Spring 1-1-2018

Experimental Investigation of Scalar Spreading by Engineered Injection and Extraction in Porous Media

Eric J. Roth
University of Colorado at Boulder, Eric.roth@colorado.edu

Recommended Citation

Roth, Eric J., "Experimental Investigation of Scalar Spreading by Engineered Injection and Extraction in Porous Media" (2018). *Civil Engineering Graduate Theses & Dissertations*. 415.
https://scholar.colorado.edu/cven_gradetds/415

EXPERIMENTAL INVESTIGATION OF SCALAR SPREADING BY ENGINEERED INJECTION AND EXTRACTION IN POROUS MEDIA

by

ERIC JAMES ROTH

B.F.A., University of Colorado Boulder, 2002

B.S., University of Colorado Denver, 2011

M.S., University of Colorado Denver, 2013

A thesis submitted to the

Faculty of the Graduate School of the

University of Colorado in partial fulfillment

of the requirement for the degree of

Doctor of Philosophy

Department of Civil, Environmental, and Architectural Engineering

2018

This thesis entitled:

Experimental Investigation of Scalar Spreading by Engineered Injection and Extraction in Porous Media

written by Eric James Roth

has been approved for the Department of Civil, Environmental, and Architectural Engineering

John P. Crimaldi

Roseanna M. Neupauer

David C. Mays

Balaji Rajagopalan

Joseph R. Kasprzyk

Date_______________

The final copy of this thesis has been examined by the signatories, and we find that both the content and the form meet acceptable presentation standards of scholarly work in the above mentioned discipline.

Roth, Eric James (Ph.D., Civil, Environmental, and Architectural Engineering)

Experimental Investigation of Scalar Spreading by Engineered Injection and Extraction in Porous Media

Thesis directed by Professor John P. Crimaldi

Abstract

Engineered injection and extraction (EIE) is a proposed in-situ contaminant remediation strategy that induces spatially and temporally varied flow fields to accelerate scalar mixing and reaction in the subsurface. Laboratory experiments were performed to quantify the effect of EIE on mixing in monodisperse porous media, and then compared with corresponding numerical simulations. Laser-induced fluorescence was used to quantify the evolution and distribution of scalar concentration fields in a quasi-two-dimensional flow apparatus containing 3 mm Pyrex glass beads that were refractive index matched to the pore fluid, glycerin. The apparatus had a 50 cm x 50 cm spatial extent, with measurements averaged through a 4 cm depth (13 bead layers), allowing for sub-millimeter-scale image resolution of plume structure. Novel methods include a system for loading spherical beads to achieve nearly homogenous hexagonal close packing, a depth-averaged porosity mapping technique, a method for mitigating wall effects, and a technique for imaging multi-species scalar mixing in porous media. Data were collected from experiments designed to test the efficacy of three EIE configurations. Experimental results were compared with those attained from numerical models, showing good qualitative agreement. Duplicate experimental data were highly reproducible. Data from the experiments could be used to improve our understanding of dispersive phenomena in porous media and improve numerical models. Experimental methods could be extended to a range of research interests.

Dedication

The work in this thesis is dedicated to my daughter Ivy and the complex world that she will inherit. Hopefully this research will lead to advancements that make the natural environment in that world a little more pristine. I would also like to dedicate this work to my parents, my brother, and Ivy's mother, all of whom have provided immeasurable support. Lastly, I dedicate this work to all the middle-aged municipal television producers out there… think long and hard before deciding on a drastic career change.

Acknowledgements

This research was supported by grants from the National Science Foundation, award numbers EAR-1417005 and EAR-1417017. Additional support came from a Dissertation Completion Fellowship awarded by the department of Civil, Environmental, and Architectural Engineering at the University of Colorado Boulder. Finally, I would like to acknowledge the members of our research team: John Crimaldi, Roseanna Neupauer, David Mays, and Lauren Reising, all of whom made important contributions to this study.

Contents

List of Tables

List of Figures

1. Introduction

As human history progresses, groundwater has become an increasingly critical resource. In 2009, of the 7 billion total people on Earth, an estimated 1.5 to 3 billion of those were dependant on groundwater as their only source of drinking water (Kundzewicz & Döll, 2009). Though most global water consumption continues to be provided by easily accessible surface water, groundwater is roughly 100 times more plentiful by volume (Fitts, 2002). Groundwater constitutes 30.1% of the total freshwater on our planet, the second largest source, only surpassed by ice and snow (Fitts, 2002). Unfortunately, groundwater reservoirs are vulnerable to contamination from a multitude of sources. Chemicals can infiltrate an aquifer from sources at the surface, subsurface pipelines or storage tanks can quietly seep for decades, oil and natural gas well casings can leak or even breech. Prior to the 1960's there were no federal guidelines concerning chemical storage or disposal. The need for regulation and remediation became more apparent through the 1970's as more became known about the proliferation of groundwater pollution and the resulting effects to human health. Groundwater contamination is both difficult and expensive to clean-up, often requiring federal emergency funding. Unfortunately, remediation efforts are often unable to lower contaminant concentrations below levels considered safe for human consumption, rendering these reservoirs un-useable for most applications. With ever-increasing water demands, a lost source of freshwater could have a large impact on future generations.

1.1 Motivation

1.1.1 Groundwater Remediation

Groundwater contamination refers to unwanted dissolved solutes or suspended materials in water. If these contaminants are present at high enough concentrations, the water can be rendered unfit for human use or detrimental to the natural environment. Contaminants can take many forms, including organic compounds found in hydrocarbon-based fuels or solvents, or from inorganic sources as is the case for road salt or mining leachate. Contamination can originate from a point source, like a leaking storage tank, or a non-point source, like pesticide application over cropland. The duration of contaminant release also varies, from a one-time pulse to a long-term continuous release. Regardless of the source or scale of groundwater contamination, if not remediated, contamination will tend to persist due to the relatively long residence time and retarded mixing potential of water in the aquifer.

Contaminant remediation in the subsurface is complicated by a variety of mechanisms. Porous media heterogeneity is a chief culprit, leading to high permeability zones and preferential pathways within the matrix. For historically popular pump-and-treat remediation strategies, fluid within these high permeability zones will be continuously cycled during treatment, leaving fluid in lower permeability zones untouched. This is due to pump-and-treat techniques that only clean the interstitial pore water and not the solid porous media (Mackay & Cherry, 1989). Additionally, sorption of a contaminant onto the porous media can leave a persistent contaminant source which requires more time to remediate than the relatively short term pump-and-treat strategies can provide. The net result is an expensive remediation strategy that can potentially leave an undesirable amount of unaltered contaminant within the porous media bed.

In-situ remediation techniques combat these problems by injecting treatment chemicals into the contaminated porous media bed, remediating groundwater and the porous media matrix simultaneously. In-situ techniques can deliver treatment chemicals to lower permeability zones by allowing additional time for chemical migration. These remediation strategies have become very popular due to lower implementation costs, aided by the fact that chemical reactions are allowed to continue long after the remediation contractor has left the site. Unfortunately, in-situ treatment efficiency is hampered by incomplete chemical mixing in the subsurface. Treatment only occurs when the contaminant and amendment chemicals are in close proximity to one another. This well-mixed condition typically only occurs at the periphery of the treatment chemical plume, leaving a large amount of contaminant untouched by remediation efforts.

1.1.2 Mixing, Spreading, and Dispersion

The efficacy of in-situ remediation techniques depends upon the ability of the treatment chemical to occupy the same pore space as the contaminant, at which point molecular diffusion will facilitate the desired chemical reaction (Cirpka, 2002; Kitanidis, 1994). At this point, the chemical species can be considered well mixed. Treatment chemicals often enter the porous media bed via injection through a well, and are then carried through the pore space by groundwater flow patterns. As the chemical plume moves through the matrix, the plume will stretch and change shape; this is called spreading. As the plume occupies more volume, local chemical concentrations within the plume must in turn decrease; this is called dilution (Kitanidis, 1994). Typically, physical spreading and dilution phenomena are combined and considered for a macroscopic porous media domain as dispersion. In Fickian models, mass flux is proportional to concentration gradients, with a constant of proportion that is dependant on flow velocity and dispersivity. Dispersivity is a variable that describes the spread and dilution of the advancing solute as it is advected through the porous media. For the most part, transport models are calibrated by empirically varying the dispersivity variable such that dispersion in the model is similar to dispersion observed in the field. In order to estimate the success of a specific in-situ remediation strategy, it is important to understand how the treatment chemical plume will spread and dilute. Thus it is critical that dispersion processes are also well understood for the porous media matrix in question.

Chemical mixing in the subsurface can be accelerated by spreading, which results from spatially varying velocity fields (Le Borgne et al., 2010). Passive spreading is caused by heterogeneity in the media matrix. This heterogeneity leads to longitudinal flow focusing (Castro-Alcala et al., 2012; Cirpka et al., 2011; Dagan, 1989; Dentz et al., 2011; Kapoor & Gelhar, 1994; Le Borgne et al., 2010); focused gradients are then tempered by transverse dispersion (Klenk & Grathwohl, 2002; Rolle et al., 2009). Active spreading is characterized by imposed flow forcings that create spatial variations in groundwater flows, including time varying point injections or extractions that create spatially and temporally varying velocity fields (Bagtzoglou & Oates, 2007; Mays & Neupauer, 2012; Sposito, 2006; Stremler et al., 2004). Active spreading techniques can be used to create chaotic advection, which has been shown to optimize spreading (Chakravarthy, 1995; Ottino et al., 1994; Piscopo et al., 2013). As defined in Aref et al. (2017), through plume stretching and folding, chaotic advection creates small scale structures in the spatial distribution of advected fields, with chaotic dynamics that evolve smooth initial distributions into patterns of filaments or sheets (depending on the dimensionality of the system) which tend exponentially fast toward geometric patterns with fractal structure. In these chaotic flows, the length scales of structures in contraction directions decrease exponentially fast, eventually becoming small enough that smoothing through diffusion can commence (Aref et al., 2017).

An important point is that many of these spreading techniques lack validation from laboratory experiments. Additionally, the numerical models used to develop these techniques rely on poorly understood pore-scale dispersion models which treat dispersivity as an empirical variable. Dispersion is superficially similar to diffusion in that it describes the movement and dilution of a chemical species. However, while diffusion is due to the intrinsic, random movement of molecules, dispersion is caused by non-uniform velocity fields that are controlled at the pore-scale by the geometry of the porous media matrix (Scheidegger, 1961). In a homogenous porous medium, longitudinal dispersion, the component of dispersion parallel to flow, dominates transverse dispersion, the component perpendicular to flow (Rolle et al., 2009). The fact that dispersion has a transverse component in a one-dimensional flow makes modeling dispersion more difficult, but when a porous media matrix is heterogeneous, or when there are two and three dimensional flow fields, accounting for the parameters that control dispersion can become quite daunting. The chief obstacle in understanding the physics of dispersion in porous media is the unknown matrix structure. Even the most carefully constructed, seemingly homogenous porous media matrix will have unwanted heterogeneity and preferential pathways. In a typical column experiment, unwanted perturbations in media packing can lead to erroneous results if heterogeneities are not accounted for, often hampering a complete understanding of dispersive processes.

1.1.3 Engineered Injection and Extraction

Engineered injection and extraction (EIE) is a proposed in-situ active plume spreading technique that employs an array of wells that use engineered injection/extraction sequences to stretch the fluid interface between the treatment solution and contaminated groundwater (Mays & Neupauer, 2012). The resulting spatial and temporal flow forcings are designed to utilize active spreading to enhance chemical mixing in the subsurface. Previous studies have investigated similar models using a pulsed dipole with reinjection of extracted pore-fluid (Trefry et al., 2012; Zhang et al., 2009). The EIE methods used in our research do not use reinjection, alleviating practical problems, while having the added benefit of supplying enhanced control over system velocity gradients by using five-well pumping protocols.

The overall benefit of EIE is enhancement of chemical reaction, leading to reduced remediation project duration and cost. Effective EIE protocols would also require less treatment chemical than other in-situ remediation techniques since the contaminant plume can be maneuvered to come into contact with the remediation chemicals, rather than relying on background flows. Furthermore, EIE could be employed to limit the advancement of a contaminant plume by creating stagnation zones. Beyond groundwater remediation, EIE techniques may be modified for use in municipal water treatment facilities or for industrial applications such as fixed bed reactors. Going forward, these EIE techniques require further validation by laboratory investigation before ultimately being tested in the field.

1.1.4 Validating EIE Techniques

Testing the efficacy of EIE is a challenge. At this point EIE has been investigated only through numerical modeling (Piscopo et al., 2013). Preliminary results from numerical investigations have indicated that EIE could be a favorable method for groundwater remediation. However, these models use Fickian dispersion, which does not accurately account for physical processes in flows through porous media. In order to propel EIE methods into the realm of practical utility, numerical results must now be compared with those acquired from laboratory experiments.

Chemical species are meant to react in-situ, so common tracer tests that measure outlet concentrations are not an appropriate validation method for EIE. Additionally, historic column experiments do not include data relating to porous media heterogeneity, a key controlling variable for spreading. Other laboratory methods such as magnetic resonance imaging have been used to map porous media structure and velocity profiles within test sections with a cross-section diameter of approximately 2.5 cm (Romanenko & Balcom, 2011). While the sampling rate, on the order of 10 ms, is suitably fast for the fluid velocities associated with groundwater flows, an apparatus of this size would be too small to accurately model the plume dynamics associated with EIE experiments, which need to operate within an essentially unbounded domain. Therefore, the next step for the experimental investigation of EIE is the development of practical experimental methods that can be used to create physical models that allow unobstructed observation of intermediate fluid dynamics over the course of an EIE sequence.

1.1.5 Other Applications

Though this research is motivated by a need to improve groundwater remediation techniques, knowledge gained from this study could be useful to a variety of researchers and industries. As mentioned previously, EIE techniques could be adapted for use in other situations that require controlled and accurate scalar mixing in porous media. Beyond this, the laboratory methods designed for EIE investigation could easily be applied to other studies of flow through porous media in quasi-two-dimensional domains. These studies could fall within the fields of environmental (transport modeling), structural (dam failure from piping), or chemical engineering (fixed-bed reactor design). Porous media flow is important to a wide variety of fields, so improved investigative techniques could have far reaching impacts.

1.2 Overview

1.2.1 Type of Research

This is exploratory research with the goal of comparing scalar transport phenomena in EIE experiments to those in corresponding numerical models. In order to achieve this goal, novel experimental methods were developed. These experimental methods are a key contribution to the scientific community. Results gained from the experimental investigations were applied to applicable numerical modeling techniques for purposes of validation and improvement.

1.2.2 Problem Statement

Numerical models indicate that EIE leads to enhanced reaction; but further validation is necessary before these techniques can be tested in the field. Due to the use of dispersivity as an empirical variable in numerical models of transport in porous media, numerical models must be calibrated by comparison to experimental data. Furthermore, the physical complexities inherent to porous media structure must be considered when evaluating EIE performance. For these reasons, a robust experimental investigation of EIE adds value to the proposed techniques.

Experimental data from the EIE sequences was compared with identical sequence data from numerical models created by a collaborating research team. Results from EIE experiments were used to calibrate, validate, and improve numerical EIE models. The overall efficacy of EIE as a remediation strategy was considered. Results from experimental and numerical investigation ultimately aid in the design of future EIE protocols.

1.2.3 Research Scope

This research encompasses the development of experimental methods leading to the design of a quasi-two-dimensional flow apparatus. The apparatus contained an essentially homogenous bed of porous media grains. Injection and extraction wells were present within the porous media bed, which was used to simulate EIE flow sequences. Each component of the experimental apparatus was rigorously tested, with success gauged by the reproducibility of results. Upon completion of each EIE sequence, experimental data were compared with numerical data in cooperation with the numerical modeling team.

1.2.4 Experimental Framework

Experimental design for the present study of EIE techniques builds upon the significant amount of experimental method development found in the literature. This includes methods for refractive-index-matching, laser-induced fluorescence, and the design of physical transport models in porous media. For the unique challenges present in EIE experiments, novel methods were created.

First, a suitable refractive-index-matched (RIM) porous media and working fluid was chosen based on criteria unique to the EIE experiments. This RIM pair was rigorously tested to ensure that the optical behavior of the system was well understood. The RIM pair was then used during the development and testing of a laser-induced fluorescence (LIF) imaging system.

An intermediate suite of experiments were executed using a one-dimensional flow apparatus. This apparatus employed the RIM pair in conjunction with the LIF imaging system to carry out continuous-planar-source plug flow experiments. These experiments were used to aid in the understanding of dispersion in a one-dimensional flow field as well as the effect of preferential flow paths along apparatus walls. Critically, this facility was used in the development and testing of components present in the quasi-two-dimensional EIE facility. These components included: injection/extraction wells, wall effect mitigation treatments, LIF optical components, and pumps. The plug flow facility was also used to develop experimental procedures including porous media loading for homogeneity.

Upon completion of one-dimensional plug flow experiments, design and construction of the quasi-two-dimensional EIE apparatus was carried out. This design drew upon lessons learned from the plug flow experiments. EIE apparatus design included an accurate fluid pumping system and a unique LIF imaging system, both of which were thoroughly tested for repeatability. Upon completion of system tests, porous media was loaded, and then saturated with the working fluid.

A suite of EIE experiments was performed. These experiments included three unique EIE sequences, a two-scalar mixing experiment, and a pore-space dye saturation experiment. Image correction was performed on the collected data, followed by the implementation of data analysis techniques. Finally, experimental data was compared with the results from the numerical models, at which point conclusions were drawn.

2. Theory and Background

2.1 Basic Concepts and Definitions

Spreading and dispersion are made possible by fluid flow. These fluid flows are driven by uneven distributions of energy. Hydraulic head is used as a proxy for energy per unit weight of water, where fluids flow from high to low head, and is described by

$$H = \frac{P}{\gamma} + z + \frac{u^2}{2g}, \qquad (1)$$

where H is total head at a definite location in the flow regime, $\frac{P}{\gamma}$ is pressure head, z is elevation head, and $\frac{u^2}{2g}$ is velocity head. For studies of flow through porous media, fluid velocities are typically very low, as such the velocity head is typically assumed to equal zero.

Whether considering groundwater, petroleum reservoirs, or filtration processes, the fluid flow of concern is in part controlled by the porous media through which it travels. Porous media consists of the combination of impermeable space and voids through which the fluid can pass. Porosity, n, is equal to the fraction of media volume containing void space,

$$n = V_v/V_t, \qquad (2)$$

where V_v is the volume of voids, and V_t is the total volume.

In approximately monodisperse, spherical media, porosity and median grain size can be used to calculate the hydraulic conductivity of the media using the Kozeny-Carman equation,

$$K = \left(\frac{\rho g}{\mu}\right)\left(\frac{n^3}{(1-n)^2}\right)\left(\frac{(d_{50})^2}{180}\right), \tag{3}$$

where K is hydraulic conductivity, μ is the viscosity of the fluid, and d_{50} is the median grain diameter of the media. However, it should be noted that the Kozeny-Carman equation can significantly over-estimate K in systems containing colloidal deposits (Roth et al., 2015b). Hydraulic conductivity, can also be calculated using, k, the permeability, by using

$$K = \frac{k\rho g}{\mu}. \tag{4}$$

Hydraulic conductivity is used to determine specific discharge, q, using Darcy's Law as

$$q = -K\frac{dh}{ds}, \tag{5}$$

where $\frac{dh}{ds}$ is the head gradient. Darcy's law is applicable for laminar flows with a Reynolds number less than 10, and ideally less than 1 (Fitts, 2002).

Average linear velocity, or seepage velocity, v, is similar to specific discharge, q , but describes the velocity for the fluid passing through the pore space of the porous medium,

$$v = \frac{q}{n}. \tag{6}$$

Reynolds number, Re, can be calculated using a characteristic length, which is d_{50} for porous media, seepage velocity, v, dynamic viscosity μ, and fluid density ρ such that

$$Re = \frac{v d_{50} \rho}{\mu}. \tag{7}$$

As a plume experiences dispersion, scalar concentrations spread and dilute. While spreading can be quantified by first moment, dilution requires the use of a macroscopic measure of dilution. As developed by Kitanidis (1994), dilution index, *E*, considers the volume of fluid occupied by solute. Using *n* discrete elementary volumes, ΔV, within the region of interest,

$$E = \Delta V \, exp\left(- \sum_{k=1}^{n} P_k \, ln(P_k) \right), \tag{8}$$

where P_k is equal to the ratio of mass within the discrete elementary volume over total system mass.

2.2 Dispersion in Porous Media

Dispersion is a hydrodynamic process describing the increasing spatial distribution and dilution of a scalar as it advects through a porous media domain. When considering scalar transport through porous media, two fundamental processes are acting on the scalar; molecular diffusion and mechanical dispersion. Diffusion can be effectively modeled as a Fickian process, while mechanical dispersion depends on spatial and temporal velocity variations which in turn depend on media structure and transient flow phenomena, which cannot be modeled with Fick's law (Fitts, 2002). Dispersion can theoretically be modeled by considering the intricacies of the porous media matrix, which forces the liquid to travel through a sequence of elementary finite and fixed stream tubes, independent of external forces, while compelling scalars to mix with surrounding fluids upon exiting the tubes (Bear & Bachmat, 1967). Dispersion is anisotropic, with transverse dispersivity that is typically small when compared to longitudinal dispersivity (Cirpka, 2002; Klenk & Grathwohl, 2002; Rolle et al., 2009).

Mechanical dispersion and molecular diffusion are often considered in unison as a one-dimensional macrodispersive flux, F_x, historically described by a form of Fick's first law,

$$F_x = -nD_x \frac{\partial C}{\partial x}. \tag{9}$$

where C is concentration, and D_x is the dispersion coefficient in the direction of flow, i.e. in the x-direction . The dispersion coefficient includes mechanical dispersion and molecular diffusion, but the diffusion term is typically neglected due to the relative minor influence it has on dispersion (Fitts, 2002). This leaves advection-dominated dispersion,

$$D = \alpha v, \tag{10}$$

where α is dispersivity in the direction of flow. Fickian gradient flux works well for describing random processes like diffusion, but dispersion is controlled by the structure of the porous media, as such, a mechanistic model would be more accurate. Unfortunately, due to the complexities of porous media geometries, mechanistic models for dispersion are not available for most studies, and as such, dispersivity is typically assumed or found empirically. Due to the effects of heterogeneity in the aquifer, it has been shown that the choice of dispersivity coefficient is dependent on the scale of the study area, with dispersivity increasing by orders of magnitude as measurements in the laboratory are applied to conditions in the field (Fitts, 2002; Gelhar et al., 1992). To remedy this inaccuracy, a method to model dispersion at higher resolution has been suggested (Lee et al., 2018), requiring intimate knowledge of porous media structure. Others have suggested different definitions of the dispersion coefficient that include power functions (Scheidegger, 1961) and/or contributions from diffusion (Kwok et al., 1995). It is apparent that there should be more agreement on how to treat the dispersion coefficient, even if that means that dispersivity should simply be considered an empirical variable. Beyond this, it would be ideal to use a more deterministic model for dispersion in porous media.

Three-dimensional transport of non-reactive scalars in porous media is governed by the advection-dispersion equation (ADE),

$$n\frac{\partial C}{\partial t}+\rho_b\frac{\partial S}{\partial t}=-n\frac{d}{dx}(v_xC)+n\frac{d}{dx}(D_x\frac{dC}{dx})+n\frac{d}{dy}(D_y\frac{dC}{dy})+n\frac{d}{dz}(D_z\frac{dC}{dz}), \tag{11}$$

where ρ_b is the bulk density, *S* is sorbed phase concentration, v_x is the component of average linear velocity in the x-direction, and

$$\begin{aligned} D_x &= \alpha_L\frac{v_x^2}{|v|}+\alpha_{TH}\frac{v_y^2}{|v|}+\alpha_{TV}\frac{v_z^2}{|v|} \\ D_y &= \alpha_L\frac{v_y^2}{|v|}+\alpha_{TH}\frac{v_x^2}{|v|}+\alpha_{TV}\frac{v_z^2}{|v|} \\ D_z &= \alpha_L\frac{v_z^2}{|v|}+\alpha_{TH}\frac{v_y^2}{|v|}+\alpha_{TV}\frac{v_x^2}{|v|}, \end{aligned} \tag{12}$$

where *TH* signifies the transverse-horizontal component of dispersivity, *TV* is the transverse-vertical component of dispersivity, and *L* is the longitudinal component of dispersivity, and $|v|$ is the magnitude of the velocity vector. Forms of this equation are often used to find analytical solutions to fluid dynamics phenomena in porous media.

Analytical solutions can help people gain insight and aid in model development by removing some of the complexities associated with the original problem. In order to find an accurate analytical solution to the advection-dispersion equation (ADE) in porous media, a number of assumptions are needed. Ogata and Banks (1961) published an analytical solution to one-dimensional dispersion of a continuous planar source. With no reaction and one dimensional flow, the governing equation is a form of the ADE,

$$D\nabla^2 C = u\frac{\partial C}{\partial x} + \frac{\partial C}{\partial t}. \tag{13}$$

Assumptions include a semi-infinite domain, a source concentration of C_0, an initial concentration downstream of the source of C equal to zero, no mass sorption to the media, and critically, that the porous medium is homogenous and isotropic. Building from equation 13, the Ogata-Banks solution takes the form,

$$\frac{C}{C_0} = \frac{1}{2}\left\{erfc\left(\frac{x-u_s t}{2\sqrt{Dt}}\right) + e^{\frac{u_s x}{D}} erfc\left(\frac{x+u_s t}{2\sqrt{Dt}}\right)\right\}, \tag{14}$$

where x is downstream position from the source ($x = 0$). Ogata and Banks validated the solution by comparison to laboratory experiments. However, it is important to note that in order to match the analytical solution to experimental data, dispersivity was treated as an empirical variable. As an example of how this solution handles concentration distribution with time, see figure 1.

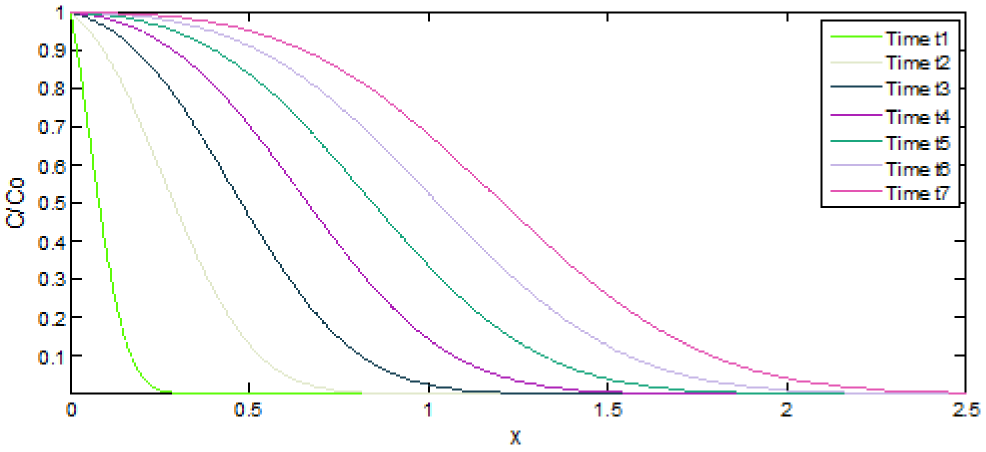

Figure 1: Ogata-Banks analytical solution at various times, as applied to research by Bhattacharjya (2014).

Many other researchers have submitted analytical solutions for different flow fields, a summary of these solutions can be found in Kwok et al. (1995). Axisymetric flow from a well bore is of interest for the research in this thesis, as such, the radial flow solution by Chen (1987) is given by:

$$\frac{C}{C_0} = 2exp\ \left(\frac{\rho-\rho_w}{2}\right)\left(\frac{\rho_w}{\rho}\right)^{\frac{1}{4}}\left[erfc\left(\frac{\omega}{2\tau^{\frac{1}{2}}}\right) - exp\left(\frac{\omega}{2\rho^{\frac{1}{2}}}+\frac{1}{4}\frac{\tau}{\rho_w}\right)erfc\left(\left(\frac{\omega}{2\tau^{\frac{1}{2}}}+\frac{1}{2}\frac{\tau^{\frac{1}{2}}}{\rho_w^{\frac{1}{2}}}\right)\right)\right], \quad (15)$$

with $\omega = \frac{2}{3}\left(\rho^{\frac{2}{3}} - \rho_w^{\frac{2}{3}}\right)$, $\rho =$ r/α, ρ_w = r_w/α, r equal to radial distance from center, r_w equal to radial distance at well bore, $\tau = \frac{At}{\alpha^2}$ for dimensionless time, $A = \frac{Q}{2\pi hn}$, and h = core thickness. This solution assumes continuous source injection of concentration C_0, non-sorbing scalars, uniform injection along the axial coordinate, miscible fluids, and an initial concentration of zero outside of the well. The validity of this solution was confirmed by Kwok et al. (1995) by comparison to a laboratory experiment. Once again, in order to match the analytical solution to experimental data, dispersivity was empirically determined.

2.3 Laboratory Techniques

With the proliferation of more powerful computers and parallelization, the use of numerical methods has become common in the study of subsurface flows. Numerical methods for groundwater investigations typically employ finite element or finite difference analysis. These methods are powerful, but model generation must be built upon a foundation of physical processes. When considering the poorly understood physics surrounding dispersion, it becomes clear that numerical results must be validated, and potentially refined with experimental data.

2.3.1 Porous Media Experiments

There is a long history of experimentation with porous media. From Henry Darcy's experiments in the early 1800's (Darcy, 1856) to the experiments of today, much has changed, and much has not. Darcy formulated his famous equation by using a simple column experiment. The column experiment has become ubiquitous in porous media research, supplying a good portion of the data that has shaped our theories on dispersion. Many column experiments use tracers that are measured at the column outlet. Measurements are then tabulated to create breakthrough curves (Robbins, 1989), which are then used to estimate dispersivity. Unfortunately, these column experiments only measure longitudinal dispersivity in a transversely bounded system, which is not representative of an effectively unbounded natural system. This is particularly true since these systems typically include preferential pathways along the walls and throughout the media matrix, which can have significant influence on the results.

Some column experiments include measurement ports along the length of the column to collect pressure data (Roth et al., 2015b; Roth et al., 2015a), or concentration data for intermediate areas between the inlet and outlet. Multiple ports can be added to the outlet to make two-dimensional measurements over the outlet cross-section (Rolle et al., 2009). Port orientation can also be changed to allow measurement of radial flow (Kwok et al., 1995). These approaches can add resolution to measurements, but this resolution is limited to the port distribution. In addition, the ports themselves can have an effect on flow dynamics as they can add preferential flow pathways or impede fluid movement.

Column experiments either use synthetic porous media, or natural porous media that has been removed from the natural media matrix and repacked into an experimental apparatus. A synthetic or repacked porous media matrix may exhibit markedly different flow characteristics than the natural system. For this reason, tracer tests are also conducted in the field by injecting and extracting from monitor wells (Anderson et al., 2003). This approach is appropriate for macro-dispersion measurements in field-based studies since there are few better options. Unfortunately, the resolution of these measurements is limited to the number of wells in the test area.

In order to understand the complexities of porous media geometry, magnetic resonance imaging (MRI) techniques have been used by a number of researchers (Manz et al., 1999; Ogawa et al., 2001; Vafai, 2015; Zhao et al., 2011). MRI scans can provide high resolution, three-dimensional maps of a porous media bed. This information could prove invaluable for the study of dispersion. Unfortunately, the imaging chamber of most MRI machines is relatively small, limiting the size of the porous media test section. MRI machines are also very expensive, most laboratories would not be able to afford one, requiring researchers to rent time from other institutions. X-ray microtomography can also be used to gather information on pore-scale geometry within porous media, but measurement areas are confined to the pore-scale, making this an impractical technique for measuring larger scale representative elementary volumes within the media matrix (Wildenschild & Sheppard, 2013).

2.3.2 Media Packing

When considering a synthetic porous media matrix in the lab, the nature of the packing largely determines fluid trajectory, and therefore, controls scalar transport. Historically, it has been impossible to map heterogeneity in the matrix. Randomly packed, heterogeneous porous media matrices will leave many questions about media matrix effects on flow dynamics due to the unknown structure of the matrix. For this reason, many researchers have attempted to homogenously pack porous media within their experimental apparatus. To increase homogeneity, monodisperse media is typically used in conjunction with a compaction technique such as mechanical compression or vibration (Iskander, 2010; Rice, 2013; Robbins, 1989). Often, packing techniques are unspecified in the literature, an unfortunate omission.

The highest likelihood of achieving homogeneity would come from a porous media matrix with monodisperse beads, uniformly packed in a hexagonally close packed (HCP) matrix (Fig. 2). This would be a structurally stable matrix with a high degree of structure. The HCP configuration represents the maximum packing density for monodisperse spheres, with a minimum porosity of 0.26 theoretically possible (Smith et al., 1929). However, due to the difficulties associated with homogeneous media packing, which include non-uniform sphere size, apparatus with rigid walls that can upset the packing geometry, and the required time to ensure that each grain is aligned correctly, a porosity of 0.35 to 0.45 is most likely in practice (McWhirter et al., 1998; Smith et al., 1929). Other studies, that do not necessarily use an HCP pattern, report porosity measurements falling within this range, which are typically near 0.4 (Atmakidis & Kenig, 2015; Carman, 1937; Cohen & Metzner, 1981; Eisfeld & Schnitzlein, 2001; Fand et al., 1987; Gunn, 1987; Lee et al., 2018; McWhirter et al., 1998; Muhammad & Massimo, 2017; Rolle et al., 2009). The minimum porosity reported by other researchers, and only value below 0.348, was a value of 0.32. This minimum value was measured within the central volume of the experimental test section, a region that did not come into contact with apparatus walls (Schwartz & Smith, 1953), so this value is not comparable to system-wide porosity measurements within the apparatus as a whole. For a polydisperse system, lower porosities are possible due to smaller media grains filling in the interstitial voids left by larger media grains. However, porosity measurements from a polydisperse system would not necessarily correspond with structural homogeneity.

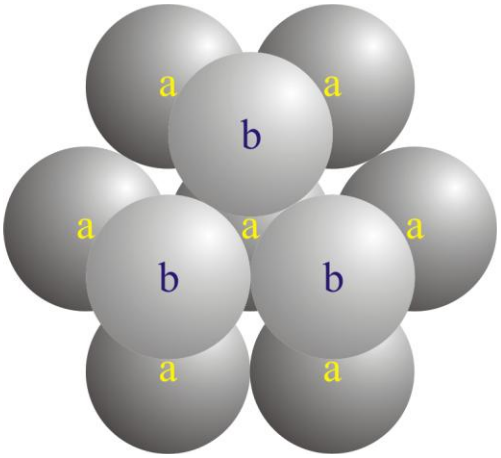

Figure 2: Hexagonal close pack configuration (Generalic, 2018)

2.3.3 Wall Effects

For spherical porous media, porosity measurements at the apparatus wall approach unity (Cohen & Metzner, 1981; Eisfeld & Schnitzlein, 2001; Gunn, 1987; Schwartz & Smith, 1953).

For an HCP packing, this means that media heterogeneity will increase with proximity to the wall, with a corresponding increase in hydraulic conductivity. These near-wall hydraulic conductivities will manifest as velocities that are 30-100% higher than those present within the core of the media matrix (Schwartz & Smith, 1953). If wall effects are ignored, preferential pathways at the wall can contribute to significant experimental error in porous media experiments(Cohen & Metzner, 1981). Some experimental techniques take care to consider regions sufficiently far from the walls to negate wall effects (Rolle et al., 2009). However, distributed preferential pathways through the media matrix are also common. Unfortunately, these preferential pathways can easily divert flow to the wall, creating a short circuit around the region of interest.

In order to account for unwanted wall effects, a correction factor can be applied during the data analysis phase (Cohen & Metzner, 1981; Eisfeld & Schnitzlein, 2001). While a correction factor may alleviate some error, it would be preferable to design the experimental apparatus such that the wall effects are physically mitigated. Few experimental techniques for mitigating wall effects were found in related porous media studies, with the exception of a silicon sleeve placed around a porous media sample (Rice, 2013). This technique helps to limit the flow at the wall by creating a surface that can deform around porous media grains, such that porosity near the wall approaches zero rather than unity.

2.3.4 Refractive Index Matched Porous Media

Experiments employing refractive index matched (RIM) porous media have become very popular in recent decades (Amini & Hassan, 2012; Cenedese & Viotti, 1996; Edery et al., 2015; Iskander, 2010; Moroni & Cushman, 2001; V. Patil et al., 2014; Rolle et al., 2009; Roth et al., 2015b; Stohr, 2003; Werth et al., 2010). RIM porous media employs the tenets of Snell’s Law by matching the index of refraction of the porous medium with that of the working fluid. Snell's law states that:

$$\frac{\sin\theta_2}{\sin\theta_1} = \frac{v_2}{v_1} = \frac{n_1}{n_2} \tag{16}$$

with θ_1 = incident light angle of approach, θ_2 = angle of refraction, v = velocity of light in each medium, and n = refractive index of each medium. By matching the refractive index of the two materials, light can travel straight through the system, allowing undistorted optical access (Fig. 3). These experiments have the advantage of attaining optical access to the inner porous media matrix (Budwig, 1994; Iskander, 2010).

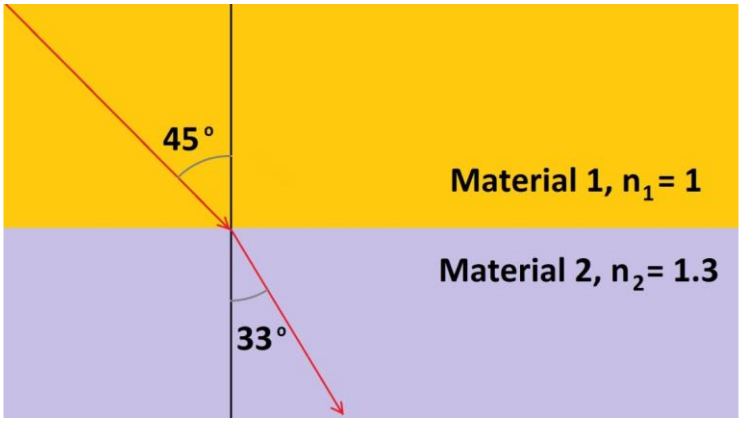

Figure 3: Illustration of Snell's Law. Mismatch of refractive index (n_1 and n_2) between material 1 and 2 changes the direction of an incident light ray, hampering optical access.

Previous studies have used various combinations of media and fluid depending on their research needs. An excellent summary of RIM pairs can be found in Amini et al. (2012). The selection of suitable RIM candidates depends on chemical reactivity, cost, toxicity, combustibility, viscosity, grain size, grain rigidity, and desired optical clarity. The refractive index of the media and fluid pair can be fine tuned by altering chemical concentrations of the fluid, temperature of the RIM system, and incident light wavelength (Patil & Liburdy, 2012; Wiederseiner, 2010).

A practical class of RIM pairing uses Pyrex glass in conjunction with glycerin as the working fluid (Cenedese & Viotti, 1996; Moroni & Cushman, 2001; Park et al., 1989). Glycerin is inexpensive, non-toxic, has low reactivity, and matches the refractive index of Pyrex glass beads. At 20°C, glycerin and Pyrex glass both have a refractive index of 1.474 (Dow-Corning, 2015; Miner & Dalton, 1953). Pyrex glass beads come in a variety of sizes, are rigid, have consistent optical clarity and size, and are durable. The downside to using glycerin is its relatively high viscosity, 1400 times more viscous than water at 20^{o} C ((Finnemore & Franzini, 2002; Miner & Dalton, 1953).

2.3.5 Laser-Induced Fluorescence

Laser-induced fluorescence (LIF) techniques have become a popular choice for pore-scale or Darcy-scale, non-intrusive, real-time measurement of scalar concentrations in RIM porous media (Amini & Hassan, 2012; J.-D. Chen & Wada, 1986; Fort, 2015; Stohr, 2003). The study by Stohr (2003) presents methods for performing planar LIF with RIM porous media. These experiments produced three-dimensional images of scalar transport within a one-dimensional flow apparatus with dimensions of approximately 5 cm x 5 cm x 10 cm (Fig. 4). This study is useful as it presents a detailed description of index matching, dye selection, imaging and image correction.

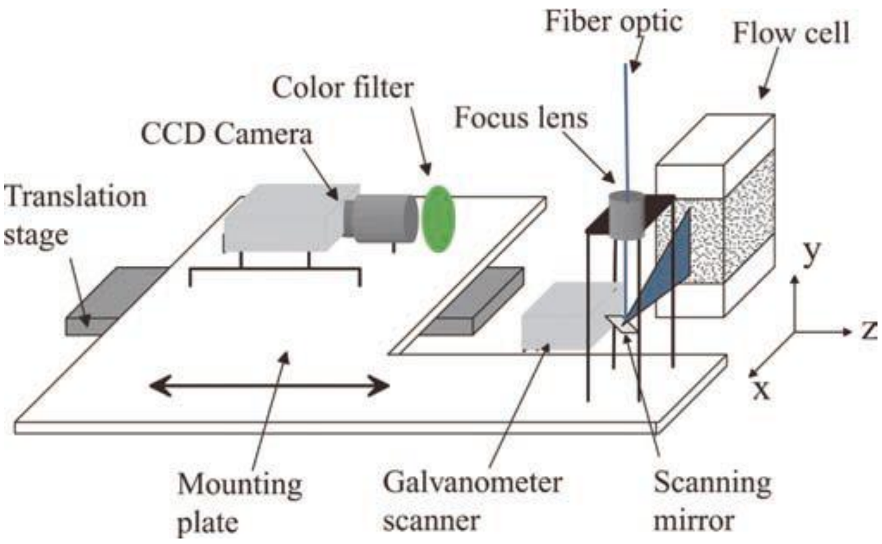

Figure 4: Schematic of RIM, PLIF apparatus (Stohr, 2003).

LIF uses laser light to excite aqueous fluorescent dyes within the pore fluid. Dyes are selected that absorb light at a specific lasing wavelength, and then in the excited state, the dye will emit light at a different wavelength. The difference between the peak absorption wavelength and peak emission wavelength is called the Stokes shift. The Stokes shift should be large enough to minimize overlap of the absorption and emission spectra (Fig. 5), allowing the use of a bandpass camera filter, completely blocking the lasing wavelength while transmitting the peak of the emission spectrum. This allows imaging of the fluoresced dye without interference from the excitation source.

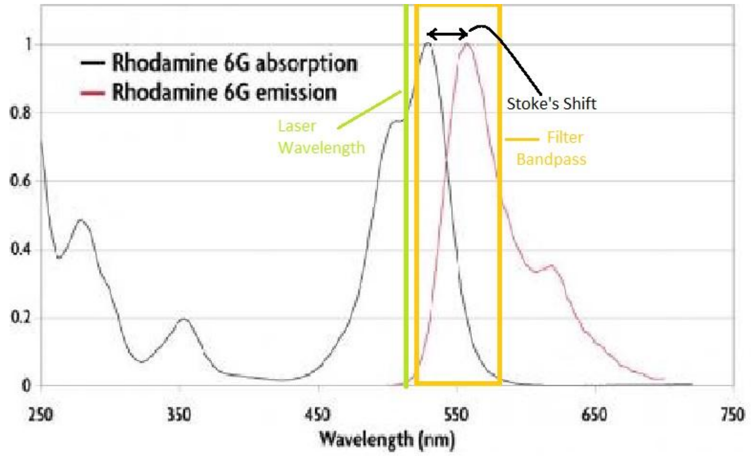

Figure 5: Absorption and Emission spectra for Rhodamine 6G (Motif, 2018).

Crimaldi (2008) presents a review on aqueous planar laser-induced fluorescence (PLIF). This review discusses dye fluorescence characteristics, sources of error in fluorescence intensity measurements, experimental techniques, and image processing. Fluorescence theory and laser beam characteristics are also presented in detail, providing sufficient information to design a robust PLIF system that makes spatial fluorescence intensity measurements that have a linear relationship to dye concentrations within the test section. In related experiments, these PLIF techniques were used to make measurements in a system with two scalars as a proxy for chemical mixing (Soltys & Crimaldi, 2011). The dyes used were passive scalars, i.e. non-reactive, so this technique modeled a very slow reaction, or in other words, a system with a very low Damköhler number. Though the PLIF techniques presented in these papers were developed for use in open channel flows, application to a system containing porous media is possible. The principal requirement for the use of PLIF is that there is optical access to the measurement region (Crimaldi, 2008). For the current research, this requirement is achieved by the use of a refractive index matched porous media and working fluid.

3. Experimental Methods

3.1 Summary of the Experimental Approach

To make measurements of scalar distribution in a quasi-two-dimensional, engineered injection and extraction (EIE) cell, with homogenous porous media, employing LIF imaging techniques, the development of a suite of novel experimental methods was needed. To ensure that the data provided from these methods were meaningful, each new method was validated by testing for precision and repeatability.

A range of possible refractive index matched (RIM) porous media and fluid combinations were tested. Upon selection of the most appropriate RIM pair, laser-induced fluorescence (LIF) imaging techniques were developed for the RIM applications. A one-dimensional plug flow apparatus was built to investigate methods for homogenous media packing and for mitigation of preferential flow along apparatus walls. After consideration of the fluid dynamics present in one-dimensional plug flow experiments with random close pack bead configurations, porous media packing techniques were developed. One-dimensional plug flow experiments were also used to study contributions from preferential flow along apparatus walls and to develop strategies to mitigate these unwanted effects. Pumping system components for the quasi-two-dimensional EIE apparatus were designed and tested for repeatability. LIF techniques were developed and tested specifically for the EIE apparatus. The apparatus was loaded with media using a specialized procedure and custom built equipment, connected to the fluid transfer system, and saturated with RIM fluid. Finally, a suite of single-scalar EIE experiments were performed, followed by a two-scalar EIE experiment. EIE experiments concluded with a dye-flooding experiment designed to gather porosity data for the specific porous media matrix configuration used in all EIE experiments.

3.2 Refractive Index Matched Porous Media

Initial RIM pair selection was based on those used in previous studies. A thorough review of RIM pairs can be found in Budwig, 1994, Hassan, 2008, Wiederseiner, 2010, and Wright, 2017. The field of initial RIM candidates was narrowed based on the needs and constraints present in subsequent EIE experiments. Specifically, the RIM pair had to provide suitable optical clarity and minimal distortion for an imaging depth equal to the depth of the EIE apparatus, at least thirteen bead diameters (approximately 3.5 cm), as well as being safe to work with and non-reactive to other apparatus materials. In addition, the ideal RIM fluid would be easy to prepare and cost effective, allowing large volumes of fluid to be used during experiments. Finally, optical limitations of the RIM pair were considered in the final design of the EIE apparatus (App. 8.3 and 8.5).

The porous media material was chosen a priori. Though homogeneity was desired, some heterogeneity in the porous medium was unavoidable, as such, scalar spreading due to media heterogeneity during EIE is a key result. It was important to have a porous media field geometry that did not change over the course of a single EIE sequence experiment, and preferable to use the same bead loading over the course of all EIE experiments (including all three EIE pumping sequences). Many RIM porous media materials are pliable, which could lead to media deformation in the presence of fluid flow. Therefore, only rigid RIM media materials would be considered. In order to produce a homogenous porous media field, it was important that the media grains have consistent size and shape. Beyond the concerns associated with creating a faithful porous media model, it was desirable to use media that exhibited a high degree of optical clarity to aid in optical access, excellent chemical compatibility so that the beads could be saturated with the pore fluid for long periods without degradation, and durability since scratches will accentuate any refractive index mismatch. Given the constraints, a good porous media candidate was borosilicate glass beads. Borosilicate glass beads are available in a variety of sizes from 1 mm to 8 mm, are relatively inexpensive compared with other RIM porous media choices, and are exceptionally consistent in size and in material composition. Glass is significantly more durable than other RIM choices such as acrylic, making it scratch resistant, which allows for the cleaning and reuse of the porous media. Critically, borosilicate glass has a relatively low index of refraction at 1.474, making it easy to match to multiple RIM fluids. 3 mm mean diameter Pyrex glass beads (Pyrex, part# 7268-3) were ultimately chosen as the primary porous media for the EIE experiment.

The selection criteria for an RIM fluid included (in order of descending importance) refractive index, chemical compatibility with experimental apparatus materials, toxicity, cost, flammability, and ease of use. After consulting the literature, five prime candidates for a working fluid were selected: glycerin (99.7% USP kosher, Chemworld, CAS# 56-81-5), diethyl phthalate (abbreviated DP, Fisher Scientific, CAS# 84-66-2) with isopropyl alcohol (abbreviated IPA, Fisher Scientific, CAS# 67-63-0), trans-cinnamaldehyde (Acros Organics, CAS# 14371-10-9) with IPA, dimethyl-sulfoxide (abbreviated DMSO, Fisher Scientific, CAS# 67-68-5) with water, and ammonium-thiocyanate (Sigma-Aldrich, CAS#1762-95-4) with water. While all five of the preliminary candidates could be tuned to an appropriate refractive index and were not prohibitively expensive, some disadvantages became obvious. Initial chemical compatibility tests revealed that trans-cinnamaldehyde was corrosive to acrylic and most sealants. Ammonium-thiocyanate poses an inhalation hazard when in a solid form. Though it was meant to be dissolved in solution, if spilled, ammonium-thiocyanate solution left a substantial amount of highly toxic precipitate after evaporation.

Quantitative analysis of the remaining RIM porous media and fluid pairs were performed by consideration of width-averaged, vertical intensity profiles of the sample’s projected image using an RIM testing facility (for details on the RIM testing facility, appendix section 8.3). Intensity profiles for each RIM sample were compared with the intensity profile of an unperturbed laser sheet, that is, the projection of only the expanded laser sheet, with no sample in the intermediate path. A good refractive index match will more closely resemble the unperturbed intensity profile than a poor refractive index match (Fig. 6). There are impurities present in the Pyrex glass, as well as impurities and microscopic air bubbles in the fluid. These impurities can reflect or block incident light. Therefore, the intensity profiles for the samples would not be expected to exactly integrate to the same value as the unperturbed laser sheet. Other irregularities in the sample intensity profile were most likely due to non-uniform material properties of the glass beads.

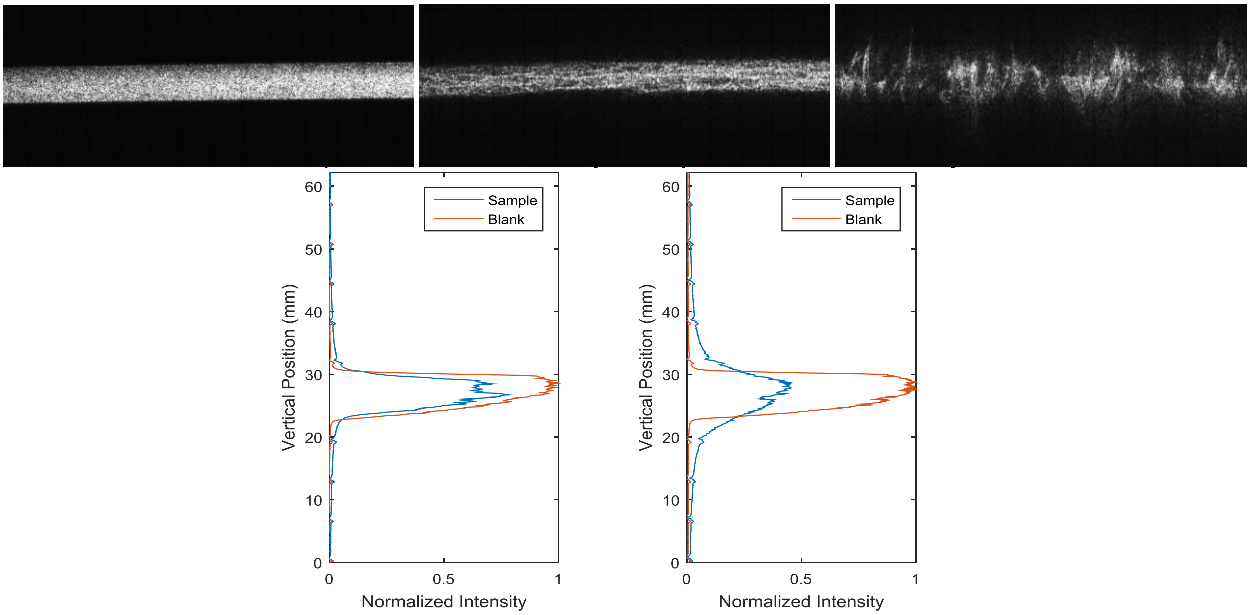

Figure 6: Unperturbed laser sheet projection (top left), sample projection with better refractive index matching (top middle), sample projection with worse refractive index matching (top right) after the addition of 0.04 mL of water. Intensity profile of better refractive index match compared with the unperturbed laser sheet, labeled as “Blank” (bottom left). Intensity profile of worse refractive index match compared with unperturbed laser sheet, labeled as “Blank” (bottom right). RIM samples were comprised of 3 mm Pyrex beads and different concentrations of DMSO and water.

Refractive index tuning for DP with IPA, DMSO with water, and glycerin was carried out using the RIM test bench (App. 8.4). Each fluid exhibited a similar refractive index match to borosilicate glass (Fig. 7). The refractive index of DP was tuned by adding 0.02 mL increments of IPA, as was the DMSO with water, until a suitable match was observed. Ultimately, the EIE experiments will require large volumes of working fluid, on the order of ten liters per experiment. While refractive index matching by concentration was effective for small volumes of fluid, it was difficult to scale the mixtures up to liter sized batches. Small variations in concentration lead to significant changes in refractive index. This was a key benefit of glycerin; at room temperature, it matched the refractive index of borosilicate glass without the addition of another component. In addition, glycerin was less expensive than any other choice, exhibited superior chemical compatibility, was non-flammable, and carried with it no health advisories, making it the safest to work with. A disadvantage of using glycerin is its high viscosity, 1410 centipoise at 20 degrees C (Miner & Dalton, 1953), as compared to water which is 1 centipoise at 20 degrees C (Finnemore & Franzini, 2002).

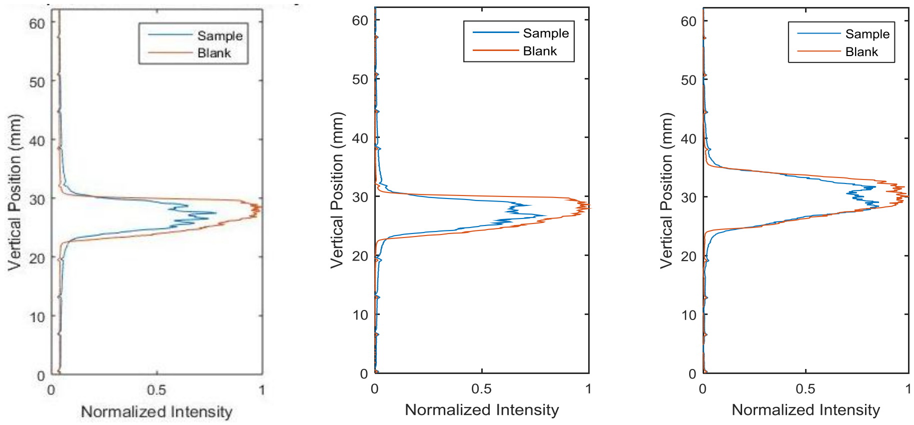

Figure 7**:** Comparison of refractive index match of Pyrex beads and pore fluids: DP with IPA (Left), DMSO with water (Middle), glycerin (Right). The glycerin sample's profile looks different because it used a different camera setup. Material impurities can cause sample intensity magnitude to be lower than that of the unperturbed sheet (Blank).

The glycerin/Pyrex bead RIM pair was then tested for sensitivity to temperature, optical distortion, and an experiment measuring maximum probe depth for a coherent laser sheet (App. 8.5). This information would inform decisions regarding the maximum imaging depth in the design of the EIE apparatus. It was found that the typical range of ambient temperature in the laboratory, 21 to 24 degrees C, was suitable for providing a reasonable refractive index match between the glycerin and Pyrex beads. Imaging a grid with 3 mm grid blocks through a depth of 33 beads (9.9 cm) produced images with a reasonably low amount of optical distortion (Fig. 8). Optical distortion in these images was similar to examples of this technique found by Zhu et al. (2016). For the depth averaged imaging technique used in EIE experiments, the resolution should be fine enough to resolve overall concentrations at a scale smaller than one bead diameter, rather than the increased resolution required to image the fluid dynamics within a pore. The planned imaging depth of the EIE cell was 3.5 cm, which should be below the necessary limits for reasonable optical distortion for a depth averaged system.

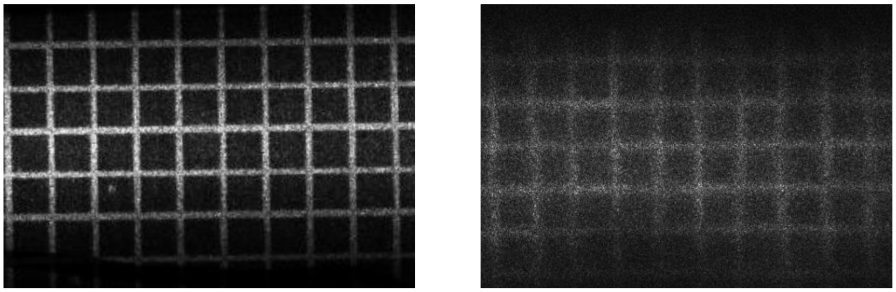

Figure 8: Image of grid with no media or fluid (left). Image of grid through 33 Pyrex beads and glycerin. Proposed EIE cell will image through 13 Pyrex beads.

In order to perform LIF, the fluorescent dye must be soluble in glycerin. A selection of fluorescent dyes including Rhodamine 6G (Aldrich, CAS# 989-38-8), Fluorescene Sodium (Fluka, CAS# 518-47-8), and Oxazine 725 Perchlorate (Exciton) all dissolved in glycerin. The fluorescence characteristics of Rhodamine 6G were tested at different dye concentrations to ensure a linear relationship between dye concentration and fluorescence intensity. Rhodamine 6G was chosen as the primary dye for subsequent experiments due to its common use in other LIF experiments (Crimaldi, 2008).

The dye stock-solution was prepared by adding a specific mass of dye powder to one liter of glycerin within an Erlenmeyer flask. Mixing was performed with a magnetic stir-bar and stir plate. As compared with water, the relatively high viscosity of glycerin leads to low turbulence in the fluid during stirring, retarding mixing. Consequently, solutions were considered well mixed after continuous stirring for three days. The resulting stock-solution was then partitioned, diluted, and re-stirred to prepare dye solutions for subsequent experiments.

3.3 One-Dimensional Plug Flow

3.3.1 Apparatus Overview

The one-dimensional plug flow experiments were designed to capture preliminary one-dimensional dispersion data, test for media heterogeneity, analyze wall effects, and to test wall effect mitigation strategies. The apparatus was made of glass and consisted of a porous media chamber, measuring 17 cm x 8 cm x 7 cm. The entrance and exit of the media chamber were bounded by an anodized aluminum screen with a maximized open area to ensure unperturbed flow, while simultaneously holding the media firmly in place. Upstream of the apparatus chamber containing the porous media, dye was preloaded into an open cavity and segregated from the media by a plastic curtain. The porous media was saturated with dye-free glycerin. A laser sheet illuminated the center section of the media chamber parallel to flow (Fig. 9). The camera imaged the illuminated plane through the imaging window, oriented 90 degrees off of the laser sheet path.

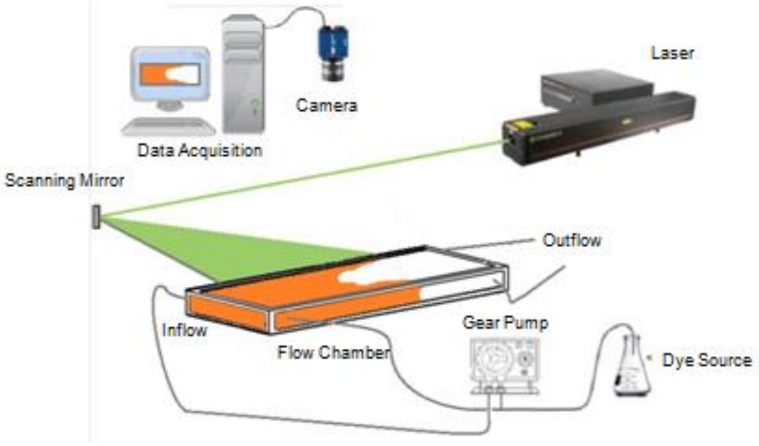

Figure 9: Schematic of one-dimensional plug flow apparatus

For plug flow experiments, the media chamber was packed with 3 mm Pyrex beads. After the media was loaded, a lid was sealed to the top of the chamber using silicone sealant. A Rhodamine 6G dye solution was added to the dye chamber, and then the media was slowly saturated with glycerin. Glycerin was pumped into an access port located at the lowest elevation of the media chamber, using capillary suction to completely fill the pore space from the bottom to the top. Immediately prior to data collection, the dye segregation curtain was pulled back. A continuous flow of dye was injected into the dye chamber upstream of the porous media using a gear pump (Ismatek, model# CB 78008, with Cole-Parmer model# 73004-14 pump head). Dye exited the dye chamber as a continuous planar source at the porous media boundary, which then flowed through the media chamber, exhibiting dispersive behavior controlled by media heterogeneity. Downstream of the porous media, on the other side of the aluminum screen, was another open cavity. Fluid exits the system through an outlet, open to the atmosphere and located 2 cm above the top elevation of the flow cell.

3.3.2 Laser-Induced Fluorescence Imaging in RIM Porous Media

For one-dimensional plug flow experiments, a 514 nm laser sheet was used to excite Rhodamine 6G fluorescent dye within the middle centimeter of the porous media chamber. In order to create the 1 cm thick laser sheet, the beam was passed through a beam expander to create a 1 cm diameter beam which was then reflected off of a single-axis scanning-galvo-mirror (Thorlabs, part# GVS011). As the scanning-mirror rotates, the reflected beam swept through the porous media domain parallel to fluid flow.

A camera, viewing perpendicular to the incoming laser sheet, captured images of dye fluorescence. Images were logged within an external computer, optimized for image capture (Quazar, Boulder Imaging). An optical band-pass filter (555DF30, Omega Optics), was attached to the camera lens, blocking the 514 nm excitation light from the laser while transmitting fluoresced light from the dye. The camera and scanning-galvo-mirror system were each controlled by a LabVIEW code which sent trigger signals to each component, communicated through an intermediate DAQ board (National Instruments, product# USB 6383). The virtual shutter of the camera was opened, which initiated image capture. The synchronized galvo-mirror then rotated, sweeping the beam through the porous media domain. Upon completion of the beam sweep, exposure time for this single image was stopped by closing the camera's virtual shutter. The resulting image showed fluorescent emission intensity from the dye present within the laser sheet.

Prior to initiating dye flow in the one-dimensional apparatus, a background image was captured. There was no dye within the porous media chamber, so this image only included unwanted artifacts from the system which were then removed from subsequent images during image processing. Upon commencement of the experiment, images were captured at a rate of one frame per minute. This frame rate was appropriate for the timescale at which this experiment proceeded. Dye was continuously pumped through the test section until a full three pore volumes of dye had been eluted. At this point, the entirety of the pore space within the test section could be considered saturated with the dye solution at source concentration. Image capture was stopped and the experimental run was concluded.

For dye mixed at sufficiently low concentrations, fluorescence intensity exhibits a linear relationship with dye concentration. However, it is important to consider only the light fluoresced from the dye, and the physical space in which the dye resides. Therefore, raw LIF images captured by the camera during experiments require image correction and calibration. Image processing ensures that unwanted artifacts are removed, including variations in illumination intensity, which can translate into inaccurate concentration measurements. Image processing is also used for purposes of calibration, synchronizing scalar mass measurements within an image to the physical mass of dye that was injected into the experimental apparatus. Calibrating for porosity is also important, as the volume of dye imaged within a pixel is dependent on the available pore space within that imaged volume. A robust image correction and calibration protocol was applied to all of the experimental data presented in this thesis.

Raw LIF images, $R(i,j)$, are comprised of 1040 by 1392 pixels that individually record light intensity values. Raw images are corrected and calibrated to form quantitative measures of scalar concentration, $C(i,j)$. Present within the raw image are background artifacts, parts of the image that do not correspond with light emitted from the dye. Background artifacts can come from unwanted light in the laboratory or attenuated laser light transmitted through the camera filter. In order to measure the light intensity emitted by the dye in the absence of any influence from background light sources, equation 17 is used,

$$I(i,j) = R(i,j) - B_R(i,j). \tag{17}$$

Where the light intensity concentration, $I(i,j)$, is found by subtracting the intensity measurement of each pixel in a background image, $B_R(i,j)$, from the corresponding pixel in the raw image, $R(i,j)$. The background image is captured while employing laser illumination, prior to injecting any dye into the experimental apparatus. The background image will capture unwanted artifacts from sources not emanating from the fluorescent dye plume. The scalar concentration, $C(i,j)$, can be found by multiplying intensity concentration by a unit conversion constant. However, for the one-dimensional plug-flow experiments, this conversion was not necessary since it was accomplished during the image correction process.

Variations in laser intensity and media optical clarity within the apparatus domain can cause inconsistencies in imaged light intensity, reducing the accuracy of concentration measurements. A similar effect is caused by the structure of the porous media. Solid media grains occupy a volume that would otherwise be filled with dye. For this reason, variations in porosity and pore-geometry lead to variations in dye emission intensity that are not caused by variations in dye concentration. Therefore, the light intensity concentration image, $I(i,j)$, must be corrected for void volume in each pixel. For this correction, the experimental apparatus, containing the identical porous media configuration as the EIE experiments, was uniformly flooded with dye of a known concentration. Dye was continuously injected until intensity measurements remained constant, ensuring a well mixed system with complete dye saturation within the pore space. A dye-saturated image, $S(i,j)$, was captured by the camera and then used in the correction given by equation 18,

$$I_o(i,j) = S(i,j) - B(i,j). \tag{18}$$

For one-dimensional plug flow experiments, the background image for the dye-saturated condition was the same as that for the raw images, so $B(i,j)$ was subtracted from $S(i,j)$, eliminating unwanted artifacts from the dye-saturated image. The background-corrected, dye-saturated image, $I_o(i,j)$, represents light intensity produced by the maximum dye volume possible within the domain, at the source concentration.

As shown in equation 19, the background-corrected raw light intensity image is then divided by the background-corrected dye-saturated light intensity image, providing an image for instantaneous intensity concentration, $I(i,j)$, over initial source intensity concentration, $I_o(i,j)$. For the plug flow experiments, dye was continuously injected throughout the experiment until reaching dye saturation; so $I(i,j)$ and $I_o(i,j)$ were taken with identical dye, under identical conditions. Therefore, no conversion constant was needed to convert from light intensity to dye concentration, leaving the non-dimensional value for $\frac{I}{I_o}\,(i,j)$ equivalent to non-dimensional dye concentration in the system, $\frac{C}{C_o}\,(i,j)$. The resulting image corrected for all light intensity fluctuations that were not caused by changes in dye concentration, faithfully representing non-dimensional scalar concentration in the system.

$$\frac{C}{C_o}(i,j) = \frac{R(i,j) - B(i,j)}{S(i,j) - B(i,j)} \tag{19}$$

3.3.3 Porous Media Packing

An ability to control porous media packing in subsequent EIE experiments was critical for accurately modeling and understanding the flow dynamics of the system. One key use of the one-dimensional plug flow apparatus was the development and validation of media packing techniques. An approximately homogenous media packing was desired for EIE experiments, enabling investigation of dispersive processes without consideration of the geometric complexities present within a heterogeneous porous media field. A homogenous porous media packing can be achieved in a structurally stable geometry such as a hexagonal close pack (HCP) or face-centered cubic pack configuration. The optimal packing geometry for maximum density, and lowest porosity for monodisperse spheres is the hexagonal close pack configuration (Smith et al., 1929). Therefore, when employing an HCP packing geometry, the spherical and essentially monodisperse Pyrex glass beads used in the experiments could be considered to have a more homogenous packing as porosity was reduced. Thus, system porosity could be used as a proxy for homogeneity within the experimental apparatus.

A variety of packing methods were investigated, including vibration, compaction, and layer-by-layer screeding. Unfortunately, none of the bulk packing techniques worked effectively. While spherical beads naturally orient themselves in an HCP geometry, the occasional bead will become misaligned, causing misalignment for multiple beads that are in contact with the original outlier, eventually causing non-ideal packing for sequentially placed beads in the system. Therefore, care must be applied to the placement of every bead in the system. Considering that the EIE apparatus contained approximately 70,000 beads, placing individual beads was not feasible. A technique involving layer-by-layer bead placement, followed by gentle shaking was developed. This technique exploited each bead's proclivity toward self alignment within an HCP lattice, and was aided by the flat, parallel walls of the apparatus. HCP orientation was confirmed for every bead in a layer before adding additional beads. For a detailed description of the HCP loading technique, consult appendix section 8.3.

In the one-dimensional plug flow experiments, the degree of homogeneity was quantified by porosity measurements and by the distribution of concentration gradients caused by dispersion within the system. The measured porosity of the experiments, ranging between 0.314 and 0.347, were very low compared to the previously reported values in section 2.4.2, which were typically near 0.4 and as low as 0.348. The degree of homogeneity achieved by the HCP bead packing procedure was also evident from the homogenous flow distribution in the one-dimensional plug flow experiments (Fig. 10). In the region sufficiently far from the apparatus walls, the dispersive front maintained an approximately planar and perpendicular profile with respect to the direction of flow. If the packing were heterogeneous, one would expect to see a sloped dispersive front, or the formation of preferential pathways in the porous media field, similar to the behavior seen near apparatus walls.

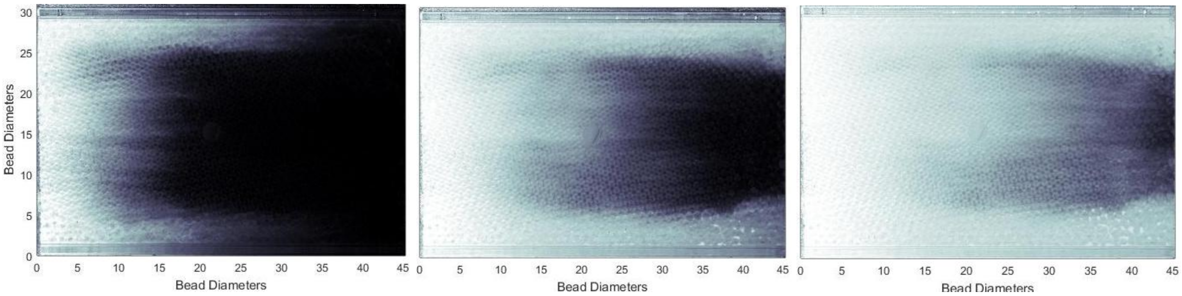

Figure 10: One-dimensional plug flow at early time (left), intermediate time (middle), and late time (right). Neglecting regions near the walls, the absence of preferential flow indicates a homogenous porous media packing.

To quantify longitudinal dispersion, the Ogata-Banks analytical solution for one-dimensional, continuous-source concentration distribution was fit to the concentration data obtained in the one-dimensional plug flow experiments (Fig. 11). In order to fit the solution to the experimental data, only the region uninfluenced by wall effects was considered. Concentration measurements were averaged perpendicular to flow for various domains. The analytical curve was tuned to the data by changing velocity and dispersion coefficients. Though further analysis is necessary, preliminary results indicate a dispersion coefficient equal to 0.002 cm^2/s and a longitudinal dispersivity of 0.77 cm. The dispersion coefficient found in the experiment was within the range of 10^{-2} and 10^{-4} cm^2/s reported in Ogata-Banks (1961).

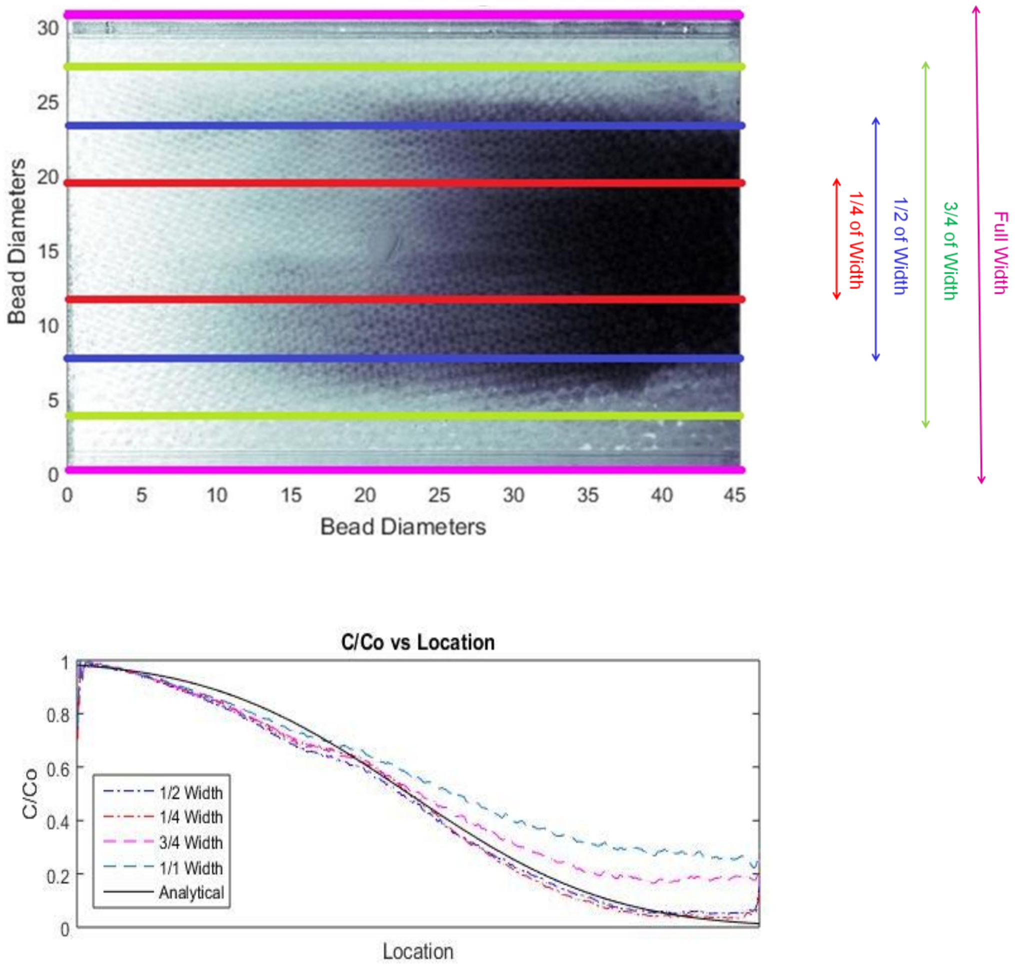

Figure 11: The analytical solution for dispersion was fit to the data for various transversely averaged longitudinal domains. The analytical solution exhibited reasonable agreement for regions outside the influence of preferential flow along the walls.

3.3.4 Wall Effects and Mitigation Strategies

The walls had little effect on flow dynamics within the middle half of the domain (Fig. 11). This indicated a region within the apparatus that could be considered sufficiently far from the wall in order to neglect influences from physical experimental constraints. However, the preferential flow along the wall was much higher than that of the unaffected porous media matrix (Fig. 10). Dispersion along the wall included a longitudinal component, propelling the dye at the wall beyond that in the field. Compounding the problem was transverse dispersion which caused dye to spread from the wall into the porous media field. This is a clear illustration of the effects of preferential flows at apparatus walls.

To mitigate wall effects, methods were developed to cause the wall to exhibit similar dispersion characteristics to the rest of the porous media matrix, based upon the tenets of the Kozeny-Carman equation, which states that permeability is a function of porosity. Two wall treatments were developed in order to control porosity and therefore control the flow along apparatus walls. For one-dimensional plug flow experiments, a centimeter wide slice parallel to flow passing through the middle of the apparatus was illuminated by the laser sheet, allowing the imaging of behavior along two walls. The wall through which the laser sheet passed is defined as the bottom wall and the opposite wall is defined as the top wall. While the bottom wall was required to maintain unobstructed optical access for transmittance of the laser sheet, the top wall did not need to transmit the laser sheet and could therefore be opaque.

For the top wall, a 3 mm layer of silicone (GE, 100% Silicone II, Black) was applied to the wall (Fig. 12). This layer was smoothed down using a screed, ensuring a consistent silicone depth. The silicone layer was then pressed into the pre-packed HCP bead field. The silicone was allowed to dry before commencement of the experiment. The result of this treatment was a wall of hemispheres which preserved HCP packing and forced consistent porosity from the porous media field to the wall, as such, the Kozeny-Carman equation would predict constant permeability near the wall.

To preserve optical access through the bottom wall, porosity was matched to that in the field by placing 1 mm borosilicate glass beads (Chemglass, part# CG-1101-06) into the interstitial area between the wall and the first layer of 3 mm Pyrex beads (Fig. 12). The addition of the 1 mm bead sub-layer forced approximately uniform porosity from the porous media field to the wall. In order to install the 1 mm sub-layer, a single-layer of 3mm beads was rigidly affixed to a plate with identical dimensions to the plug-flow apparatus wall. One layer of 3 mm beads was placed in the guide in an HCP configuration. 1 mm beads were placed in the interstitial areas of the 3 mm layer. The loaded bead guide was then placed against the inside of the apparatus wall with the 1 mm sub-layer against the wall. While holding the guide firmly against the wall, the apparatus was inverted so that the back of the guide was facing up. The guide was carefully removed, allowing the 1 mm and 3 mm beads to maintain HCP configuration. Subsequent layers were then loaded according to the bead loading protocol.

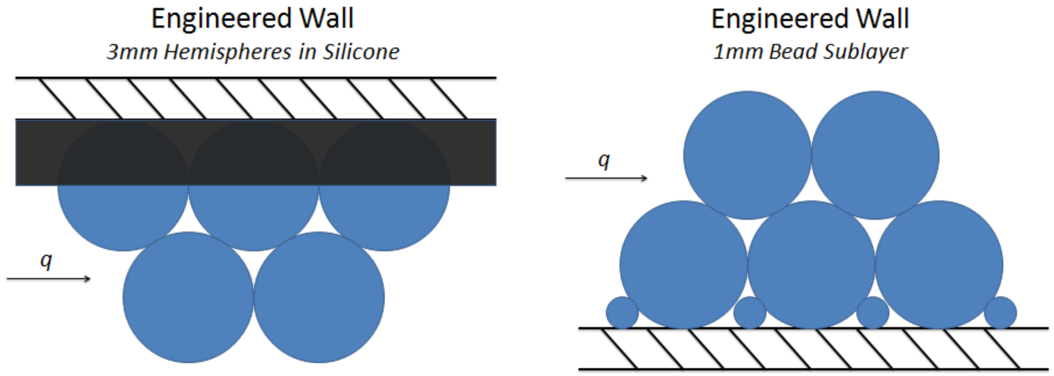

Figure 12**:** Schematic of 3 mm beads pressed into silicone, effective-hemispheres, for the top wall (left) and transparent 1 mm bead sub-layer for the engineered bottom wall (right).

Along the transparent bottom wall, the resulting mean bead diameter was lower than that in the field. By the Kozeny-Carmen equation, expected permeability along the wall would be slightly lower than that in the field, leading to lower dispersion. This was not a perfect solution, however dispersion along the wall lower than dispersion in the field was preferable. Higher dispersion at the wall could lead to dye permeation into high hydraulic conductivity zones ahead of the advancing plume (Fig. 13). A lower dispersion at the wall would cause a lingering tail behind the advancing dye front, but higher hydraulic conductivity zones in the field would not retain dye. Additionally, transverse dispersion along the engineered wall would be mitigated due to the direction of the dispersive gradient. For the smooth wall with higher dispersion, transverse dispersion would be allowed to permeate the interior. In the EIE apparatus, erroneous results caused by low dispersion could be quantified and would be confined to the pore space between the wall and one half of one bead diameter away from the wall. Conversely, smooth walls with higher dispersion could lead to system wide errors and would be difficult to accurately quantify.

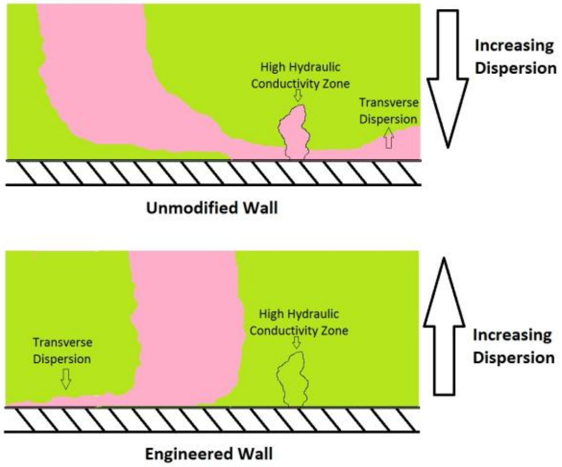

Figure 13: Error caused by high dispersion along the smooth wall (top) verses error caused by low dispersion along the engineered wall (bottom)

Wall mitigation strategies were tested using the one-dimensional plug flow apparatus. Preferential flow along the walls were largely mitigated, as observed near the engineered bottom walls in Figure 14; the intensity profile for the region near the engineered wall more closely resembles that of the field when compared to the smooth wall at the top of the apparatus. Overall, the 1 mm bead sub-layer technique did lead to dispersion that was slightly lower than that in the field. The hemisphere technique lead to dispersion that was slightly higher than that in the field. Though the mitigation techniques worked imperfectly in preliminary experiments, in the context of future EIE experiments, the mitigation techniques should improve the accuracy of quasi-two-dimensional apparatus experiments.

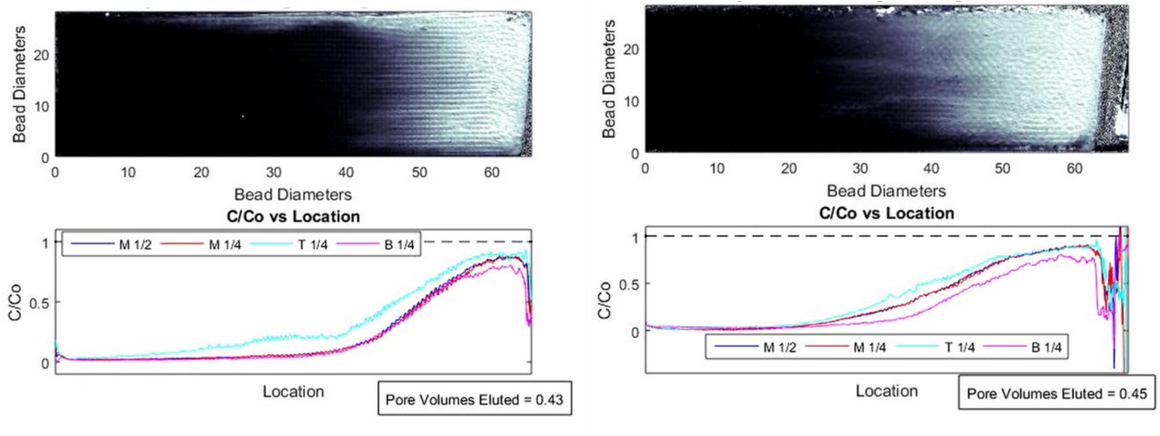

Figure 14: Wall effect mitigation with engineered walls. On the left, the bottom wall uses a 1mm bead sub-layer technique, the top wall uses a soft silicone wall applied dry. On the right, the top wall uses a silicone layer applied wet, the bottom wall uses a 1mm bead sub-layer. In both of the plots, M ½ refers to the middle half of the porous media field, with averaging transverse to flow, M ¼ refers to the middle quarter, T ¼ refers to the top quarter, and B ¼ is the bottom quarter.

3.4 Quasi-Two-Dimensional EIE

3.4.1 Apparatus Overview

The quasi-two-dimensional engineered injection and extraction (EIE) cell was designed to replicate previous numerical simulations created by the collaborative numerical team. The cell was designed to make Darcy rather than pore-scale measurements. Measurements were averaged through a 13 layer thickness of beads, making this a “quasi” two-dimensional cell (Fig. 15).

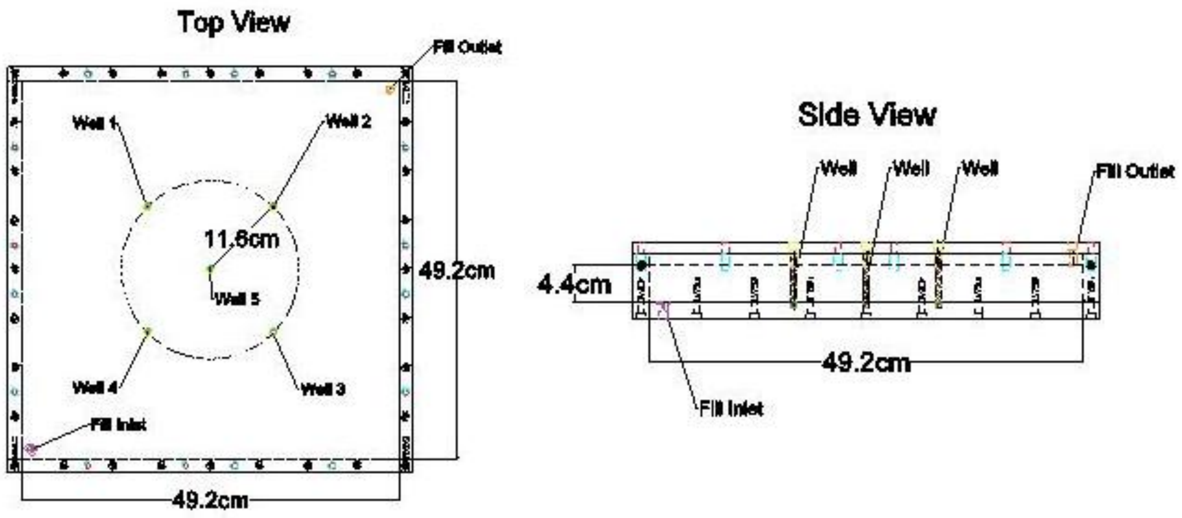

Figure 15: Dimensional schematic of EIE apparatus.

Overall dimensions of the cell were approximately 50 cm x 50 cm x 5 cm (160 x 160 x 15 bead diameters). Injection/extraction wells were fully screened, and penetrated the entire 5 cm thickness of the cell. There was a well located in the center, with four equally spaced wells surrounding the center well at a radius of 11.6 cm (37 bead diameters). The top and bottom walls of the cell (parallel to flow) used engineered walls to limit preferential flow along the wall. Flow entered the wells from one side, and was supplied by a positive displacement plumbing system containing five high accuracy syringe pumps (Fig. 16). The bottom of the cell was illuminated by using two scanning mirrors. The camera was located next to the scanning mirrors, and captured images from the same side as the incident light.

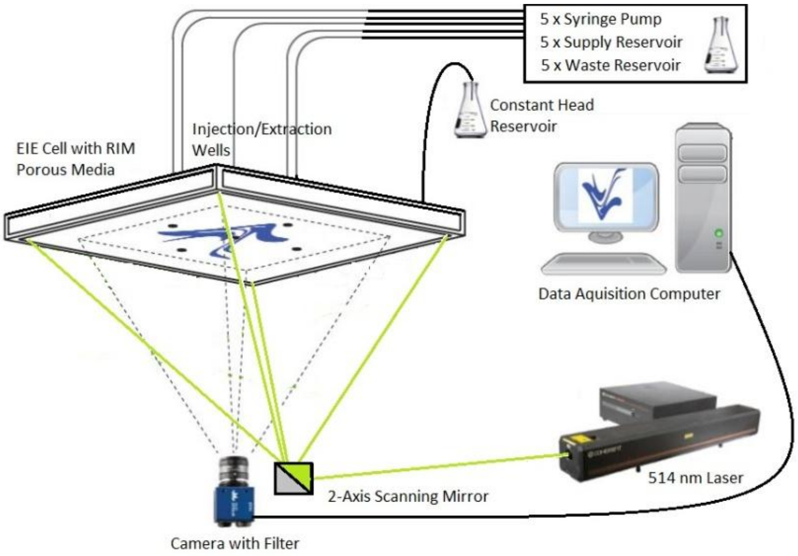

Figure 16: Quasi-two-dimensional EIE apparatus setup

3.4.2 Apparatus Components

The test section was designed to include five injection and extraction wells. Fluid could be injected or extracted from the top of each well. Well design used 6.35 mm diameter, 0.635 mm wall perforated tubing (Perforated Tubes Inc., code 70), with 1.3 mm perforations, giving an overall open area of 66%. The tubing was strong enough to resist deformation by the surrounding porous media. In order to further increase the open area, additional 1.3 mm holes were drilled into the perforated tubing, further increasing open area to approximately 70% which did not effect the structural integrity of the tubing under the demands of the EIE experiments.

To ensure uniformity with depth, it was important that the well elute fluid at an equal flowrate from top to bottom while penetrating the surrounding porous media. In order to accomplish this, the well screen must allow fluid to flow freely with minimal headloss as compared to the headloss contributions from the surrounding porous media. An apparatus was built to test the wells. This apparatus held two wells, each of which had injection/extraction access through the top, bottom, or top and bottom of the well. Pyrex beads were packed into the apparatus by vibration, leading to a random close pack media configuration. Well testing was performed by multiple dipole pumping experiments, alternating the orientation of inlets and outlets from the top to the bottom of the wells for each experiment (Fig. 17). For this experiment, there were no attempts to mitigate wall effects and porous media packing was not homogenous. Therefore, well flow uniformity would be based upon flow biases caused by the direction of pumping. It was found that dye plume fluid dynamics were identical, regardless of whether inlets and outlets were located at the top or bottom of each well. This was an indication that the wells eluted fluid uniformly over the depth, with little head loss along the well length.

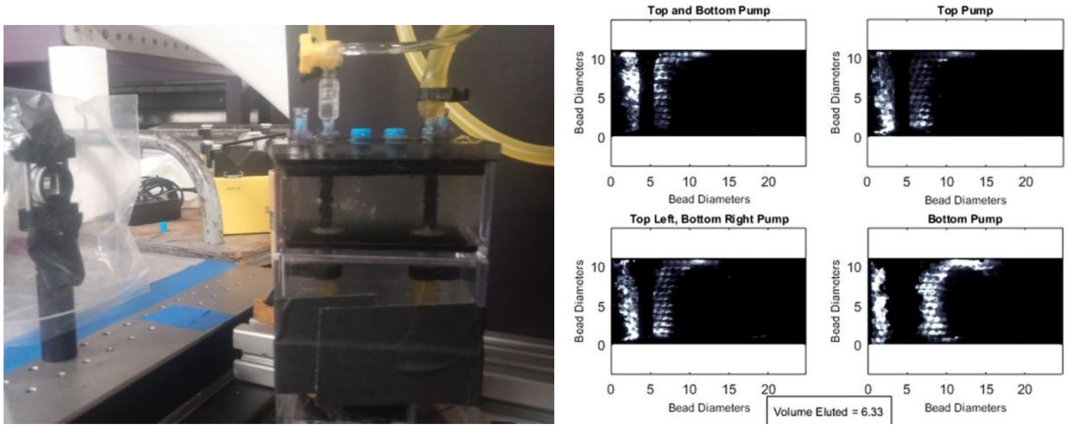

Figure 17: Well testing apparatus (left). Results of dye pumping from different ends of the well (right). Note that these images had different pumping start and stop times, so the dye fronts have advected different distances. These results are more clear as shown in a video, however the shape of the dye fronts are similar, showing uniform flow through the wells.

Injected volume had to equal extracted volume during the pumping sequence. Syringe pumps (Kd Scientific, Legato 270) used for intra-venous injection for the medical field were chosen for this task. Each pump held four syringes (BD, 60 mL luer lock syringe). For a single throw, two of the syringes injected fluid as the other two syringes simultaneously extracted fluid at an identical flowrate. The pumps were reversible and programmable, allowing continuous periodic injection and extraction. Since the combined volume of the two syringes supplying flow to injection or extraction was limited to 120 mL, a system of check valves was designed to fill the extracting syringes with source fluid as the injecting syringes supplied flow to the apparatus wells. The syringe pumps were programmed to instantaneously change direction once the extracting syringes had been completely filled, so that the former extraction syringes could then supply the wells and the former injection syringes could then draw from the fluid source. Three-way valves were also added to the plumbing loop, allowing for the selection of injection or extraction for the specific well (Fig. 18). The system was designed to minimize the volume of recycled fluid by the system, such that fluid drawn from a well was not re-injected later in the experiment. Valves were linked with transparent, semi-rigid poly-vinyl chloride tubing (Vyplas, part# TDX73-CAO).

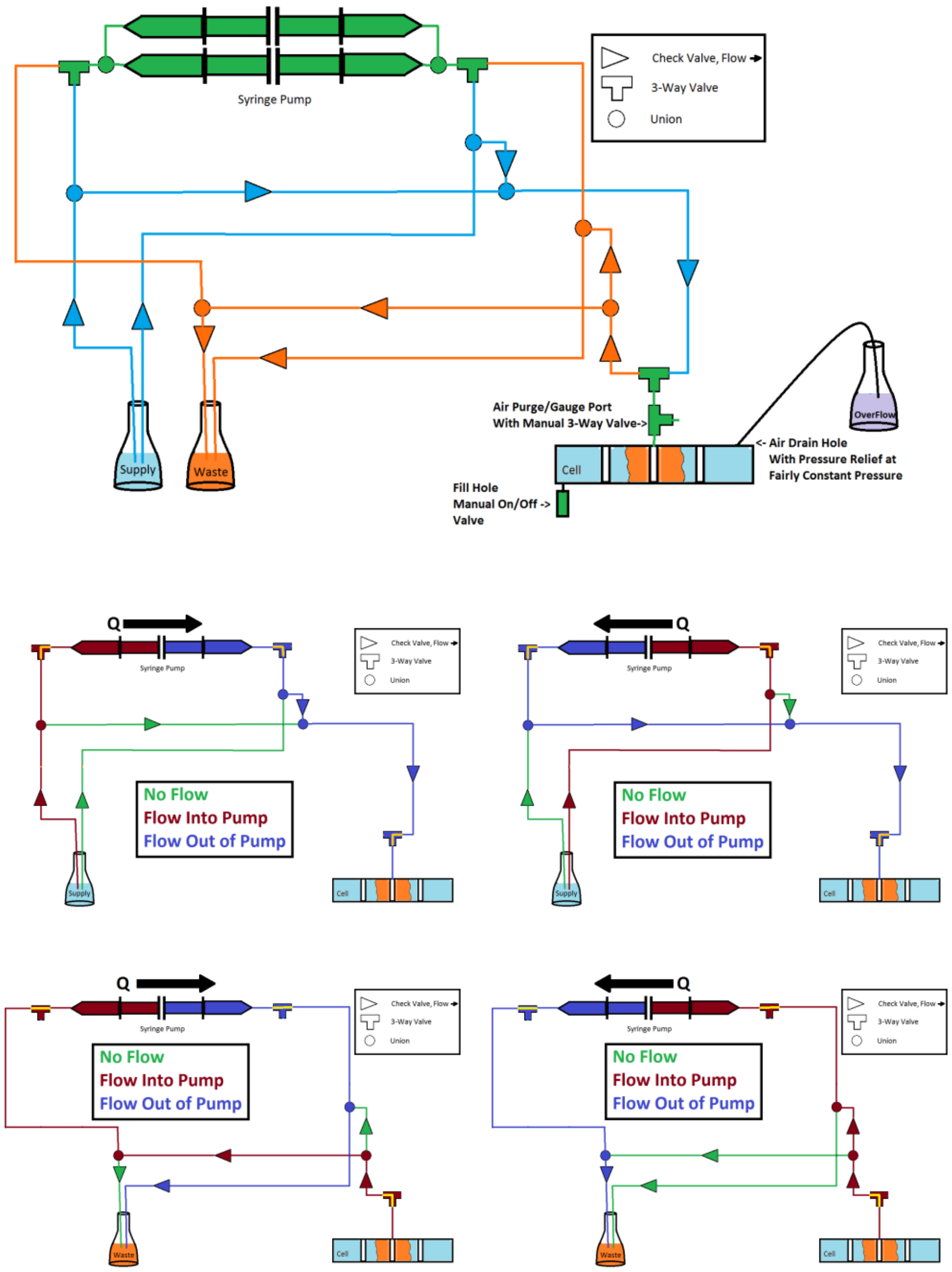

Figure 18: Pumping system schematic. Full setup (top), injection loop (middle), extraction loop (bottom)

After extensive testing by measurement of eluted volume through the pumping system, corrections were made for system compliance (hydraulic capacitance) caused by tubing elasticity and check valve triggering volume. Corrected pumping rates were programmed into the syringe pumps. Further volumetric testing of the system confirmed acceptable accuracy, with errors less than 0.3% between tests. With the potential for pumping error in mind, the EIE apparatus was designed with a constant head reservoir, allowing the apparatus to maintain constant pressure regardless of volumetric flux.

To mitigate wall effects, engineered apparatus walls were used in all EIE experiments. For the top face of the EIE apparatus, it was not necessary to preserve optical access. As described in section 3.3.4, a 3 mm thick layer of wet silicone was pressed into the top layer of pre-loaded HCP beads, then allowed to dry. In order to preserve optical access through the bottom wall of the apparatus, it was necessary to use the 1 mm bead sub-layer approach described in section 3.3.4. The 1 mm bead sub-layer required the development of specialized equipment and techniques (App. 8.3). With the placement of the first layer of 3 mm beads complete, the subsequent layers of HCP beads could then be packed into the EIE cell.

A total of thirteen layers of 3 mm beads were packed into the EIE apparatus, comprising the imaging depth over which subsequent quasi-two-dimensional data would be averaged. Three additional layers of opaque beads were loaded in an HCP configuration on top of the thirteen transparent layers. Though the hemisphere in silicone wall mitigation technique seemed effective, there was a chance that bead HCP configuration could be misaligned upon installation of the EIE apparatus lid. By including three layers of opaque beads, any irregularities in flow near the wall would not be imaged during experiments, further ensuring porous media uniformity over the depth of the imaged domain.

Opaque beads were fabricated by painting the 3 mm Pyrex beads in a specially constructed fluidized-bed apparatus. This painting technique produced a thin and even painted surface on the beads, assuring consistent spherical shape and conformance to the standard 3 mm sphere diameter. Tests were carried out to confirm that the painted surface was durable, so that paint would not contaminate the glycerin during EIE experiments.

The EIE apparatus allowed optical access only through the bottom face of the cell. With this configuration it was necessary to modify the LIF imaging techniques described in section 3.3.2., in which a laser sheet was passed through one window and imaging from a separate window perpendicular to the path of the laser. The imaging area for the EIE apparatus was approximately 0.5 m x 0.5 m, a cross-section too large to pass a coherent laser beam for accurate LIF imaging. However, the imaging depth of the EIE apparatus was only 3.5 cm, well under the maximum probe depth of 10 cm discussed in section 3.2. Therefore, it was decided that the best strategy for execution of LIF would be based on passing the laser through the same face of the apparatus as that through which the image would be captured. This means that the camera would be located next to the incoming laser beam.

In order to evenly illuminate the entire test section, a similar technique was used to that described in section 3.3.2. The 514 nm laser was first passed through a beam expander to produce a 1 cm diameter beam. The expanded beam was then manipulated be reflection off of a two-axis galvo-mirror (Thorlabs, dual-axis scanning-galvo-mirror system, GVS312). The LabVIEW code controlling the mirrors was setup to sweep the beam over every point in the imaging domain. Starting from the top, right corner of the EIE apparatus imaging window, the beam would scan horizontally to the left, move vertically down 0.25 cm, scan horizontally to the right, move 0.25 cm down, then continue the pattern until reaching the bottom left corner of the imaging domain. Each image was captured using a one second exposure time, equal to the duration of one complete scan of the domain by the laser. Images were captured every 15 seconds, a sufficient frame rate to capture the transient fluid dynamics of the EIE system.

3.4.3 Apparatus Setup

Physical setup of the experiment is shown in figure 19. An extruded aluminum frame held the EIE cell, galvo-mirrors, and camera. The frame was attached to an optics table which held the laser, beam expander, and beam positioning mirrors. The frame extended approximately 2 m from the camera mount. The 2 m focal distance from the EIE cell to the camera minimized parallax within captured images, ensuring that the quasi-two-dimensional assumption was valid. Five syringe pumps were each attached to the pumping systems described in section 3.4.2., which were in turn attached to the top of the EIE cell. In order to reduce vibration, the pumping system panel was not attached to the optics table, or to the EIE frame. A beam block was attached to the sides of the EIE frame for safety and to minimize stray light within the imaging path.

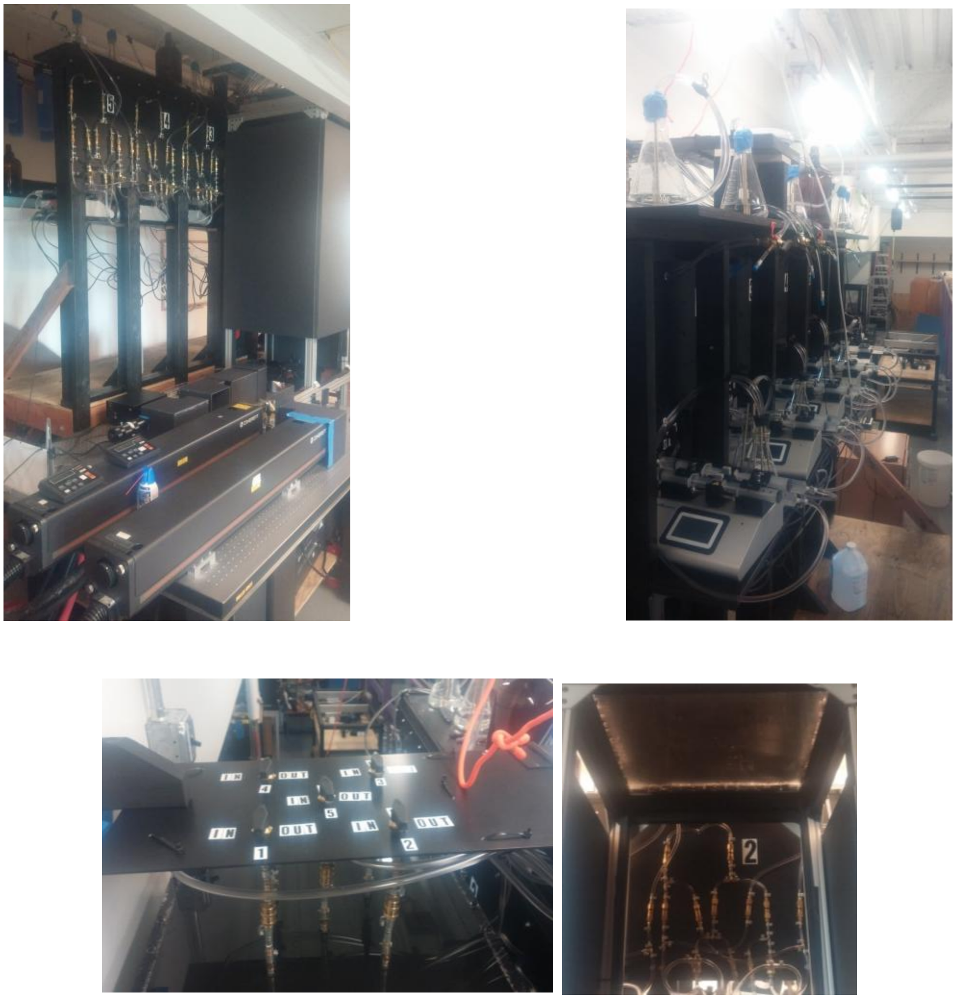

Figure 19: Physical setup of EIE experiment. Optics bench, EIE frame, and fluid conveyance system front panel (top left). Fluid conveyance system back panel and syringe pumps (top right). EIE cell coupling to fluid conveyance system (bottom left). EIE apparatus imaging window as seen from underneath (bottom right).

3.4.4 Experimental Procedure

Prior to an EIE experiment, new fluid was cycled through the pumping system, ensuring that all air was purged from the system. The laser and camera were then turned on and allowed to warm up for one hour before any images were captured. All light sources inside the laboratory were turned off or shrouded. A blank image of the porous media domain with no dye in the system was then captured for post-experiment image correction.

20 mL of the dye solution was collected using a 60 mL syringe fitted with a quick release valve that coupled with the well inlets on the EIE cell. The EIE cell was temporarily disconnected from the pumping system. The syringe containing the dye was then connected to the center well and dye was slowly injected at a rate of approximately 4 mL/min, allowing clear fluid to be expelled into the atmosphere through the surrounding wells. All wells were then reconnected to the pumping system. The valve for the constant head reservoir was opened. The syringe pump and valves for the center well were then engaged to allow 7 mL of clear fluid to be injected into the well, clearing dye from the plumbing directly upstream from the well. Pumps were programmed and three-way valves were set to the desired configurations for the first step in the EIE sequence. Image capture and pumping was then started. Upon completion of the first EIE sequence step, image capture was stopped, then pumps were reprogrammed and valve configuration was selected for the next EIE sequence step. Image capture was reinitiated and pumps were started. Upon completion of all steps within the EIE sequence, pumps and valves were set to extract from the center well while injecting through the surrounding wells. Fluid was drawn from the center well until there was no dye left in the imaging domain. By extracting all dye from the cell, subsequent EIE experiments could be performed using an identical porous media configuration.

After collecting data for all of the EIE sequences, and any other experiments that used the specific bead configuration within the EIE cell, the apparatus was flooded with dye. All loops in the fluid conveyance system were initially filled with dye solution at a known concentration. Pumps and valves were set to inject dye through the center well. The EIE cell fill port and constant head reservoir port were used as outlets for excess fluid. Three pore volumes of dye solution were injected into the system. Complete dye saturation of the pore space within the radius of the outer wells was confirmed by observation of no change in concentration with time. Images were collected during dye flooding for later review. The dye-saturated images collected at the end of this experiment were then used for image correction and for porosity mapping.

Upon completion of EIE experiments and dye flooding, an image correction technique similar to that described in section 3.3.2. was performed. However, for EIE experiments the saturated image was captured during a separate experiment, so slight variations were necessary. For calculation of $I_o(i,j)$, a specific blank, $B_S(i,j)$, was subtracted from the dye saturated image, $S(i,j)$:

$$I_o(i,j) = S(i,j) - B_S(i,j) \tag{20}$$

The background-corrected, dye-saturated light intensity image, $I_o(i,j)$, represents the light intensity produced by the maximum dye volume possible within the domain, at the source concentration.

The background-corrected raw light intensity image is then divided by the background-corrected dye-saturated image, providing an image for instantaneous light intensity concentration, $I(i,j)$, over dye-saturated intensity concentration, $I_o(i,j)$. The resulting image corrects for all light intensity fluctuations that are not caused by changes in dye concentration.

$$\frac{C}{C_o}(i,j) = \alpha \frac{R(i,j) - B_R(i,j)}{S(i,j) - B_S(i,j)} \tag{21}$$

Since images for $I(i,j)$ and $I_o(i,j)$ are captured at different times, dye concentrations, and laser power, it is necessary to calibrate instantaneous concentration to initial concentration by multiplying $\frac{I}{I_o}\ (i,j)$ by a constant, α. Upon correction, non-dimensional intensity concentration can be considered equivalent to non-dimensional scalar concentration, $\frac{C}{C_o}\ (i,j)$. The calibration variable α is found by tuning α such that the total volume, V_{Image}, found in image $\frac{C}{C_o}\ (i,j)$, is equal to the volume that was physically injected into the apparatus to create the initial dye plume, $V_{Injected}$, by using equation 20.

$$V_{Image} = b \int \frac{C}{C_o}\ (i,j) n\ dA = V_{Injected}, \qquad (22)$$

with n equal to porosity, b equal to apparatus depth, and $V_{Injected}$ equal to the volume of dye injected into the apparatus.

Finally, the mass assigned to the numerical model is also matched to $V_{Injected}$ from the experiments. By matching masses, the experiment and numerical simulations will have synchronous initial conditions, facilitating comparison of the two simulations.

In order to quantify the plume dynamics captured within the corrected images, two strategies were employed. The first strategy involved taking a vertically averaged slice of concentrations across the width of the image. As shown in figure 20, the vertical average was taken over the middle centimeter of the image. The vertically averaged slice could then be compared with duplicate EIE images, as well as numerical models. The second strategy involved a radial average of concentrations around the center well. As seen in figure 21, the radial average shows the average concentration at a given radius, as it is rotated through the domain. With this method it is important to note that deviation in concentration is more pronounced with proximity to the center well due to the smaller arc length of the radial sweep.

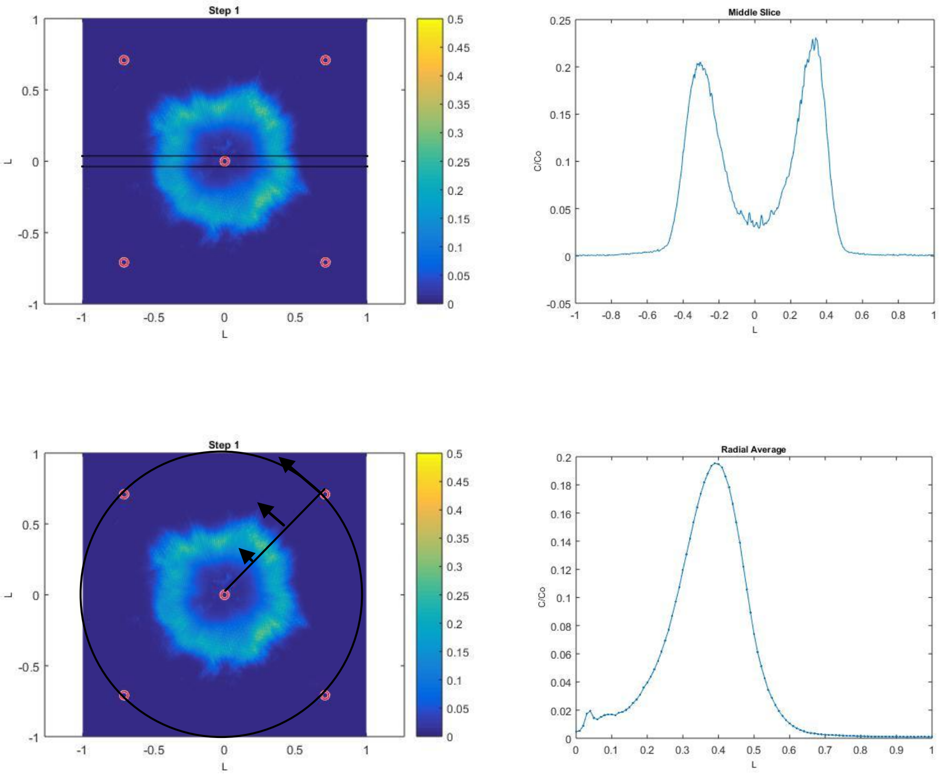

Figure 20: Vertically averaged horizontal concentration profile slice, region of interest (top left), profile (top right). Radial profile of average concentration, region of interest (bottom left), profile (bottom right).

3.4.5 Numerical Methods

The test section was numerically modeled as a confined two-dimensional, isotropic aquifer. Groundwater flow patterns were modeled by using the groundwater flow equation for a confined, isotropic aquifer,

$$S_S \frac{\partial H}{\partial t} = \nabla \cdot KH + \sum_{j=1}^{N_W} Q_j(t)\delta(\boldsymbol{x}-\boldsymbol{x}_j), \tag{23}$$

where $\boldsymbol{S_S}$ is specific storage, $\boldsymbol{Q_j}$ is the injection rate in well j, $\boldsymbol{x}$ is a spatial coordinate, $\mathbf{x_j}$ is the spatial coordinate of well j, $\boldsymbol{N_W}$ is the number of wells, and $\boldsymbol{\delta}$ is the Dirac delta function. The flow equation was solved numerically using MODFLOW, a standard groundwater flow simulation program. Scalar transport was solved numerically using the random walk particle tracking code, RW3D. For more information on numerical modeling procedures, see Reising (2018).

3.5 Two-Scalar EIE

3.5.1 Methodological Hypothesis

As shown in Section 4 of this thesis, EIE results were highly reproducible. Reproducible results were made possible by rigid porous media grains packed into a structurally stable HCP configuration, working in conjunction with the accurate fluid pumping system. This made development of a two-scalar imaging technique possible. In theory, a single dye species could be used to represent two scalars by performing two experiments that use an identical pumping protocol. In order to make the technique work, each experiment would need to start with an initial condition matching that of one scalar. For the first experiment, an initial dye plume would be injected, representing the contaminant, followed by injection of clear fluid, representing the treatment scalar. The clear fluid injection will cause dispersion in the contaminant plume equal to that caused by injection of a true scalar. The EIE pumping protocol would then be applied. In the subsequent experiment, only an injection of dye, representing the treatment scalar, would comprise the initial condition. The identical EIE pumping protocol would be applied to the system. Data from the two experiments could then be superimposed, allowing consideration of scalar mixing caused by the EIE sequence. This process is shown graphically in figure 21.

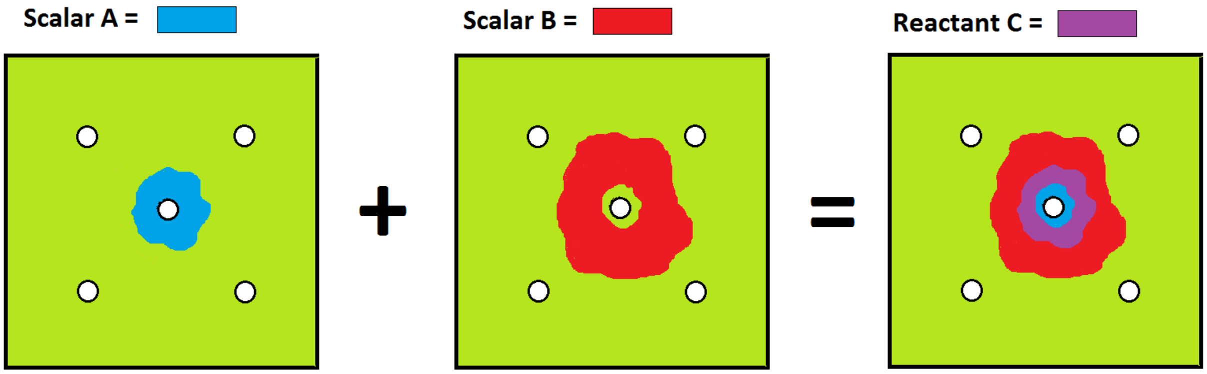

Figure 21: Two-scalar LIF. Scalar A is imaged separately from Scalar B. When the two images are combined, the overlapping area of the scalars indicates Reactant C. This method assumes a very low Damköhler number.

This technique did not cause a physical reaction. Therefore the mass of each scalar was conserved throughout execution of the EIE sequence. It follows that this technique represented a very slow reaction rate, i.e. an extremely low Damköhler number. In the combined image, locations in which the two scalars overlap would indicate reaction potential. Given infinite reaction time in this configuration, the reaction would occur as shown in a given step.

3.5.2 Experimental Procedure

The experimental procedure for this technique closely followed that described for all other EIE experiments. However, the initial conditions were different. For the initial scalar experiment, the dye injection volume was 10 mL, half of that injected into single-scalar experiments. The dye injection was then followed by a 10 mL injection of clear fluid. The well was reattached to the fluid pumping system and 7 mL of clear fluid was injected, as if clearing dye from the upstream plumbing. The EIE protocol was then imaged in its entirety.

The subsequent experiment represented the fluid dynamics of the treatment scalar plume. 10 mL of dye was injected into the center well. The well was then reattached to the fluid pumping system and 7 mL of clear fluid was injected. The identical EIE protocol was imaged in its entirety. Image correction was performed for each experiment in the same manner described in section 3.4.4. Corrected images were then analyzed in tandem to provide data for two-scalar mixing dynamics.

3.5.3 Validation of Technique

The two-scalar experiment, used the identical pumping protocol to that used in one of the single scalar EIE experiments. As shown in figure 22, superimposed images for scalars A and B from the two-scalar experiment matched the plume dynamics imaged in the corresponding single-scalar EIE folding experiment, validating the technique in terms of overall plume dynamics. As shown in figure 23, the two-scalar method was also validated by a separate, true two-color experiment. This experiment used two different fluorescent dyes, accompanied by two different camera filters, closely following the method used in Soltys, 2011. While this was a qualitative match, mass for the two-dye experiment was not conserved throughout the EIE sequence, attributable to incomplete dye mixing prior to injection into the EIE cell and camera filter misalignment between steps. Consult appendix section 8.2 for more data from these experiments.

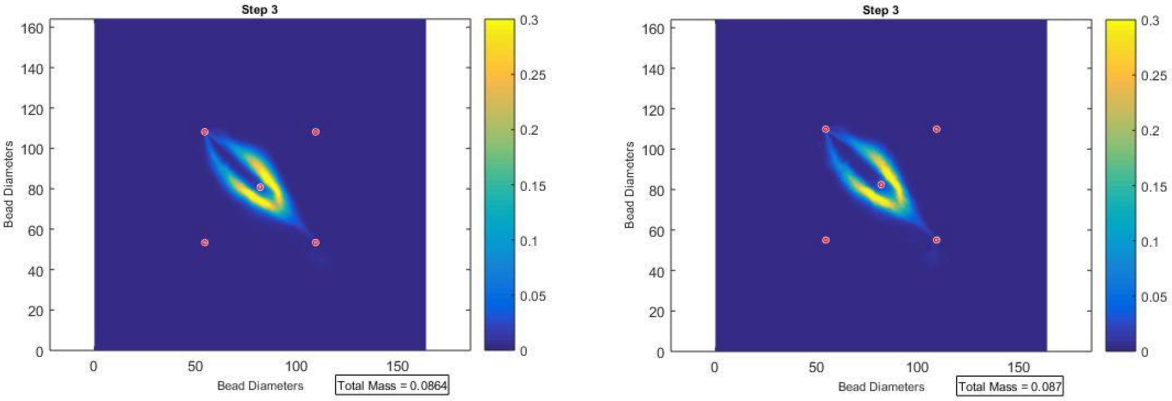

Figure 22: Comparrison of plume dynamics. Superimposed inner and outer plume from single-dye, two-scalar experiment (left). Image from single-dye, single-scalar experiment (right).

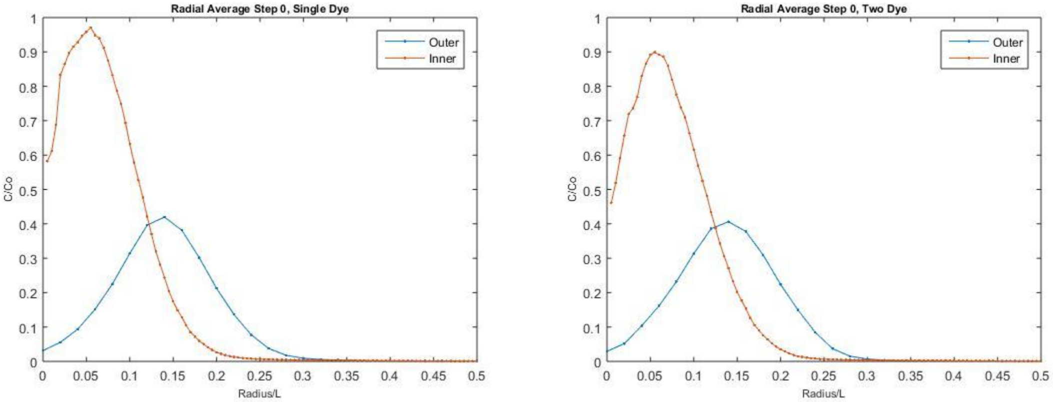

Figure 23: Comparison of radial profiles. Inner and outer plume profiles from single-dye, two-scalar experiment (left). Inner and outer plume profiles from two-dye, two-scalar experiment (right). Slight variations in mass are due to incomplete dye mixing or filter misalignment for two-dye experiment.

4. Results

Five distinct experiments were carried out using the quasi-two-dimensional EIE apparatus, all using the same porous media packing. Experiments included porosity mapping, oscillating EIE, folding EIE, push-pull EIE, and a two-scalar folding EIE. Presentation of each EIE sequence will be partitioned by pumping sequence step, with a total of four to five steps per sequence. Pumping volumes will be presented as pore volumes, defined as the volume of the apparatus contained within the radius L (11.6 cm), over a depth of 3.5 cm, and divided by system porosity, 0.31. The motivation for each experiment will be presented, followed by a table showing the number of pore volumes injected or extracted for each well during a given step, plume images for $\frac{C}{C_o}$ from the experiments with replicates and corresponding images from the numerical simulations, and finally quantitative analysis of the data. Axes for all plume images are identical, as such, axes will be presented for the porosity map, but will be omitted for subsequent images.

The pumping sequence tables are each presented with a legend (Fig. 24). This legend shows the orientation and corresponding number of each well used in the EIE sequence. Note that the radial dimension L has been included on the legend, with wells one through four equally spaced along the radius. Initial injection of the tracer plume (step 0) will be shown prior to presentation of the pumping sequence table.

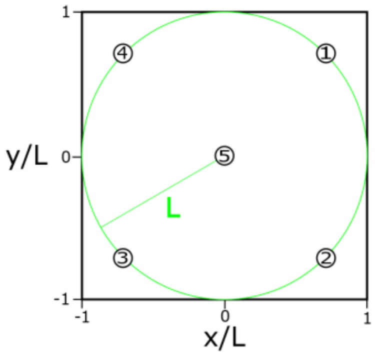

Figure 24: Pumping sequence legend

For quantitative analysis of EIE data, two approaches were used. Each approach will be indicated on quantitative plots with a distinct symbol (Fig. 25). For the radial averaging technique, circumferential averages of $\frac{C}{C_o}$ are presented for points along the radial coordinate, x/L. Please note that radial coordinates near the origin (near x/L = 0) used fewer points for the average, so spatial variations in $\frac{C}{C_o}$ will be more pronounced than they would be for larger values of x/L.

For plume configurations that were not axisymmetric, diagonal profile slices are presented (Fig. 25). These slices are aligned with the wells, showing $\frac{C}{C_o}$ distribution from –x/L to x/L. These profile slices are three well diameters thick, i.e., $\frac{C}{C_o}$ is averaged perpendicular to the slice over the length of three well diameters (equal to 0.08 L). Profile slices were either taken between well three and well one, or well four and well two, depending on the orientation of the plume.

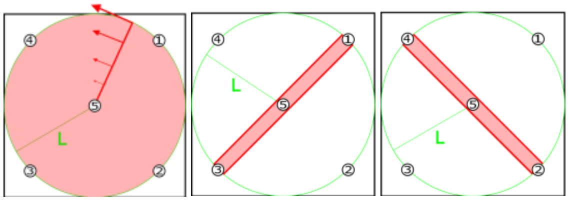

Figure 25: Symbols for radial averaging (left), and directional profile slices (middle and right)

Please note that measurements taken within the wells were not accurate. Due to the higher concentrations within wells, fluorescence intensity values were orders of magnitude higher than those in the porous media. In order to use the full dynamic range of the camera for measurements within the porous media, light-intensity values within the wells were allowed to over-saturate. As such, measurements within a radius of one well diameter of the well centers were not considered for quantitative analysis.

4.1 Porosity Map

The porosity map was created in order to provide critical information about spatial heterogeneity within the porous media field. Since all EIE experiments used the same porous media bed, the map applies to all experiments presented in this study. This map was used to gauge the degree of homogeneity achieved for the porous media packing, for system-wide mass calculations, and for calibration of $\frac{C}{C_o}$ values to those in the numerical results. For future work, this map can be used to model heterogeneity in the numeric simulations.

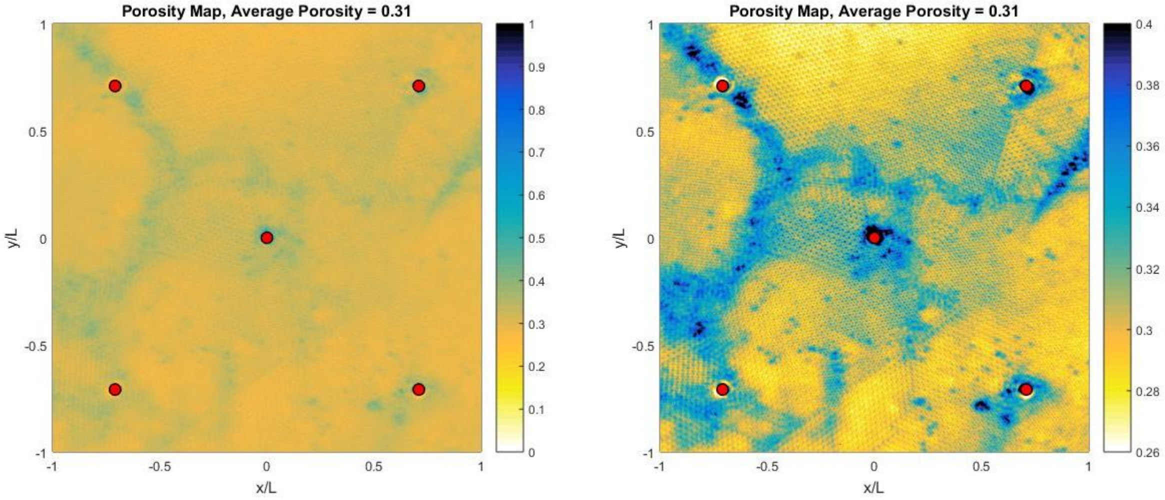

Figure 26: Porosity map. Shown with a scale from 0 – 1 (left) to illustrate the extent of homogeneity, and with a scale from 0.28 – 0.4 (right) to accentuate heterogeneity in the system.

The porosity within the apparatus as a whole was physically measured at 0.31. The image intensities were tuned to match the system porosity. Porosity fell within the range of 0.28 to 0.4 (Fig. 26). Areas with a high degree of homogeneity are apparent from even porosity distribution in the map. For the more homogenous regions, porosity measurements are near 0.28, which is close to the theoretical limit of 0.26. For the heterogeneous veins, most porosity measurements fell within the range of 0.32 and 0.38. All results look reasonable in comparison to information provided by other studies.

4.2 Push-Pull Sequence

This sequence was designed to simulate a common push-pull remediation technique, primarily using one injection/extraction well to provide flow forcings within the contamination zone. For this study, the push-pull sequence is useful for showing purely radial dispersion rather than the combination of longitudinal and transverse dispersion which would be present with other pumping regiments. The initial scalar plume was injected into well five, then cleared from the well with a small-volume clear fluid injection. For steps one through four, fluid was injected and extracted from well five with each of the surrounding wells pumping the negative value of one quarter of the volume injected or extracted for well five, ensuring a net-zero volume injection into the system.

Step 0: Wells 1 through 4 were left open to the atmosphere. 0.034 pore volumes of dye were injected into well 5 to create the initial plume.

Number of pore volumes injected per step:

	Well 1	Well 2	Well 3	Well 4	Well 5
Step 1	-0.038	-0.038	-0.038	-0.038	0.151
Step 2	0.013	0.013	0.013	0.013	-0.050
Step 3	-0.013	-0.013	-0.013	-0.013	0.050
Step 4	0.006	0.006	0.006	0.006	-0.025

Table 1: Push-Pull EIE Pumping Scheme

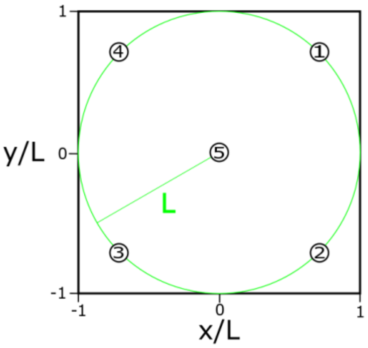

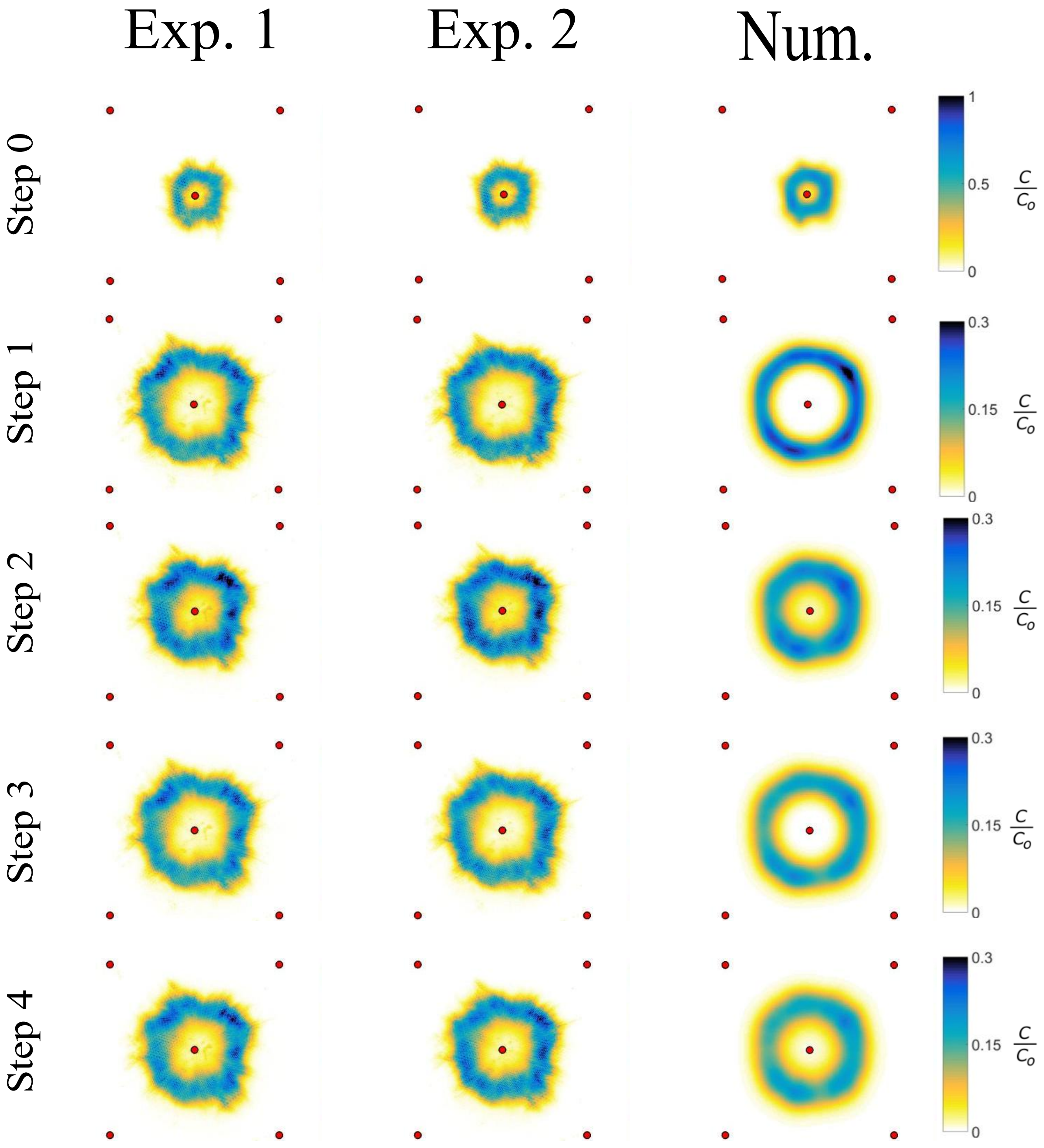

Figure 27: Experimental and numerical plume images of $\frac{C}{C_o}$ for Push-Pull EIE. Numerical data taken from Reising (2018)

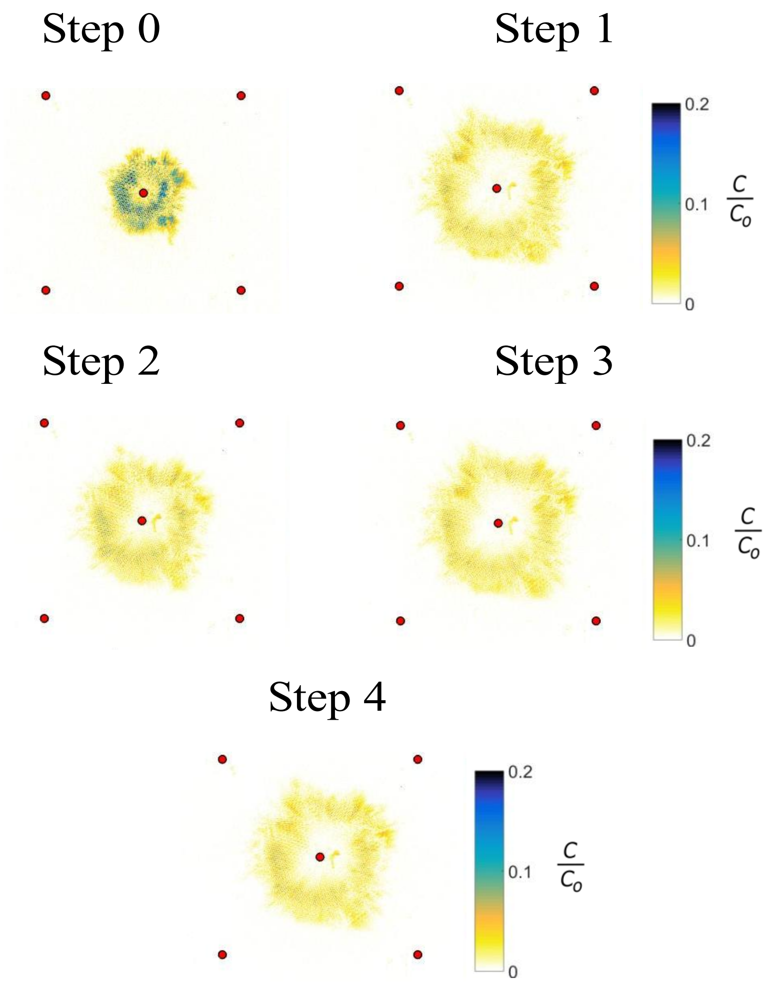

Figure 28: Differences in $\frac{\mathbf{C}}{\mathbf{C_o}}$ between experiment 1 and experiment 2 for Push-Pull EIE.

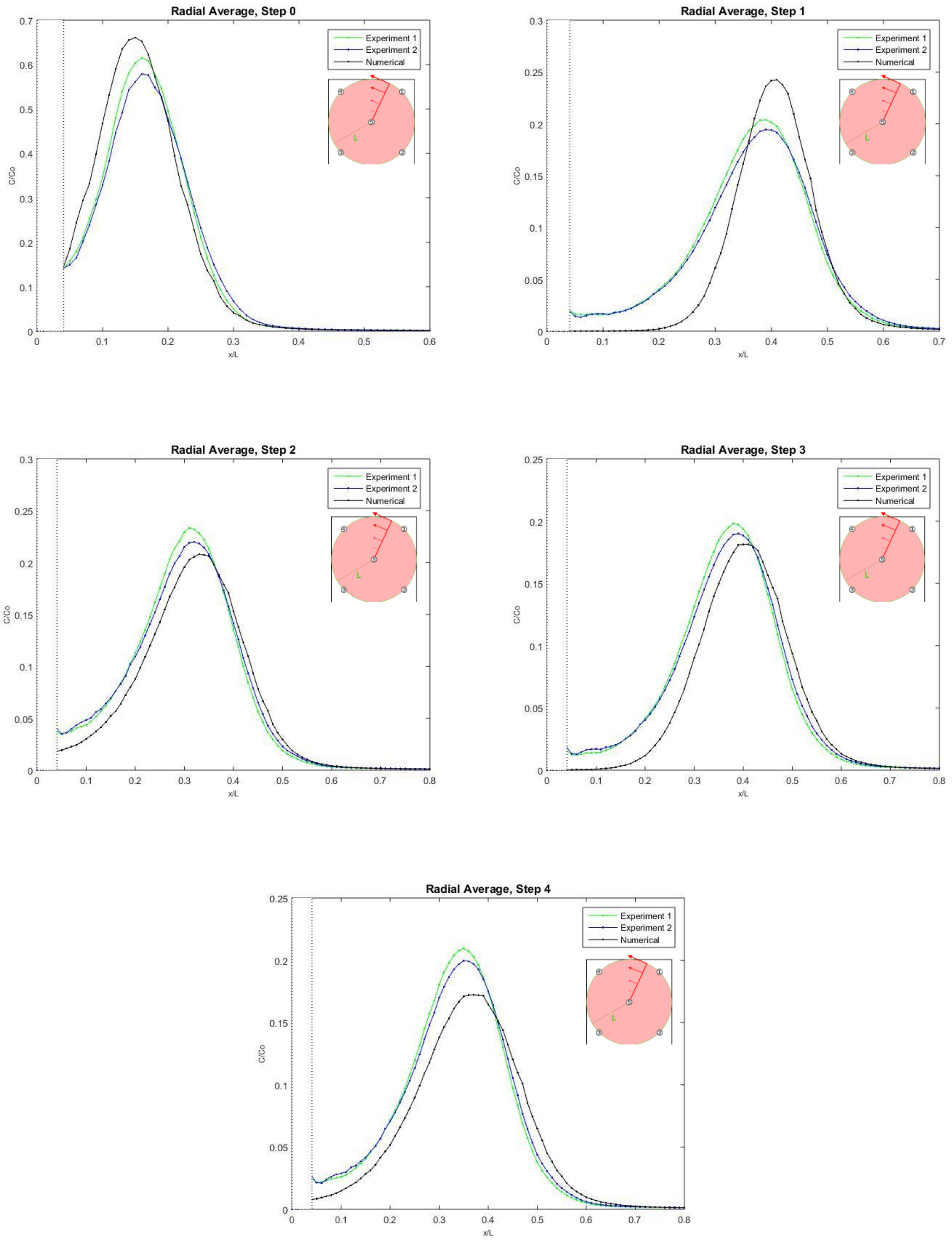

Figure 29: Radially averaged concentration profiles for Push-Pull EIE. Includes first & second experiments with numerical results. Numerical data taken from Reising (2018)

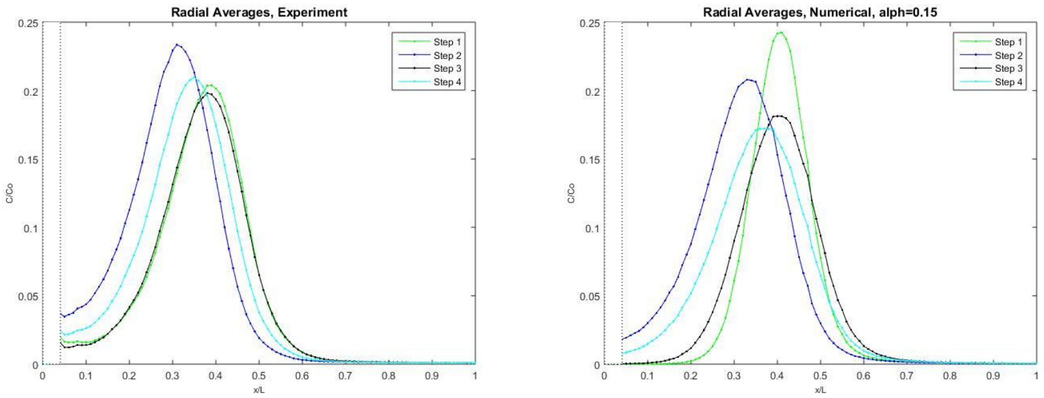

Figure 30: Combined radial profiles for steps 1 through 4 of Push-Pull EIE. Including experiment 2 and numerical results. Numerical data taken from Reising (2018)

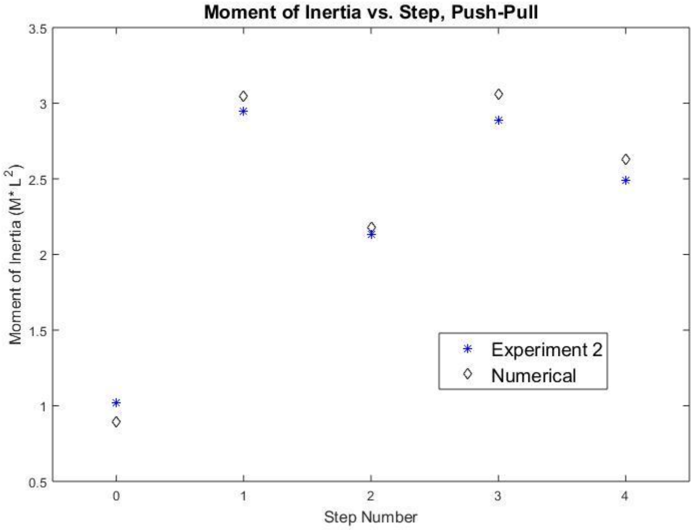

Figure 31: Moment of inertia by step for experiment 2 and numerical data, push-pull EIE.

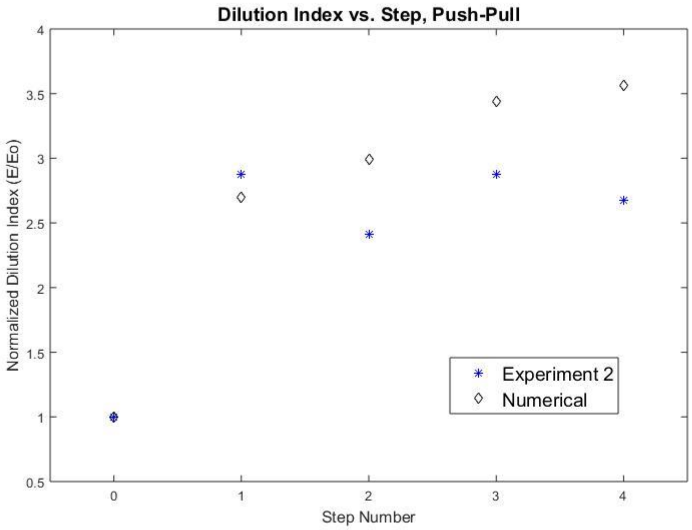

Figure 32: Dilution index by step for experiment 2 and numerical data, push-pull EIE. Normalized by the step 0 dilution index.

Plume dynamics are qualitatively identical between experiments one and two, and exhibit a high degree of agreement with the numerical model (Fig. 27). By plotting the absolute value of the difference in non-dimensional spatial concentrations in experiment 1 and experiment 2, a high degree of repeatability between experiments is apparent (Fig. 28). Experiments essentially conserve mass during the EIE sequences, with a 3.2% change in mass over the course of experiment 1 and a 3.6% change in mass over the course of experiment 2 (see appendix section 8.1 for step-wise mass values). Upon consideration of quantitative results, some discrepancies become apparent. Peak concentrations between the two experiments are slightly different (Fig. 29), which could be due to a slight mismatch in initial dye injection volumes or latent mixing effects within the well. However, this is a minor difference and as such, the experimental results can be considered essentially identical. The numerical concentration profiles in figure 29 show less agreement, starting with higher peak concentrations in early steps that appear to disperse too rapidly in later steps. Combined radial profiles from all steps (Fig. 30) show markedly different behavior in the numerical model, with peak concentrations that decrease with every step regardless of pumping direction. Moments of inertia in the numerical data show good agreement with the experiment (Fig. 31), indicating that the numerical model accurately describes plume spread. Dilution index for the numerical and experimental data match worse as the sequence progresses (Fig. 32), indicating a departure in mixing behavior. The experimental data suggests that peak concentrations can increase as the plume diameter is condensed via extraction from well five. This could be an effect of inaccurate dispersivity values in the model (for combined profiles with different dispersivities see appendix 8.1), dispersivity values that may require more specific longitudinal, transverse, and possibly radial tuning.

4.3 Oscillating Sequence

This sequence was created by the numerical modeling team with the intention of optimizing mixing. After initial scalar injection into well 5, the plume was radially spread by clear fluid injection into well 5 with corresponding extractions from wells 2 and 4. The largely circular plume was then stretched in steps 2 and 3. The elongated plume was then oscillated, perpendicular to the elongation, from side to side via dipole pumping with wells 1 and 3 during steps 4 and 5.

Please note, oscillating experiment #1 was the first EIE experiment performed. Upon consideration of the results, a number of improvements were made to the EIE apparatus. Improvements included an updated laser sweep code, a different camera lens, and most importantly, a larger volume initial dye injection. For these reasons, this sequence does not include a true experimental replicate. From a qualitative perspective, plume dynamics would appear to exhibit similar behavior. Numerical simulations were designed to match the initial scalar injection volume present in the second experiment.

Oscillation Pumping Sequence:

Step 0: Wells 1 through 4 were left open to the atmosphere. 0.027 pore volumes of dye were injected into well 5 to create the plume for the first experiment, 0.034 pore volumes were injected into well 5 to create the plume for the replicate experiment.

Number of pore volumes injected per step:

	Well 1	Well 2	Well 3	Well 4	Well 5
Step 1	0	-0.050	0	-0.050	0.101
Step 2	0.101	-0.101	0.101	-0.101	0
Step 3	-0.013	-0.013	-0.013	0.101	0
Step 4	0.202	0	-0.202	0	0
Step 5	-0.202	0	0.202	0	0

Table 2: Oscillating EIE Pumping Scheme

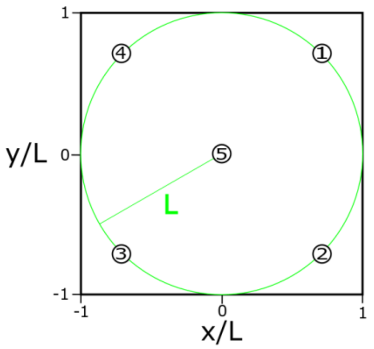

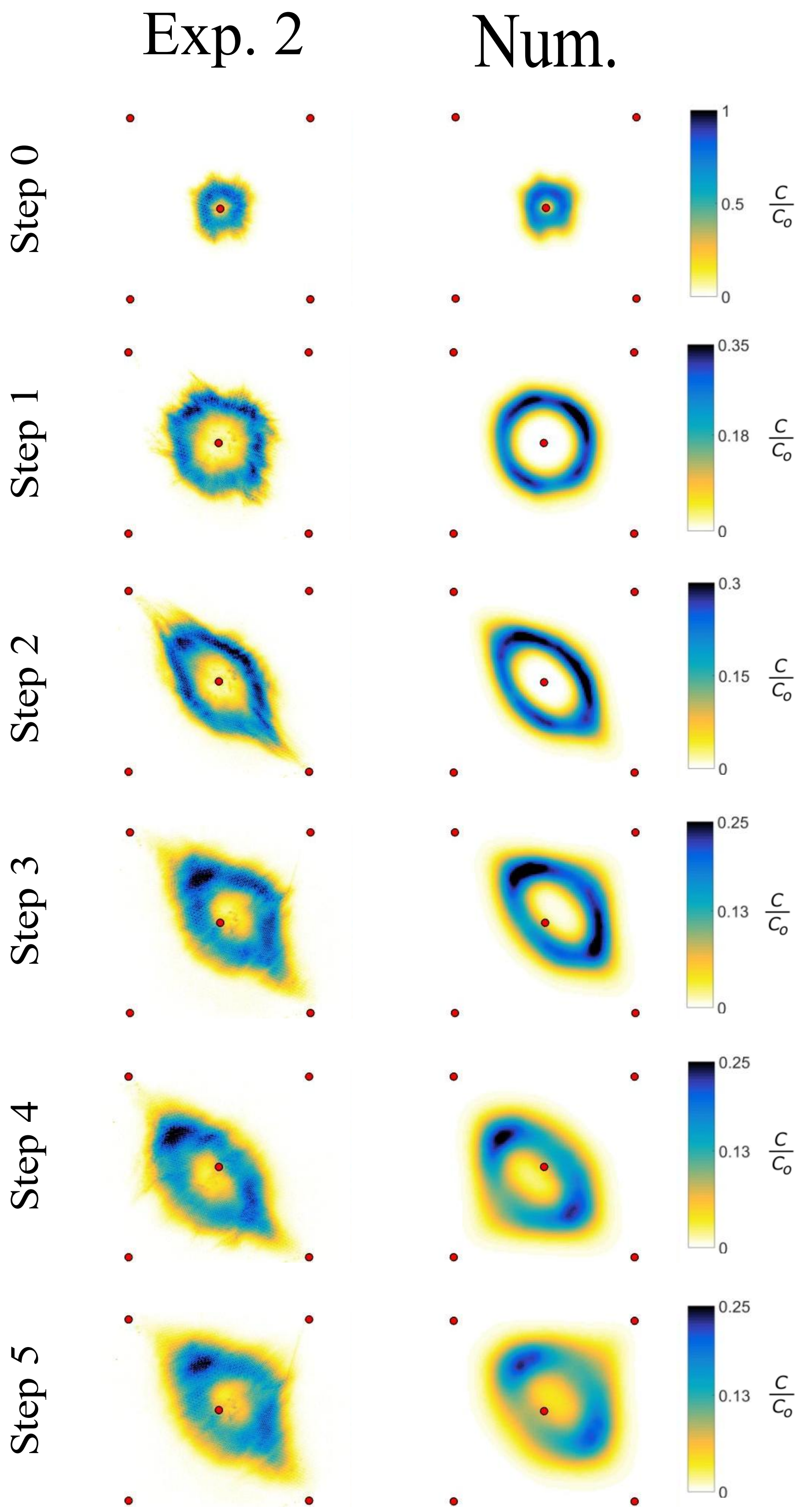

Figure 33: Plume images of $\frac{c}{c_o}$ for Oscillating EIE. Numerical data taken from Reising (2018)

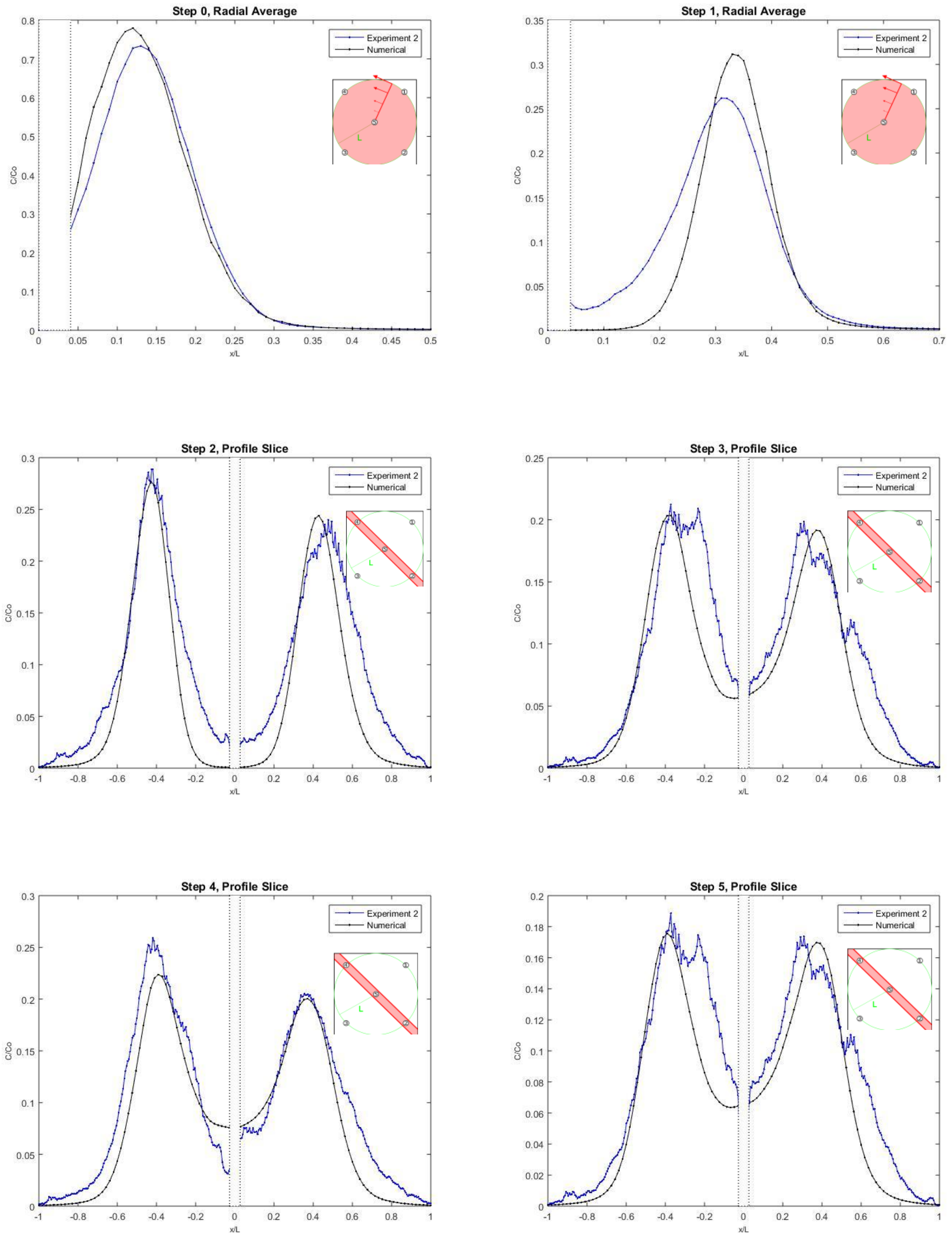

Figure 34: Concentration profiles for Oscillating EIE. Includes second experiment with numerical results. Numerical data taken from Reising (2018)

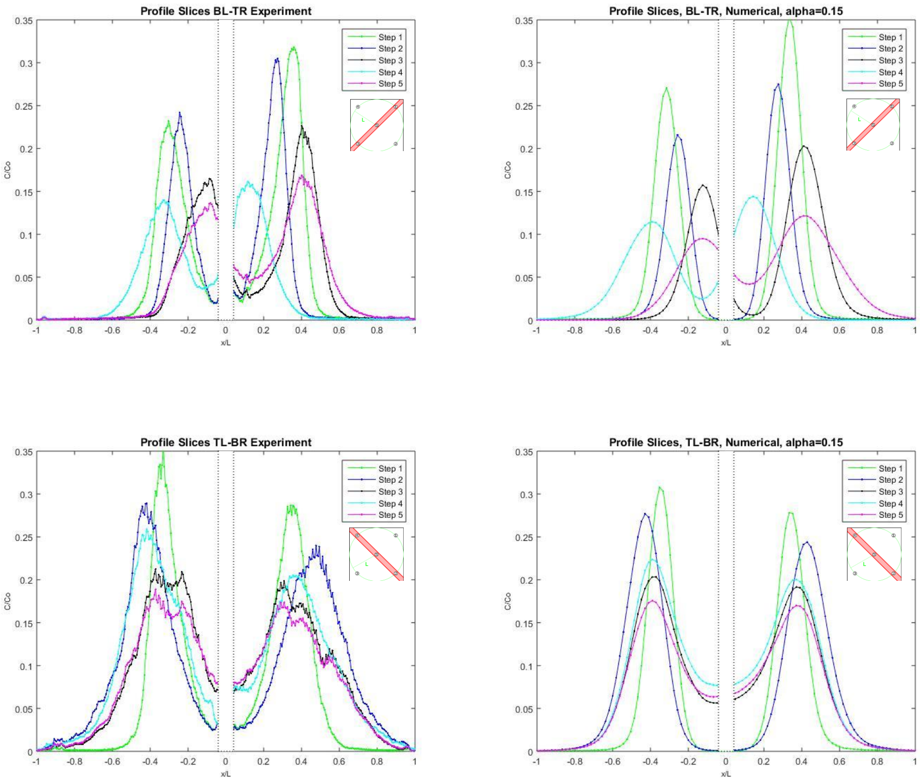

Figure 35: Combined profile slices for steps 1 through 5 for Oscillating EIE. Including experiment 2 and numerical results. Numerical data taken from Reising (2018)

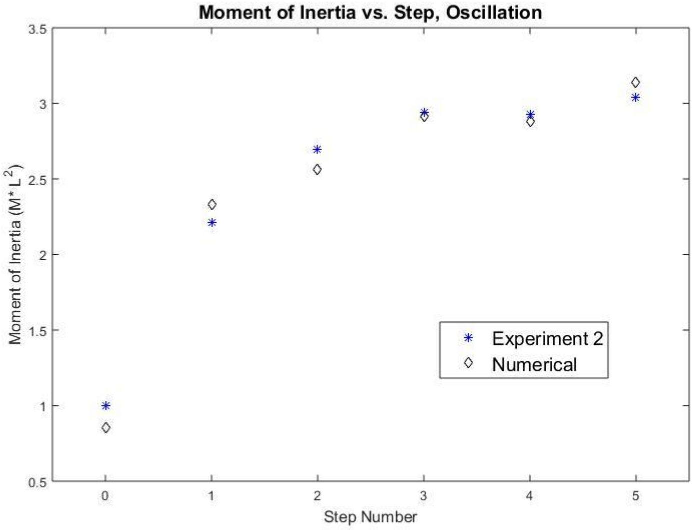

Figure 36: Moment of inertia by step for experiment 2 and numerical data, oscillation EIE.

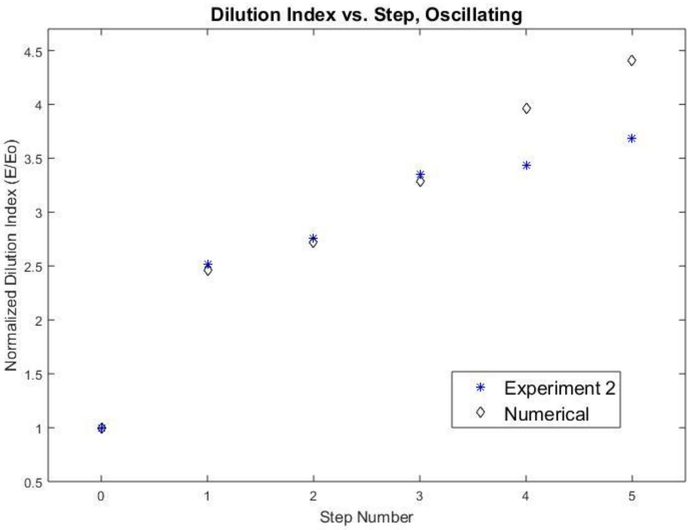

Figure 37: Dilution index by step for experiment 2 and numerical data, oscillation EIE. Normalized by the step 0 dilution index.

Qualitative analysis of plume dynamics (Fig. 33) indicates reasonable agreement for the shape and spread of the plume in the experimental and numerical models. The numerical models seem to faithfully convey the advective processes present in the experiment under this EIE regiment. Experiment 2 essentially conserved mass during the EIE sequence, with a 2.5% change in mass over the course of the experiment (App. 8.1).

Quantitative analysis indicates some difference between the scalar distribution in experiment 2 and the numerical simulation for steps 0 and 1 (Fig. 34). In spite of this, concentration profiles match relatively well for subsequent steps. The discrepancies are attributable to the presence of a physical well in the experiments, which contributes to the persistent scalar tails. Plots for combined profile slices (Fig. 35) illustrate some discrepancies in behavior between the numerical and experimental simulations. It would appear that dispersion in the model is too high as peak concentrations decay more rapidly, and scalar distributions spread more quickly for the numerical model. This is more pronounced in profile slices taken parallel to flow, indicating that the longitudinal dispersivity requires more adjustment than the transverse dispersion in the numerical model. Moments of inertia in the numerical data show some agreement with the experiment (Fig. 36), indicating that the numerical model nearly describes plume spread. Dilution index for the numerical and experimental data match worse as the sequence progresses (Fig. 37), indicating a departure in mixing behavior.

4.4 Folding Sequence

The folding sequence was designed to stretch and fold the scalar plume in an attempt to spread the plume with chaotic advection. This sequence follows the proposed EIE method presented in Mays & Neupauer, 2012, and is similar to the numerical sequence presented in Piscopo et al., 2013.

Step 1 is used to move the plume toward well 4, which sets up the first folding event in step 2. To create the fold in step 2, a stagnation point is created between wells 4 and 5 by injecting into well 5 while using wells 2 and 4 as a dipole. Step 3 is used to stretch the plume, followed by step 4 which was used to move the plume in anticipation of another folding event in step 5. Similar to step 2, step 5 makes use of a stagnation point to create the fold.

Folding Pumping Sequence:

Step 0: Wells 1 through 4 were left open to the atmosphere. 0.034 pore volumes of dye were injected into well 5 to create the plume, followed by an injection of 0.012 pore volumes of clear fluid to clear the well bore of dye.

Number of pore volumes injected per step:

	Well 1	Well 2	Well 3	Well 4	Well 5
Step 1	0	0.278	0	-0.277	0
Step 2	0	-0.554	0	0.444	0.111
Step 3	0.139	-0.028	0.139	-0.250	0
Step 4	0.277	0	-0.277	0	0
Step 5	-0.428	0	0.257	0	0.171

Table 3: Folding EIE Pumping Scheme

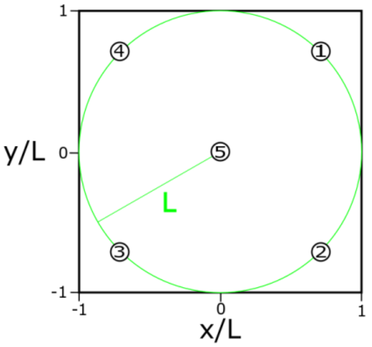

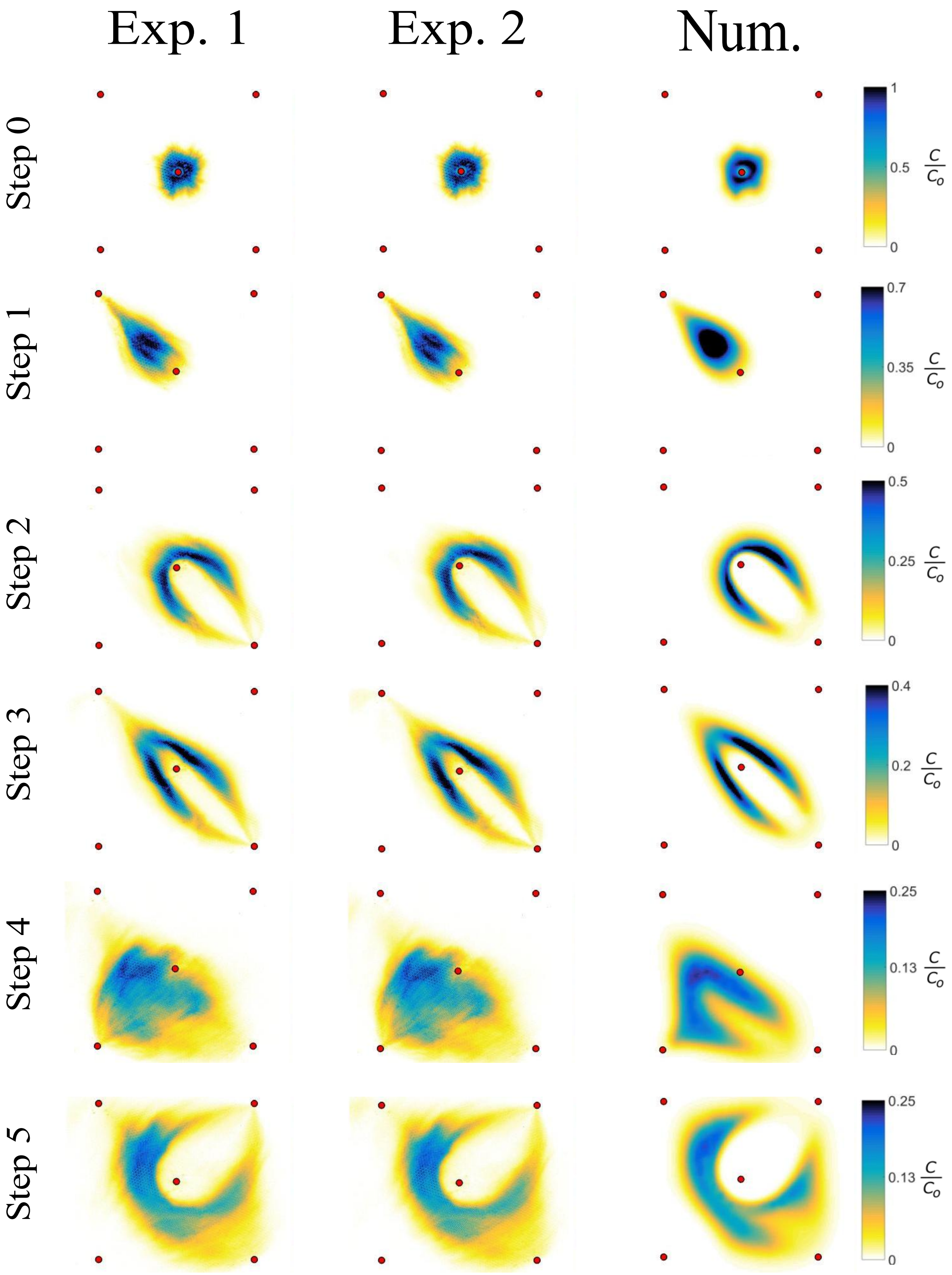

Figure 38: Experimental and numerical plume images of $\frac{c}{c_o}$ for Folding EIE. Numerical data taken from Reising (2018)

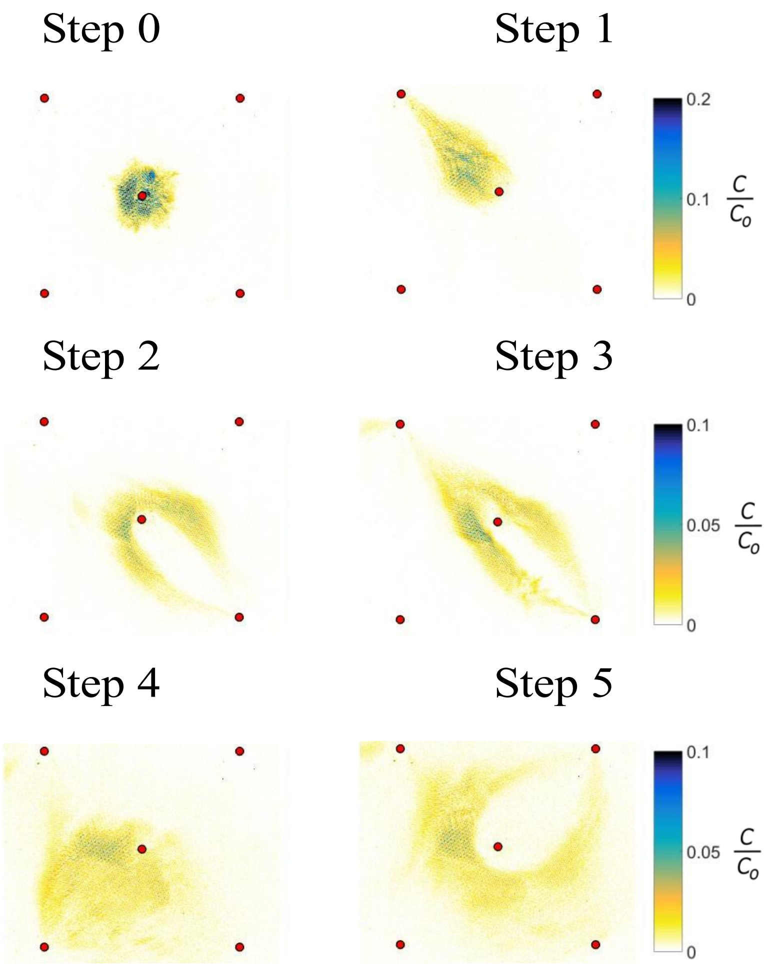

Figure 39: Differences in $\frac{C}{C_o}$ between experiment 1 and experiment 2 for Folding EIE.

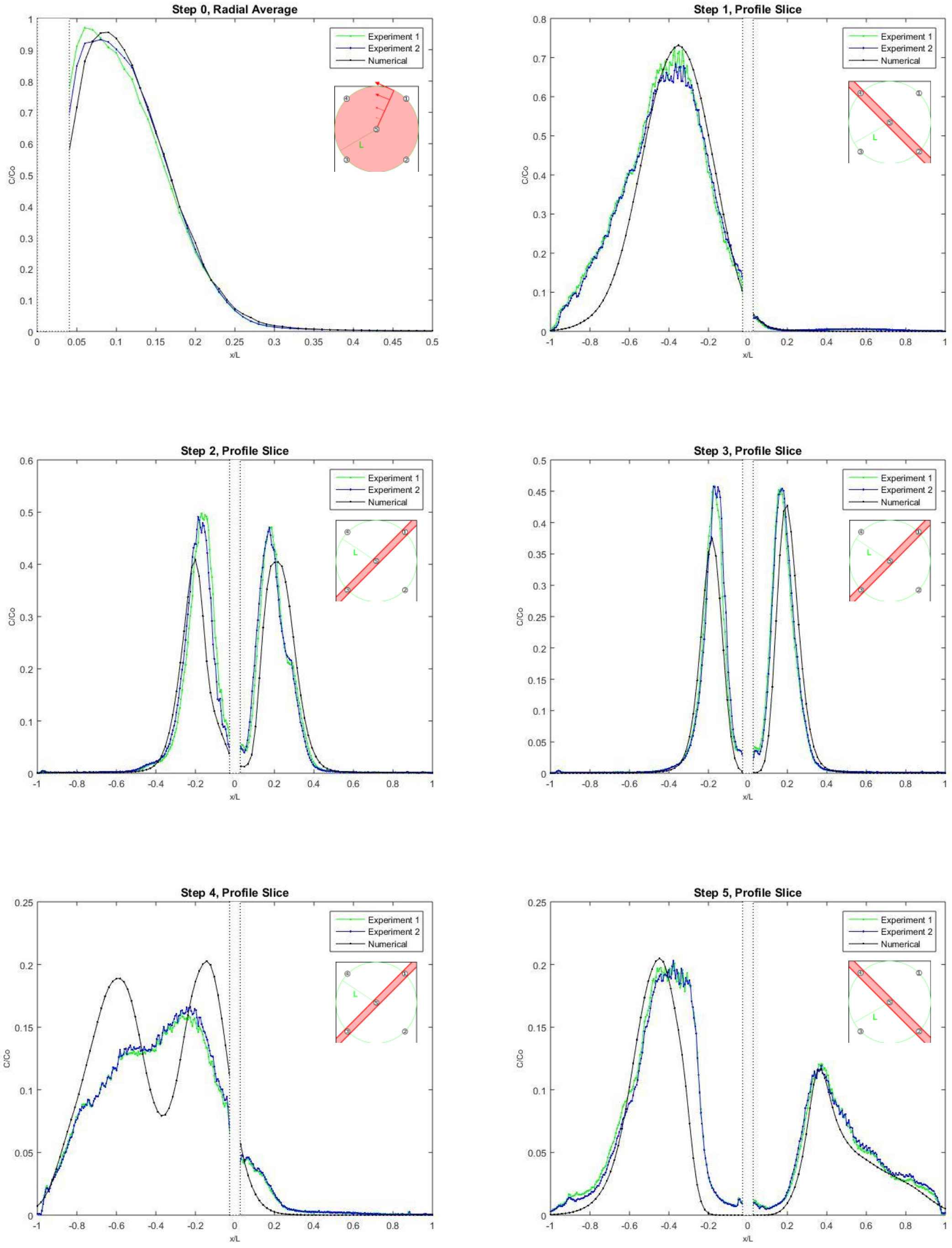
Step 0, Radial Average

Step 1, Profile Slice

Step 2, Profile Slice

Step 3, Profile Slice

Step 4, Profile Slice

Step 5, Profile Slice

Figure 40: Concentration profiles for Folding EIE. Includes first & second experiments with numerical results. Numerical data taken from Reising (2018)

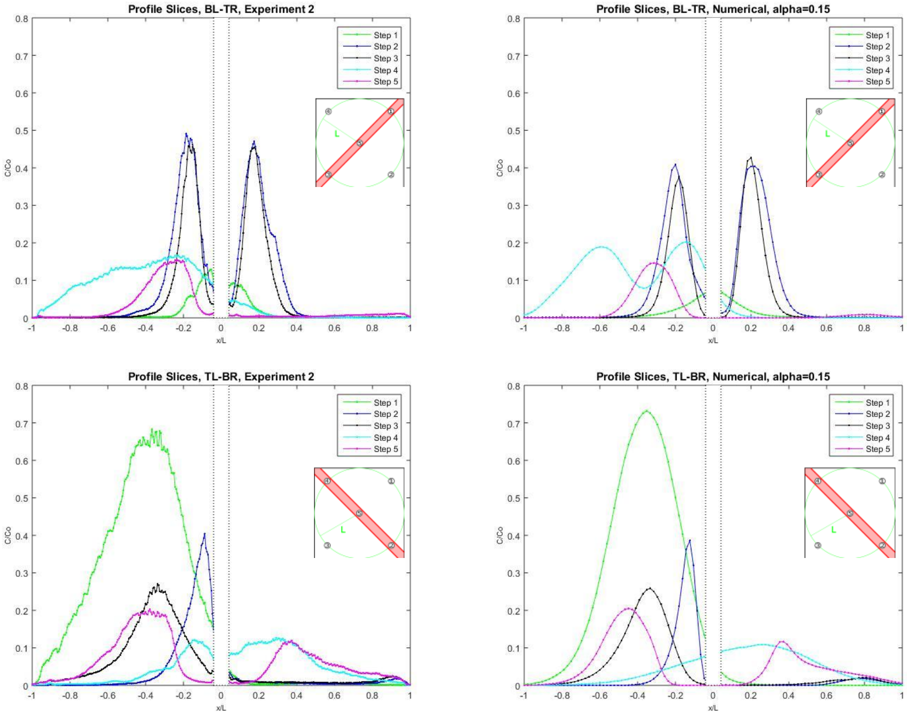

Figure 41: Combined profile slices for steps 1 through 5 of Folding EIE. Including experiment 2 and numerical results. Numerical data taken from Reising (2018)

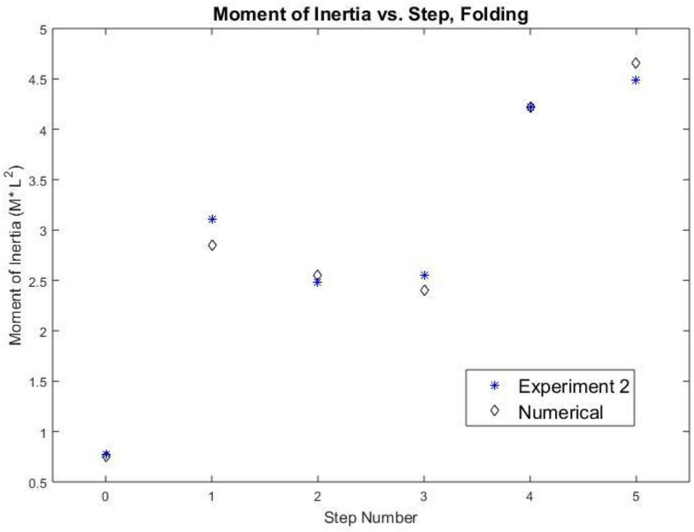

Figure 42: Moment of inertia by step for experiment 2 and numerical data, folding EIE.

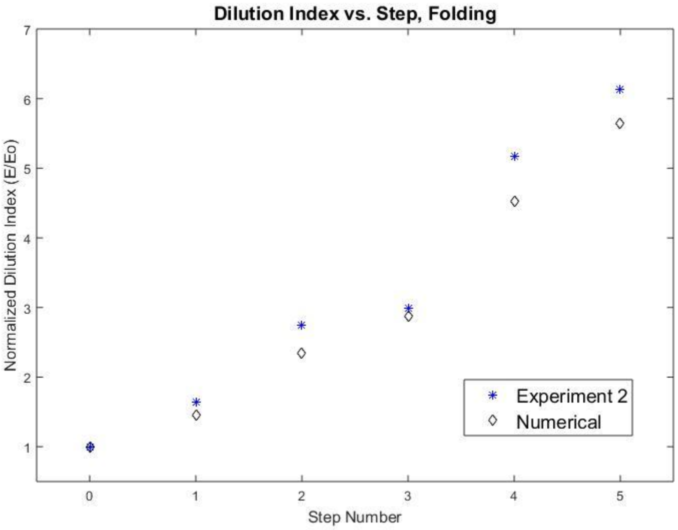

Figure 43: Dilution index by step for experiment 2 and numerical data, folding EIE. Normalized by the step 0 dilution index.

Qualitative analysis of plume images shows essentially identical results for the experimental and numerical models (Fig. 38). Plots of the absolute value of the difference in non-dimensional spatial concentrations in experiments 1 and 2, indicate a high degree of repeatability between experiments (Fig. 39). Experiments nearly conserve mass during the EIE sequences, with a 4.5% change in mass over the course of experiment 1 and a 3.02% change in mass over the course of experiment 2 (see appendix for step-wise mass values). The quantitative analysis shows excellent agreement for steps 0, 1, and 5 (Fig. 34). Steps 2 and 3 of the numerical model exhibit slightly lower peak concentrations, and step 4 shows more dispersion in the center of the plume during experiments. All of these discrepancies could be due to well 5, which is a physical high permeability zone in the experiment, but modeled as a point with homogenous permeability in the numerical model. However, these differences do not seem to have any ultimate effect for step 5, as the profiles show excellent agreement once again. The overall dispersive behaviors with time seem to match well for this EIE sequence (Fig. 41). Moments of inertia in the numerical data show good agreement with the experiment (Fig. 42), indicating that the numerical model describes plume spread. Dilution index for the numerical and experimental data matches better for this sequence than the others (Fig. 43). This may indicate that folding has a direct effect on mixing behavior.

4.5 Two-Scalar Folding

The reaction kinetics are well understood for well mixed systems. Within the context of reaction in porous media, achieving a well mixed condition is not well understood. This is the motivation for two-scalar experiments. In the quasi-two-dimensional apparatus, two scalars that overlap at a one-to-one ratio would be considered completely mixed, when considered in tandem with theoretical reaction kinetics, this would supply dependable reaction data. Though there is no actual reaction occurring in our experiments, mixing processes do occur, as such this experiment will model reaction kinetics for a system with a very low reaction rate.

The two-scalar folding EIE experiment uses an identical pumping sequence to the folding sequence in section 3.4. The initial condition is also essentially the same, but broken into two equal dye injections over two experiments, with a superimposed spatial distribution that matches the initial condition for the folding sequence in section 3.4. By matching many of the variables in the preceding experiment, the two-scalar folding experiment can be validated by comparison to the single-scalar experiments (App. 8.2). Data will be presented for scalar A, scalar B, and the reaction product.

Two-Scalar Folding Pumping Sequence:

Step 0: Wells 1 through 4 were left open to the atmosphere. For the outer plume, 0.017 pore volumes of dye were injected into well 5 to create the plume, followed by an injection of 0.029 pore volumes of clear fluid. In a separate experiment, the inner plume was created by injecting 0.017 pore volumes of dye, followed by 0.012 pore volumes of clear fluid.

Steps 1 through 7 are identical to the pumping sequence used for the folding sequence in section 3.4.

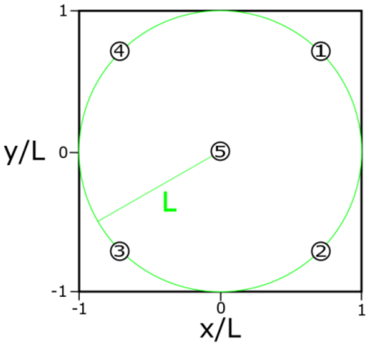

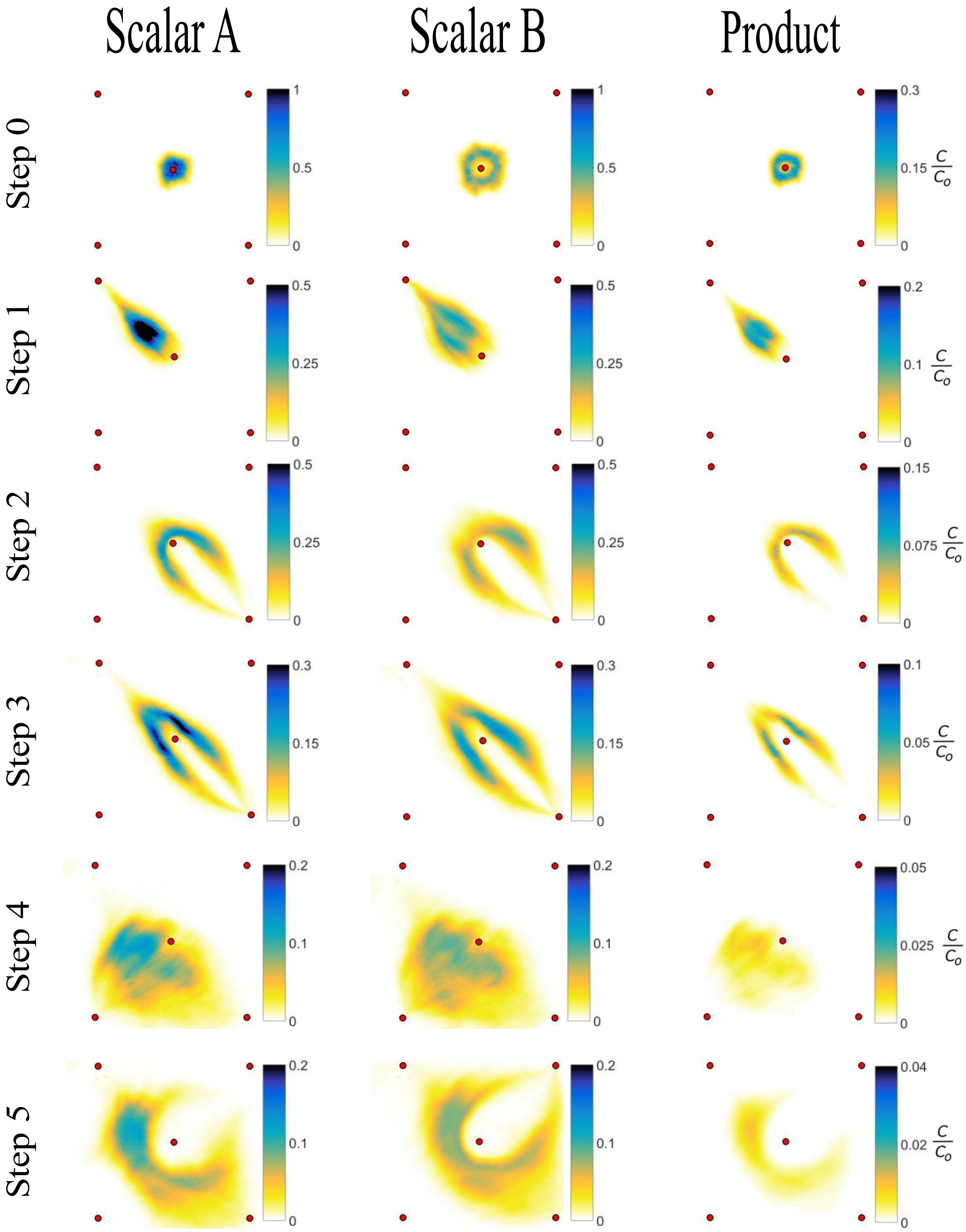

Figure 44: Experimental plume images of $\frac{C}{C_o}$ for scalar A, scalar B, and the reaction product. Folding EIE sequence is used to facilitate spreading.

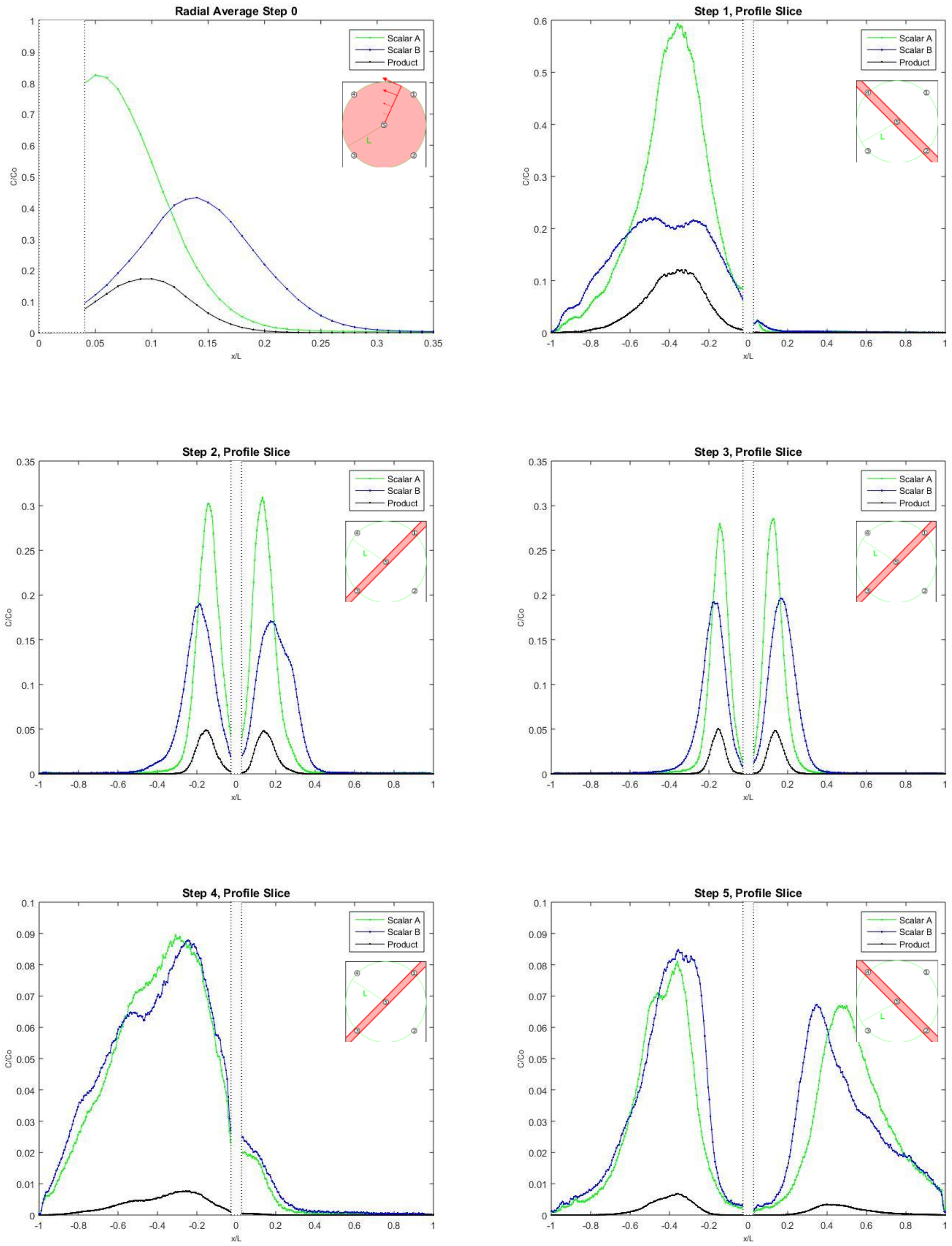

Figure 45: Concentration profiles for Two-Scalar Folding EIE. Includes inner plume (scalar A), outer plume (scalar B), and the product.

The two-scalar imaging technique was effective, as evident from similar scalar concentration distributions to those found in the single-scalar folding EIE sequence. Two-color, single-dye data was also similar to those found in an experiment that used two fluorescent dyes during a single experiment (App. 8.2). Qualitative results (Fig. 44) and quantitative results (Fig. 45) both indicate significant mixing and reaction upon initial injection of scalar B into the scalar A plume. The re-orientation of the plumes during step 1 also contributes to a high production of reactant. For subsequent steps, it appears that the scalars continue to get mixed, as concentration profiles become largely indistinguishable in later steps. Reactant formation is lower in the later steps, but this is a direct result of lower spatial concentrations of the scalars.

5. Discussion

These experiments were carried out with the expressed purpose of validating and improving numerical simulations of proposed EIE pumping protocols. Overall, numerical simulations captured many of the fundamental transport characteristics of the physical system. Qualitative and quantitative analysis indicates that advection is modeled well by the numerical model. However, there would seem to be more tuning necessary to capture dispersive phenomena. While dispersive spreading in experiments and numerics nearly match for many single steps within EIE regiments, they do not for others. Much of this could potentially be remedied by applying the porosity map to the numerical model. Spatial distribution of permeability in the experiment could be estimated with the porosity map. The resulting estimated permeability map could then be applied to the numerical model. By adding this critical information, it is possible that numerical dispersivities could then be calibrated such that dispersive processes more closely match those of the experiments. This should result in a less-smooth concentration distribution in numerical results, including the finer-scale lamellae present in plume images from the experiments. Conversely, by considering differences in plume behavior in the porosity-corrected and non-corrected numerical models, the degree of homogeneity attained in the experimental porous media beds could be evaluated with an additional metric.

Upon consideration of aggregate concentration profiles of all steps within an EIE sequence, spreading phenomena that could not be rectified by simplistic dispersivity tuning were apparent for many steps. At times, experimental longitudinal dispersion appeared to agree with the numerical model, while transverse did not. This would indicate the need to tune each component separately, rather than just assigning transverse dispersivity a value equal to one tenth of the longitudinal. As seen in data from the Push-Pull EIE protocol, it may be possible that there is a degree of reversibility present in the experiments that is not captured by the numerical model, evident from anomalies in aggregate behavior over the entirety of EIE sequences. An assertion of reversibility would require additional evidence, which could potentially be provided by further investigation of the results from the EIE experiments. At this point, it seems likely that the reversibility could be aided by incomplete mixing at the pore-scale. Some behaviors could also be explained by treating dispersion as a power function, making seepage velocity a more important variable. This is a more popular view than reversibility, as such, it may be a more likely to explain the discrepancies.

A potentially illuminating experimental data set has been created over the course of this research, with applicability to outside studies of scalar transport. With further analysis of the results, it is possible that some of the mysteries surrounding dispersion could be solved. At the very least, new questions could come to light, bringing with them a need for further experimental investigation. The EIE apparatus could easily be modified to accept a variety of porous media or source/sink configurations. In addition, the apparatus could be used to model mixing processes involving numerous scalars. The experimental apparatus proved itself over the course of this research, and now that its efficacy has been shown, it should be used for further investigation of fluid dynamics within porous media systems.

6. Conclusions

Methods and results for experiments investigating the spreading phenomena associated with engineered injection and extraction have been presented. Methods improved upon RIM and LIF techniques used in other studies; supporting EIE experiments that produced high-resolution data for a relatively large quasi-two-dimensional test section, within an apparatus designed to minimize the influence of apparatus walls. The products were first-of-their-kind data sets showing the evolution of spatial concentration distributions produced by a suite of candidate EIE pumping sequences, using a non-invasive imaging technique. EIE experimental procedures were validated by replicate experiments that exhibited a high degree of repeatability. In addition, experimental and numerical simulations exhibited good qualitative agreement. Data from these experiments can be used to investigate the physics of scalar dispersion, spreading, and mixing in porous media. Specifically, this data will be used to calibrate and improve the numerical models used to simulate EIE protocols.

In developing EIE experiments, methods for mitigating wall effects, packing porous media for increased homogeneity, creating porosity maps, and investigating non-reactive mixing of two scalar species were also developed. Novel wall-effect mitigation techniques were validated by LIF measurements using RIM porous media in a one-dimensional apparatus. Porous media packing techniques produced a higher degree of homogeneity for spherical, monodisperse media than any other study found over the course of this research. The highly-homogenous porous media field used in EIE experiments aids in understanding dispersion in the system. Similarly, LIF porosity mapping techniques, which were calibrated with physical porosity measurements, should prove valuable in the analysis of spreading phenomena in EIE experiments. The novel two-scalar imaging technique, validated by comparison to single-scalar

EIE experiments and by an experiment using two dyes, provided mixing data with enhanced temporal and spatial resolution as compared to methods found in similar studies. Experimental methods developed in this research could have applications to a number of fields beyond groundwater hydrology, including chemical engineering, bio-medical research, or oil recovery.

7. Works Cited

Amini, N., & Hassan, Y. A. (2012). An investigation of matched index of refraction technique and its application in optical measurements of fluid flow. *Experiments in Fluids*, *53*(6), 2011-2020. doi:10.1007/s00348-012-1398-x

Anderson, R. T., Vrionis, H. A., Ortiz-Bernad, I., Resch, C. T., Long, P. E., Dayvault, R., . . . Peacock, A. (2003). Stimulating the in situ activity of Geobacter species to remove uranium from the groundwater of a uranium-contaminated aquifer. *Applied and environmental microbiology, 69*(10), 5884-5891.

Aref, H., Blake, J. R., Budišić, M., Cardoso, S. S., Cartwright, J. H., Clercx, H. J., . . . Gouillart, E. (2017). Frontiers of chaotic advection. *Reviews of Modern Physics, 89*(2), 025007.

Atmakidis, T., & Kenig, E. Y. (2015). Numerical Analysis of Residence Time Distribution in Packed Bed Reactors with Irregular Particle Arrangements. *Chemical Product and Process Modeling, 10*(1), 17-26. doi:10.1515/cppm-2014-0021

Bagtzoglou, A. C., & Oates, P. M. (2007). Chaotic advection and enhanced groundwater remediation. *Journal of Materials in Civil Engineering, 19*(1), 75-83. doi:10.1061/(asce)0899-1561(2007)19:1(75)

Bear, J., & Bachmat, Y. (1967). *A generalized theory on hydrodynamic dispersion in porous media.* Paper presented at the IASH symposium on artificial recharge and management of aquifers.

Bhattacharjya, R. (2014). Groundwater Hydrology: National Programme on Technology Enhanced Learning (NPTEL) - Phase II.

Budwig, R. (1994). REFRACTIVE-INDEX MATCHING METHODS FOR LIQUID FLOW INVESTIGATIONS. *Experiments in Fluids, 17*(5), 350-355. doi:10.1007/bf01874416

Carman, P. C. (1937). Fluid flow through granular beds. *Trans. Inst. Chem. Eng., 15*, 150-166.

Castro-Alcala, E., Fernandez-Garcia, D., Carrera, J., & Bolster, D. (2012). Visualization of Mixing Processes in a Heterogeneous Sand Box Aquifer. *Environmental Science & Technology, 46*(6), 3228-3235. doi:10.1021/es201779p

Cenedese, A., & Viotti, P. (1996). Lagrangian Analysis of Nonreactive Pollutant Dispersion in Porous Media by Means of the Particle Image Velocimetry Technique. *Water Resources Research, 32*(8), 2329-2343. doi:10.1029/96WR00605

Chakravarthy, V. S., Ottino, J. M. (1995). Mixing studies using horseshoes. *Int. J. Bifurcat Chaos, 5*(2), 519-530.

Chen, C. S. (1987). Analytical solutions for radial dispersion with Cauchy boundary at injection well. *Water Resources Research, 23*(7), 1217-1224.

Chen, J.-D., & Wada, N. (1986). Visualization of immiscible displacement in a three-dimensional transparent porous medium. *Experiments in Fluids, 4*(6), 336-338. doi:10.1007/bf00266299

Cirpka, O. A. (2002). Choice of dispersion coefficients in reactive transport calculations on smoothed fields. *Journal of Contaminant Hydrology, 58*(3), 261-282. doi:https://doi.org/10.1016/S0169-7722(02)00039-6

Cirpka, O. A., de Barros, F. P. J., Chiogna, G., Rolle, M., & Nowak, W. (2011). Stochastic flux-related analysis of transverse mixing in two-dimensional heterogeneous porous media. *Water Resources Research, 47*. doi:10.1029/2010wr010279

Cohen, Y., & Metzner, A. B. (1981). Wall effects in laminar flow of fluids through packed beds. *AIChE Journal, 27*(5), 705-715. doi:doi:10.1002/aic.690270502

Crimaldi, J. P. (2008). Planar laser induced fluorescence in aqueous flows. *Experiments in Fluids, 44*(6), 851-863.

Dagan, G. (1989). Flow and Transport in Porous Formations. Berlin: Springer-Verlag.

Darcy, H. (1856). The public fountains of the city of Dijon. *Victor Dalmont, Paris, France*.

Dentz, M., Le Borgne, T., Englert, A., & Bijeljic, B. (2011). Mixing, spreading and reaction in heterogeneous media: A brief review. *Journal of Contaminant Hydrology, 120-21*, 1-17. doi:10.1016/j.jconhyd.2010.05.002

Dow-Corning. (2015). Properties of Pyrex, Pyrexplus, and Low Actinik Pyrex code 7740 Glasses.

Edery, Y., Dror, I., Scher, H., & Berkowitz, B. (2015). Anomalous reactive transport in porous media: Experiments and modeling. *Physical Review E, 91*(5), 052130.

Eisfeld, B., & Schnitzlein, K. (2001). The influence of confining walls on the pressure drop in packed beds. *Chemical Engineering Science, 56*(14), 4321-4329. doi:10.1016/s0009-2509(00)00533-9

Fand, R. M., Kim, B. Y. K., Lam, A. C. C., & Phan, R. T. (1987). Resistance to the flow of fluids through simple and complex porous-media whose matrices are composed of randomly packed spheres. *Journal of Fluids Engineering-Transactions of the Asme, 109*(3), 268-274.

Finnemore, E. J., & Franzini, J. B. (2002). *Fluid mechanics with engineering applications* (Vol. 10): McGraw-Hill New York.

Fitts, C. R. (2002). *Groundwater science*: Elsevier.

Fort, C., Fu, C. D., Weichselbaum, N. A., Bardet, P. M. (2015). Refractive index and solubility control of para-cymene solutions for index-matched fluid–structure interaction studies. *Experiments in Fluids, 56*.

Gelhar, L. W., Welty, C., & Rehfeldt, K. R. (1992). A critical review of data on field-scale dispersion in aquifers. *Water Resources Research, 28*(7), 1955-1974.

Generalic, E. (2018). Hexagonal close-packed structure. Retrieved from https://glossary.periodni.com

Gunn, D. J. (1987). AXIAL AND RADIAL DISPERSION IN FIXED-BEDS. *Chemical Engineering Science, 42*(2), 363-373. doi:10.1016/0009-2509(87)85066-2

Hassan, Y. A., Dominguez-Ontiveros, E.E. (2008). Flow visualization in a pebble bed reactor experiment using PIV and refractive index matching techniques. *Nuclear Engineering and Design, 238*, 3080-3085.

Iskander, M. (2010). *Modelling with Transparent Soils Visualizing Soil Structure Interaction and Multi Phase Flow, Non-Intrusively*. Berlin: Springer-Verlag.

Kapoor, V., & Gelhar, L. W. (1994). Transport in 3-dimensionaly heterogeneous aquifers: Dynamics of concentration fluctuations. *Water Resources Research, 30*(6), 1775-1788. doi:10.1029/94wr00076

Kitanidis, P. K. (1994). The concept of the dilution Index. *Water Resources Research, 30*(7), 2011-2026. doi:10.1029/94wr00762

Klenk, I. D., & Grathwohl, P. (2002). Transverse vertical dispersion in groundwater and the capillary fringe. *Journal of Contaminant Hydrology, 58*(1-2), 111-128. doi:10.1016/s0169-7722(02)00011-6

Kundzewicz, Z. W., & Döll, P. (2009). Will groundwater ease freshwater stress under climate change? *Hydrological Sciences Journal, 54*(4), 665-675. doi:10.1623/hysj.54.4.665

Kwok, W., Hayes, R., & Nasr-El-Din, H. (1995). Dispersion in consolidated sandstone with radial flow. *Transport in porous media, 19*(1), 37-66.

Le Borgne, T., Dentz, M., Bolster, D., Carrera, J., de Dreuzy, J.-R., & Davy, P. (2010). Non-Fickian mixing: Temporal evolution of the scalar dissipation rate in heterogeneous porous media. *Advances in Water Resources, 33*(12), 1468-1475. doi:10.1016/j.advwatres.2010.08.006

Lee, J., Rolle, M., & Kitanidis, P. K. (2018). Longitudinal dispersion coefficients for numerical modeling of groundwater solute transport in heterogeneous formations. *Journal of Contaminant Hydrology, 212*, 41-54. doi:https://doi.org/10.1016/j.jconhyd.2017.09.004

Mackay, D. M., & Cherry, J. A. (1989). Groundwater contamination: Pump-and-treat remediation. *Environmental Science & Technology, 23*(6), 630-636.

Manz, B., Gladden, L., & Warren, P. (1999). Flow and dispersion in porous media: Lattice-Boltzmann and NMR studies. *AIChE Journal, 45*(9), 1845-1854.

Mays, D. C., & Neupauer, R. M. (2012). Plume spreading in groundwater by stretching and folding. *Water Resources Research, 48*. doi:10.1029/2011wr011567

McWhirter, J. D., Crawford, M. E., & Klein, D. E. (1998). Magnetohydrodynamic flows in porous media II: Experimental results. *Fusion Technology, 34*(3), 187-197.

Miner, C. S., & Dalton, N. N. (1953). *Glycerol*: Reinhold Publishing Corporation.

Moroni, M., & Cushman, J. H. (2001). Three-dimensional particle tracking velocimetry studies of the transition from pore dispersion to Fickian Dispersion for homogeneous porous media. *Water Resources Research, 37*(4), 873-884. doi:10.1029/2000WR900364

Motif, A. (2018). Rhodamine 6G GSD Goat anti-Rabbit lgG.

Muhammad, M., & Massimo, R. (2017). Experimental investigation of the impact of compound-specific dispersion and electrostatic interactions on transient transport and solute breakthrough. *Water Resources Research, 53*(2), 1189-1209. doi:doi:10.1002/2016WR019727

Ogata, A., & Banks, R. B. (1961). *A solution of the differential equation of longitudinal dispersion in porous media* (2330-7102). Retrieved from

Ogawa, K., Matsuka, T., Hirai, S., & Okazaki, K. (2001). Three-dimensional velocity measurement of complex interstitial flows through water-saturated porous media by the tagging method in the MRI technique. *Measurement Science and technology, 12*(2), 172.

Ottino, J. M., Jana, S. C., & Chakravarthy, V. S. (1994). From Reynolds stretching and folding to mixing studies using horseshoe maps. *Physics of Fluids, 6*(2), 685-699. doi:10.1063/1.868308

Park, J. T., Mannheimer, R. J., Grimley, T. A., & Morrow, T. B. (1989). Pipe Flow Measurements of a Transparent Non-Newtonian Slurry. *Journal of Fluids Engineering, 111*(3), 331-336. doi:10.1115/1.3243648

Patil, & Liburdy, J. A. (2012). Optical measurement uncertainties due to refractive index mismatch for flow in porous media. *Experiments in Fluids, 53*, 1453-1468. doi:10.1007/s00348-012-1369-2

Patil, V., Finn, J., He, X., Ziazi, R., Apte, S. V., Liburdy, J. A., & Wood, B. (2014). *Experimental Versus Computational Methods in the Study of Flow in Porous Media.* Paper presented at the ASME 2014 4th Joint US-European Fluids Engineering Division Summer Meeting collocated with the ASME 2014 12th International Conference on Nanochannels, Microchannels, and Minichannels.

Piscopo, A. N., Neupauer, R. M., & Mays, D. C. (2013). Engineered injection and extraction to enhance reaction for improved in situ remediation. *Water Resources Research, 49*(6), 3618-3625. doi:10.1002/wrcr.20209

Reising, L. J. (2018). *Numerical Investigations of Active and Passive Spreading to Enhance Mixing and Reaction in Porous Media.* (PhD), University of Colorado.

Rice. (2013). Laboratory Modeling of Critical Hydraulic Conditions for the Initiation of Piping *Geo-Congress 2013*.

Robbins, G. A. (1989). Methods for determining transverse dispersion coefficients of porous media in laboratory column experiments. *Water Resources Research, 25*(6), 1249-1258. doi:doi:10.1029/WR025i006p01249

Rolle, M., Eberhardt, C., Chiogna, G., Cirpka, O. A., & Grathwohl, P. (2009). Enhancement of dilution and transverse reactive mixing in porous media: Experiments and model-based interpretation. *Journal of Contaminant Hydrology, 110*(3–4), 130-142. doi:http://dx.doi.org/10.1016/j.jconhyd.2009.10.003

Romanenko, K. V., & Balcom, B. J. (2011). Permeability mapping in porous media by magnetization prepared centric-scan SPRITE. *Experiments in Fluids, 50*(2), 301-312. doi:10.1007/s00348-010-0923-z

Roth, Gilbert, B., & Mays, D. C. (2015b). Colloid Deposit Morphology and Clogging in Porous Media: Fundamental Insights Through Investigation of Deposit Fractal Dimension. *Environmental Science & Technology, 49*(20), 12263-12270. doi:10.1021/acs.est.5b03212

Roth, Mont-Eton, M. E., Gilbert, B., Lei, T. C., & Mays, D. C. (2015a). Measurement of colloidal phenomena during flow through refractive index matched porous media. *Rev Sci Instrum, 86*(11), 113103. doi:10.1063/1.4935576

Scheidegger, A. E. (1961). General theory of dispersion in porous media. *Journal of Geophysical Research, 66*(10), 3273-3278. doi:10.1029/JZ066i010p03273

Schwartz, C. E., & Smith, J. M. (1953). FLOW DISTRIBUTION IN PACKED BEDS. *Industrial and Engineering Chemistry, 45*(6), 1209-1218. doi:10.1021/ie50522a025

Smith, W. O., Foote, P. D., & Busang, P. F. (1929). Packing of Homogeneous Spheres. *Physical Review, 34*(9), 1271-1274. doi:10.1103/PhysRev.34.1271

Soltys, M. A., & Crimaldi, J. P. (2011). Scalar interactions between parallel jets measured using a two-channel PLIF technique. *Experiments in Fluids, 50*(6), 1625-1632. doi:10.1007/s00348-010-1019-5

Sposito, G. (2006). Chaotic solute advection by unsteady groundwater flow. *Water Resources Research, 42*(6). doi:10.1029/2005wr004518

Stohr, M., Roth, K., Jahne, B. (2003). Measurement of 3D pore-scale flow in index-matched porous media. *Experiments in Fluids, 35*, 159-166. doi:10.1007/s00348-003-0641-x

Stremler, M. A., Haselton, F. R., & Aref, H. (2004). Designing for chaos: applications of chaotic advection at the microscale. *Philosophical Transactions of the Royal Society a-Mathematical Physical and Engineering Sciences, 362*(1818), 1019-1036. doi:10.1098/rsta.2003.1360

Trefry, M. G., Lester, D. R., Metcalfe, G., Ord, A., & Regenauer-Lieb, K. (2012). Toward enhanced subsurface intervention methods using chaotic advection. *Journal of Contaminant Hydrology, 127*(1-4), 15-29. doi:10.1016/j.jconhyd.2011.04.006

Vafai, K. (2015). *Handbook of porous media*: Crc Press.

Werth, C. J., Zhang, C., Brusseau, M. L., Oostrom, M., & Baumann, T. (2010). A review of non-invasive imaging methods and applications in contaminant hydrogeology research. *Journal of Contaminant Hydrology, 113*(1-4), 1-24. doi:10.1016/j.jconhyd.2010.01.001

Wiederseiner, S., Andreini, N., Epely-Chauvin, G., Ancey, C. (2010). Refractive-index and density matching in concentrated particle suspensions: a review. *Experiments in Fluids, 50*, 1183-1206. doi: 10.1007/s00348-010-0996-8

Wildenschild, D., & Sheppard, A. P. (2013). X-ray imaging and analysis techniques for quantifying pore-scale structure and processes in subsurface porous medium systems. *Advances in Water Resources, 51*, 217-246. doi:https://doi.org/10.1016/j.advwatres.2012.07.018

Wright, S. F., Zadrazil, I., & Markides, C. N. (2017). A review of solid–fluid selection options for optical-based measurements in single-phase liquid, two-phase liquid–liquid and multiphase solid–liquid flows. *Experiments in Fluids, 58*(9), 108. doi:10.1007/s00348-017-2386-y

Zhang, P., DeVries, S. L., Dathe, A., & Bagtzoglou, A. C. (2009). Enhanced Mixing and Plume Containment in Porous Media under Time-Dependent Oscillatory Flow. *Environmental Science & Technology, 43*(16), 6283-6288. doi:10.1021/es900854r

Zhao, Y., Song, Y., Liu, Y., Liang, H., & Dou, B. (2011). Visualization and measurement of CO2 flooding in porous media using MRI. *Industrial & Engineering Chemistry Research, 50*(8), 4707-4715.

Zhu, W., Knapp, Y., & Deplano, V. (2016). Low hazard refractive index and density-matched fluid for quantitative imaging of concentrated suspensions of particles. *Experiments in Fluids*, *57*(5), 1-8. doi:10.1007/s00348-016-2150-8

8. Appendix

8.1 Additional EIE Data

Non-dimensional mass totals (M^*)

Push-Pull EIE

	Experiment 1	Experiment 2	Numerical
Step 0 (Step1,frame 23)	15.77	15.68	16.25
Step 1	16.25	16.25	16.25
Step2	15.73	15.66	16.25
Step3	16.18	16.03	16.25
Step 4	15.91	15.79	16.25

Oscillating EIE (not true replicate)

	Experiment 1	Experiment 2	Numerical
Step 0 (Step1,frame 23)	13.67	15.85	16.25
Step 1	12.83	16.04	16.25
Step2	13.00	16.25	16.25
Step3	12.77	16.25	16.25
Step 4	12.71	16.00	16.25
Step 5	12.93	16.15	16.25

One-Scalar Folding EIE

	Experiment 1	Experiment 2	Numerical
Step 0	15.52	15.82	16.25
Step 1	15.63	15.76	16.25
Step2	16.22	16.20	16.25
Step3	16.25	16.25	16.25
Step 4	16.11	16.00	16.25
Step 5	16.17	16.05	16.25

Two-Scalar Folding EIE

	Scalar A	Scalar B	Rxn. Product
Step 0	6.787	8.416	1.667
Step 1	8.066	8.082	1.487
Step2	8.125	8.125	0.8782
Step3	8.176	8.086	0.8188
Step 4	8.013	7.992	0.4437
Step 5	8.052	7.937	0.3267

EIE profiles with different dispersivities.

Push-Pull:

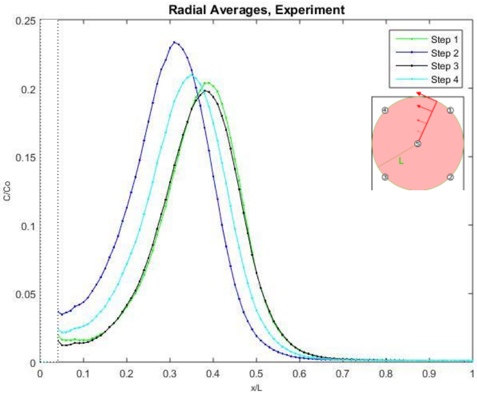
Radial Averages, Experiment

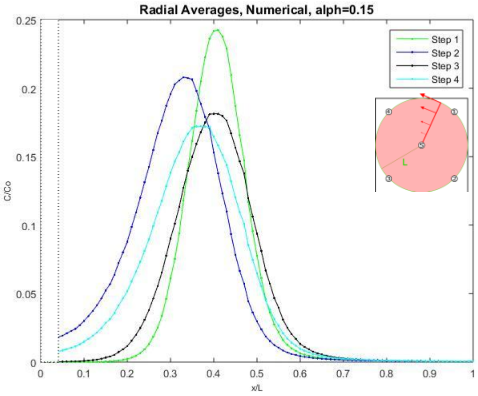
Radial Averages, Numerical, alph=0.15

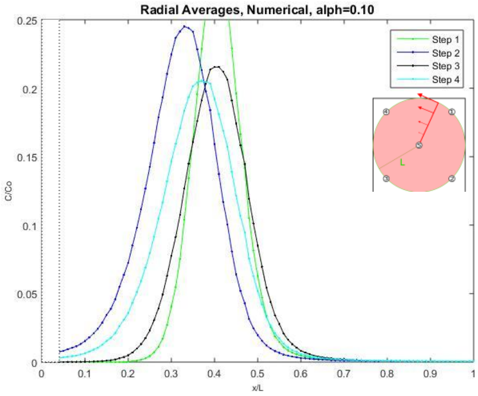
Radial Averages, Numerical, alph=0.10

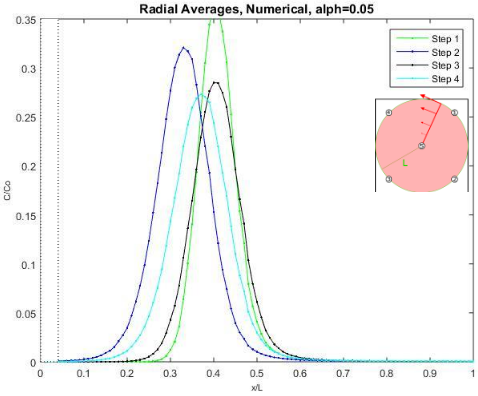
Radial Averages, Numerical, alph=0.05

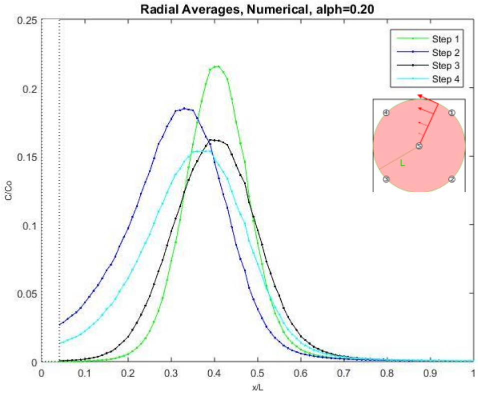
Radial Averages, Numerical, alph=0.20

Oscillating:

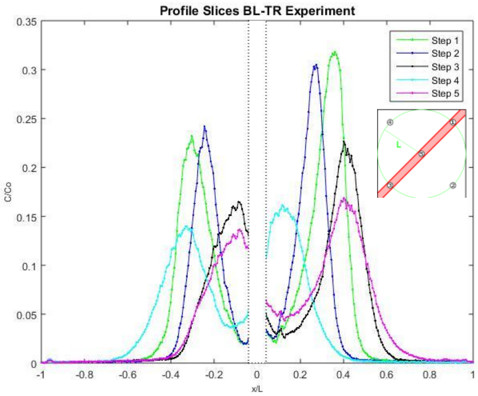

Profile Slices BL-TR Experiment

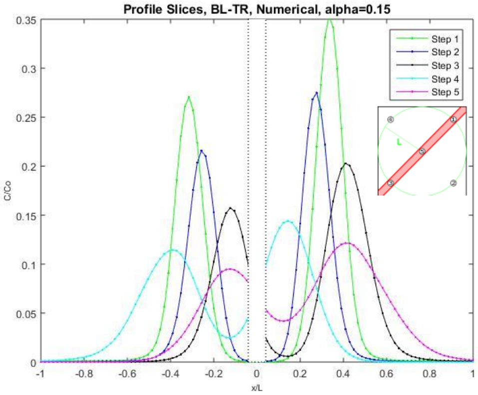

Profile Slices, BL-TR, Numerical, alpha=0.15

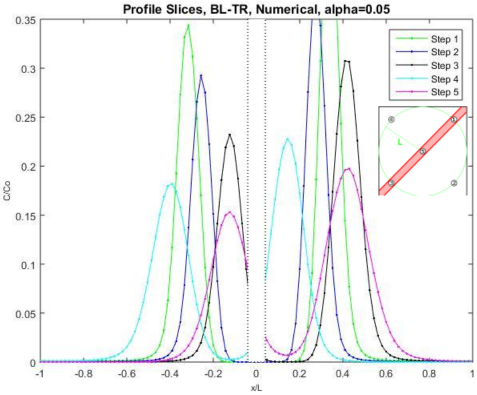

Profile Slices, BL-TR, Numerical, alpha=0.05

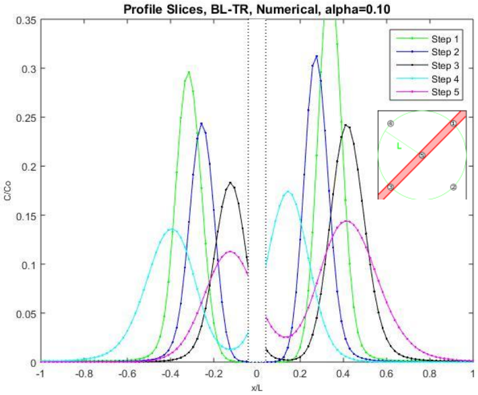

Profile Slices, BL-TR, Numerical, alpha=0.10

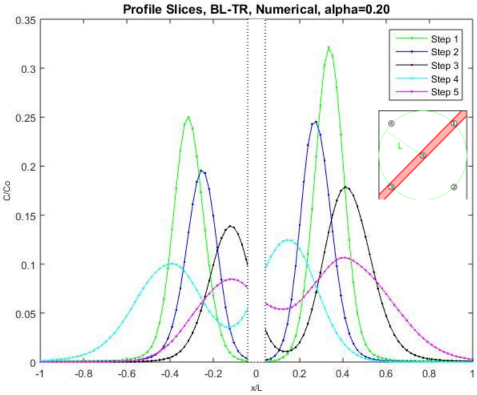

Profile Slices, BL-TR, Numerical, alpha=0.20

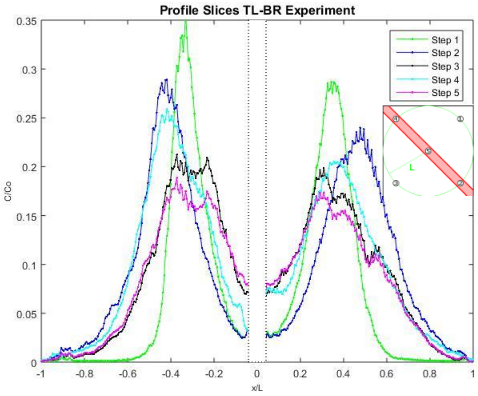
Profile Slices TL-BR Experiment

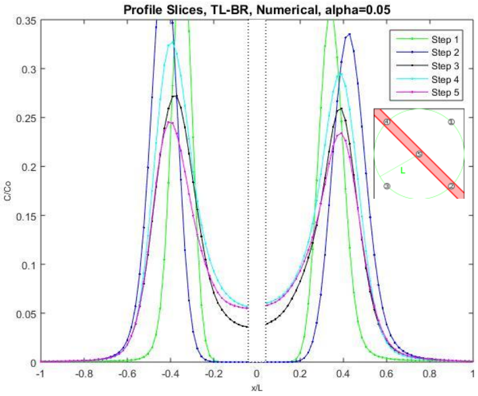
Profile Slices, TL-BR, Numerical, alpha=0.05

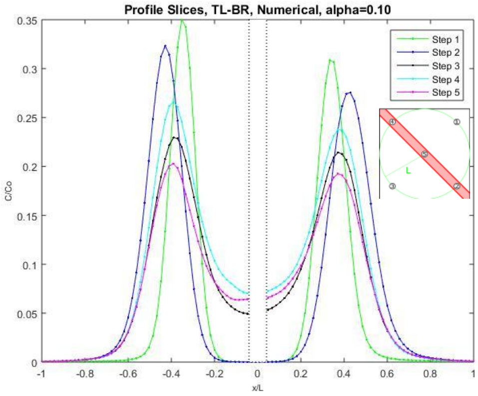
Profile Slices, TL-BR, Numerical, alpha=0.10

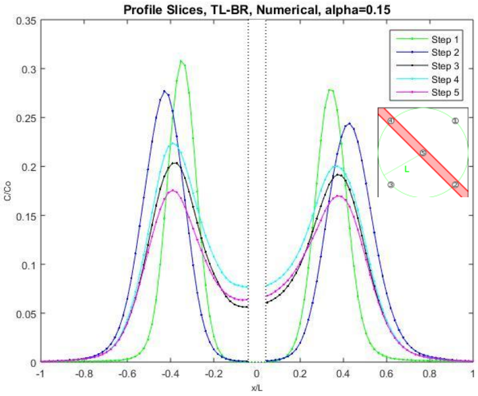
Profile Slices, TL-BR, Numerical, alpha=0.15

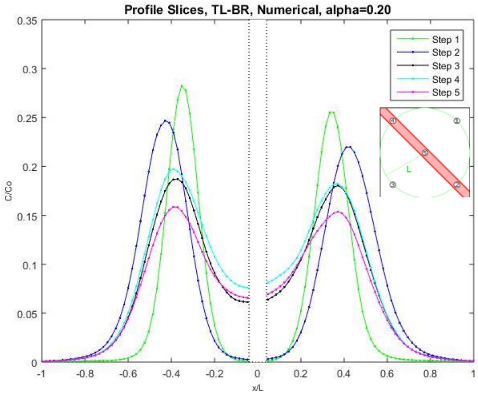
Profile Slices, TL-BR, Numerical, alpha=0.20

Folding:

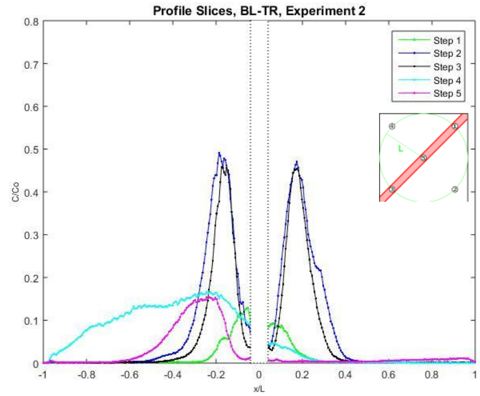
Profile Slices, BL-TR, Experiment 2
C/Co
x/L
0
0.1
0.2
0.3
0.4
0.5
0.6
0.7
0.8
-1
-0.8
-0.6
-0.4
-0.2
0
0.2
0.4
0.6
0.8
1
Step 1
Step 2
Step 3
Step 4
Step 5
L

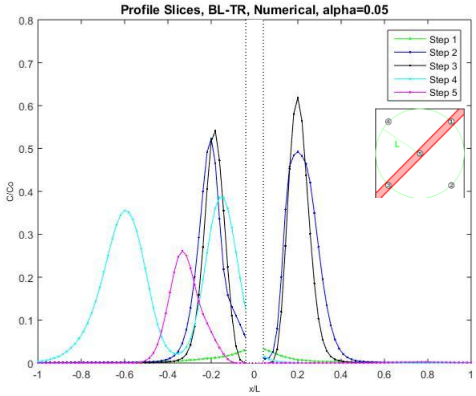
Profile Slices, BL-TR, Numerical, alpha=0.05
C/Co
x/L
0
0.1
0.2
0.3
0.4
0.5
0.6
0.7
0.8
-1
-0.8
-0.6
-0.4
-0.2
0
0.2
0.4
0.6
0.8
1
Step 1
Step 2
Step 3
Step 4
Step 5
L

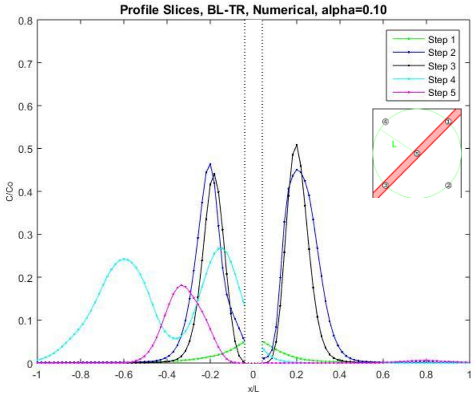
Profile Slices, BL-TR, Numerical, alpha=0.10
C/Co
x/L
0
0.1
0.2
0.3
0.4
0.5
0.6
0.7
0.8
-1
-0.8
-0.6
-0.4
-0.2
0
0.2
0.4
0.6
0.8
1
Step 1
Step 2
Step 3
Step 4
Step 5
L

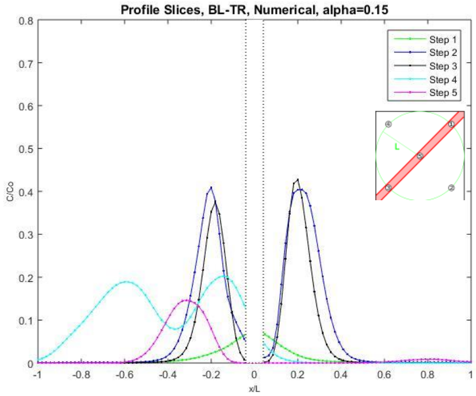
Profile Slices, BL-TR, Numerical, alpha=0.15
C/Co
x/L
0
0.1
0.2
0.3
0.4
0.5
0.6
0.7
0.8
-1
-0.8
-0.6
-0.4
-0.2
0
0.2
0.4
0.6
0.8
1
Step 1
Step 2
Step 3
Step 4
Step 5
L

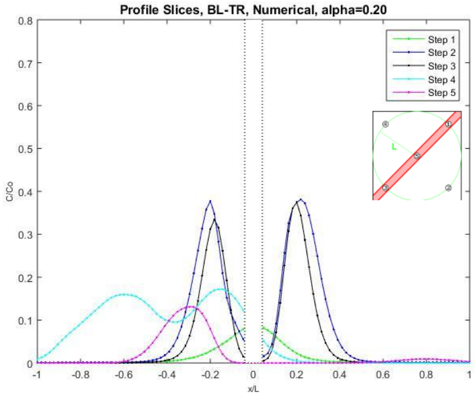
Profile Slices, BL-TR, Numerical, alpha=0.20
C/Co
x/L
0
0.1
0.2
0.3
0.4
0.5
0.6
0.7
0.8
-1
-0.8
-0.6
-0.4
-0.2
0
0.2
0.4
0.6
0.8
1
Step 1
Step 2
Step 3
Step 4
Step 5
L

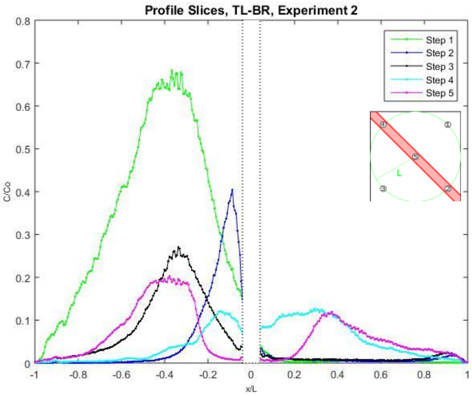
Profile Slices, TL-BR, Experiment 2
Step 1
Step 2
Step 3
Step 4
Step 5
C/Co
x/L
L
①
②
③
④
⑤

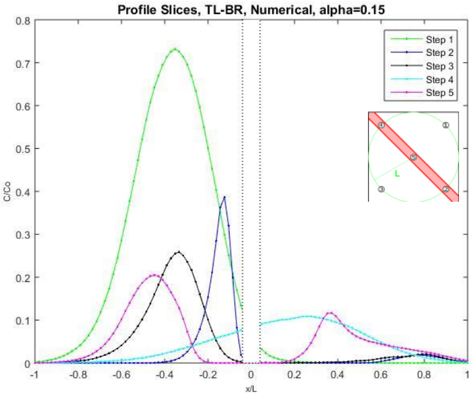
Profile Slices, TL-BR, Numerical, alpha=0.15
Step 1
Step 2
Step 3
Step 4
Step 5
C/Co
x/L
L

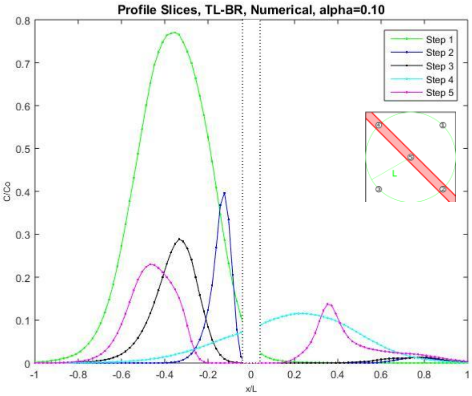
Profile Slices, TL-BR, Numerical, alpha=0.10
Step 1
Step 2
Step 3
Step 4
Step 5
C/Co
x/L
L

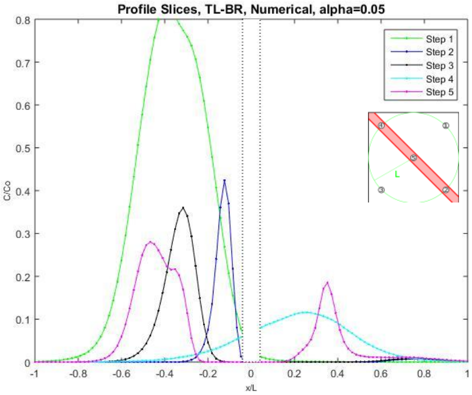
Profile Slices, TL-BR, Numerical, alpha=0.05
Step 1
Step 2
Step 3
Step 4
Step 5
C/Co
x/L
L

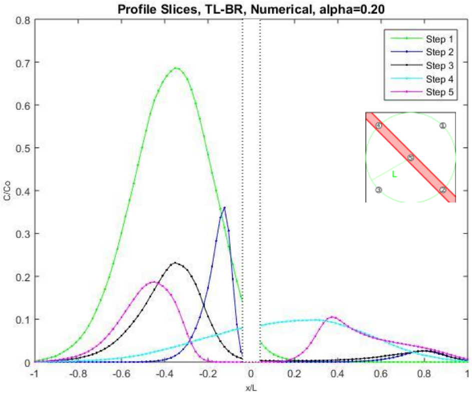
Profile Slices, TL-BR, Numerical, alpha=0.20
Step 1
Step 2
Step 3
Step 4
Step 5
C/Co
x/L
L

Oscillating EIE Plume Images:

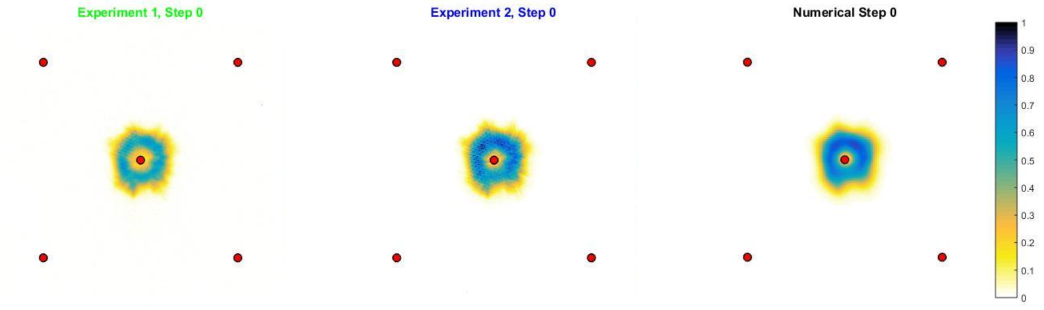

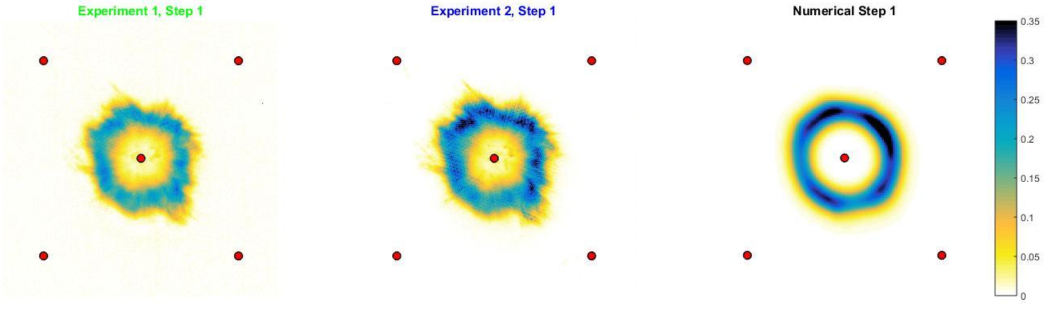

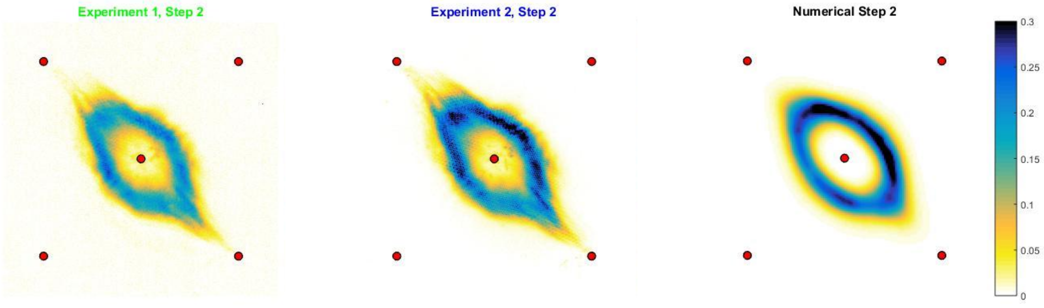

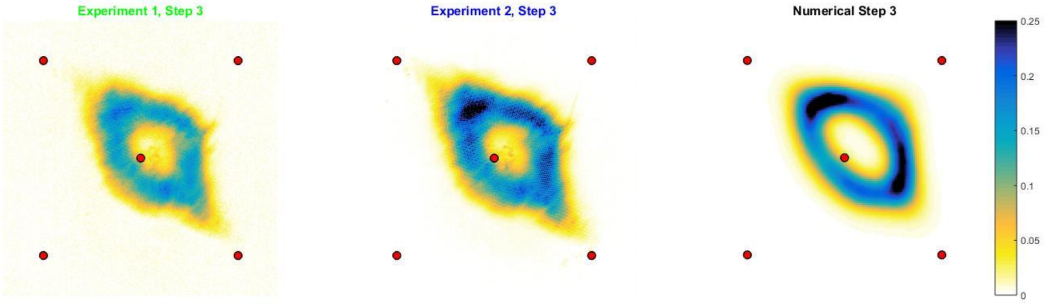

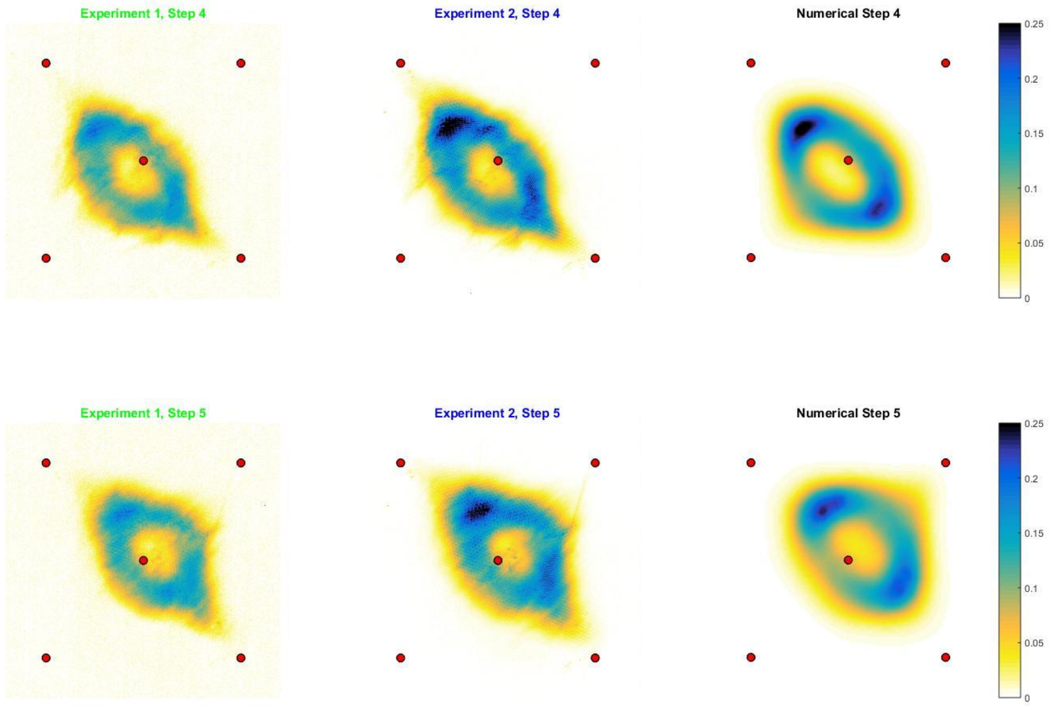
Experiment 1, Step 4
Experiment 2, Step 4
Numerical Step 4
0.25
0.2
0.15
0.1
0.05
0
Experiment 1, Step 5
Experiment 2, Step 5
Numerical Step 5
0.25
0.2
0.15
0.1
0.05
0

Oscillating EIE Quantitative Analysis:

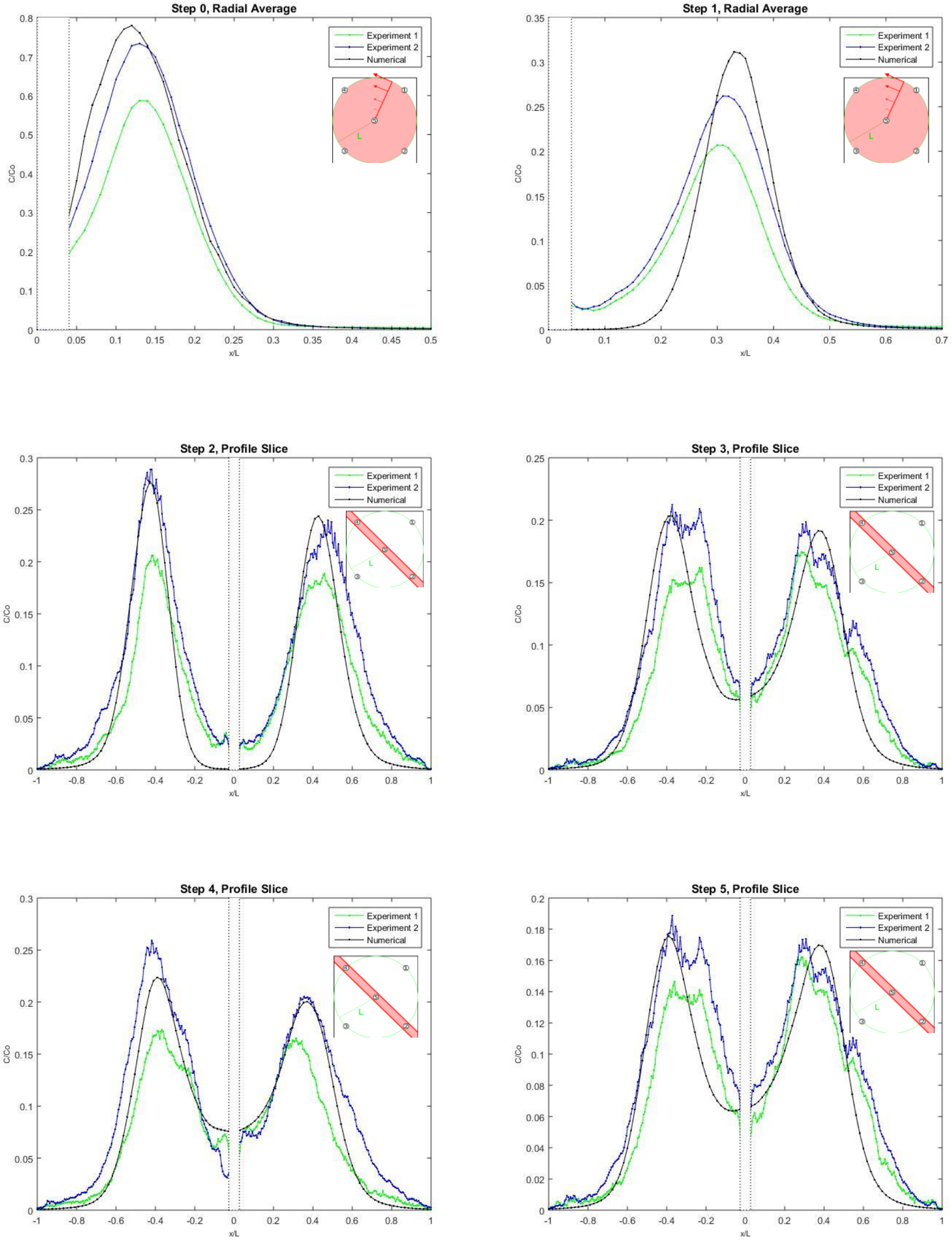

Concentration profiles for Oscillating EIE. Includes first & second experiments with numerical results.

8.2 Validation of Two-Scalar EIE

Plume dynamic matching for one-scalar folding and superimposed scalar images from two-scalar folding:

Experimental Sequence 4/26/18: Mass

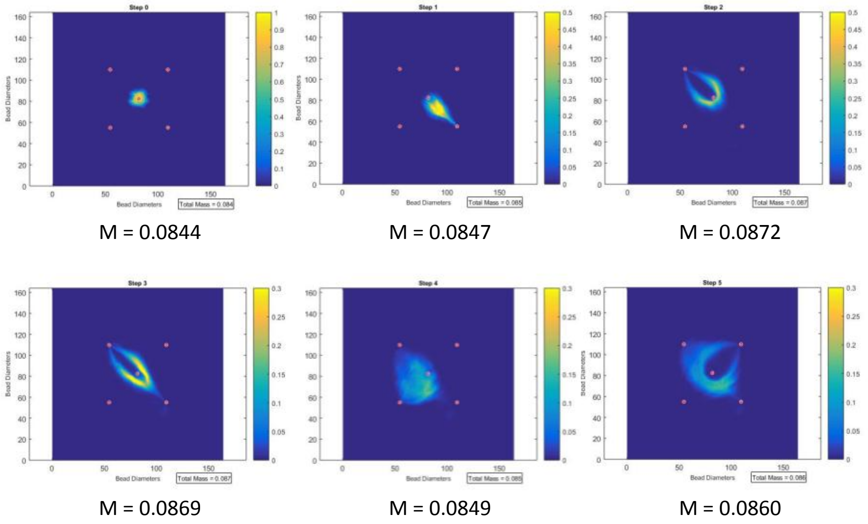

M = 0.0844 M = 0.0847 M = 0.0872

M = 0.0869 M = 0.0849 M = 0.0860

Experimental Sequence 2C: Combined Mass, Inner and Outer Plumes
(Combined Inner and Outer Images)

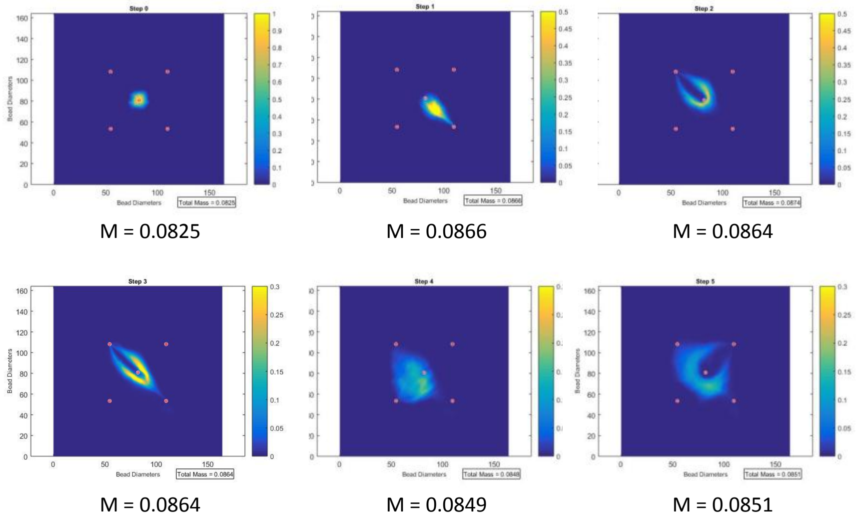

M = 0.0825 M = 0.0866 M = 0.0864

M = 0.0864 M = 0.0849 M = 0.0851

Comparison of Two-Scalar EIE technique to experiment with two different fluorescent dyes:

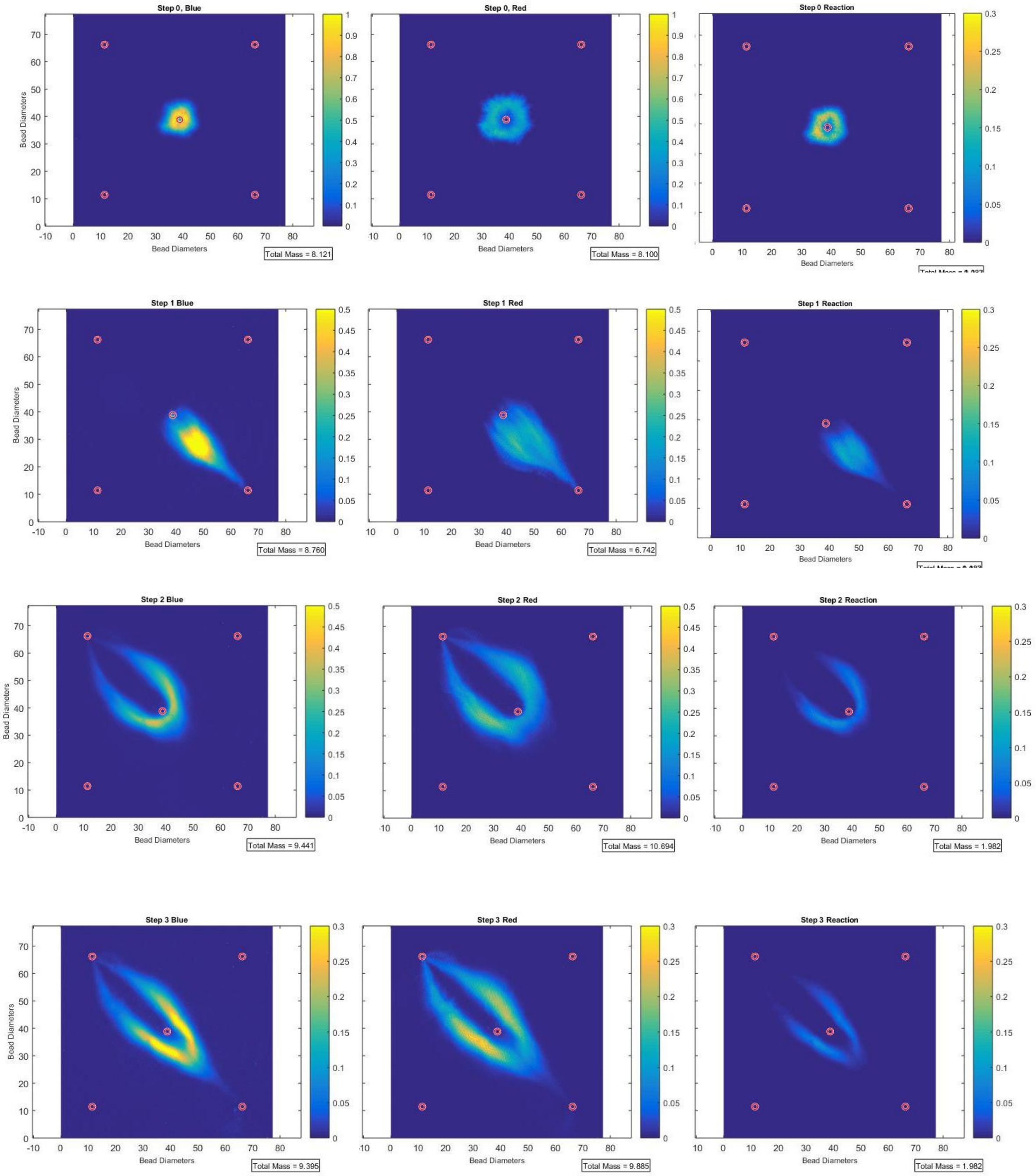
Step 0, Blue
Step 0, Red
Step 0 Reaction
Step 1 Blue
Step 1 Red
Step 1 Reaction
Step 2 Blue
Step 2 Red
Step 2 Reaction
Step 3 Blue
Step 3 Red
Step 3 Reaction
Bead Diameters
Total Mass = 8.121
Total Mass = 8.100
Total Mass = 8.760
Total Mass = 6.742
Total Mass = 9.441
Total Mass = 10.694
Total Mass = 1.982
Total Mass = 9.395
Total Mass = 9.885
Total Mass = 1.982

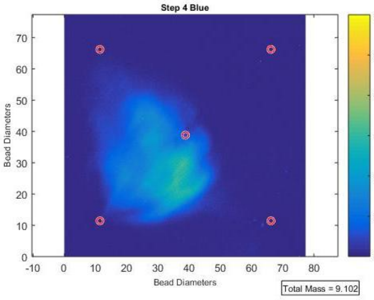
Step 4 Blue
Bead Diameters
Bead Diameters
Total Mass = 9.102

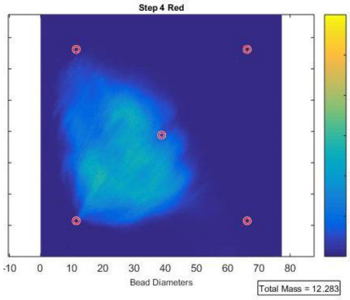
Step 4 Red
Bead Diameters
Total Mass = 12.283

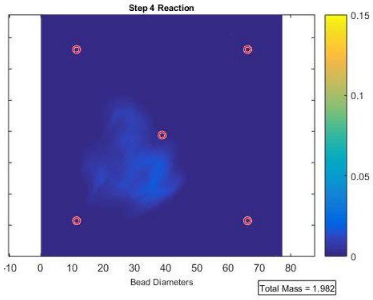
Step 4 Reaction
Bead Diameters
Total Mass = 1.982

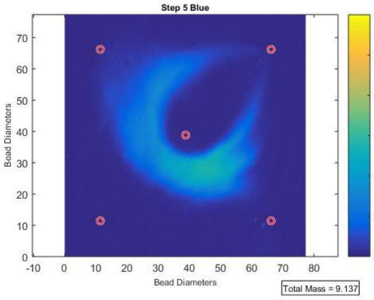
Step 5 Blue
Bead Diameters
Bead Diameters
Total Mass = 9.137

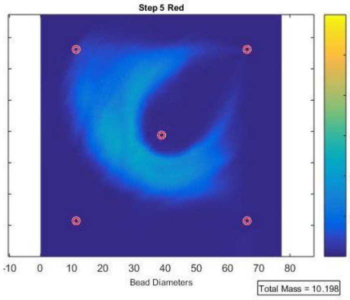
Step 5 Red
Bead Diameters
Total Mass = 10.198

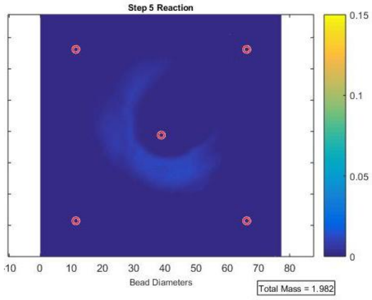
Step 5 Reaction
Bead Diameters
Total Mass = 1.982

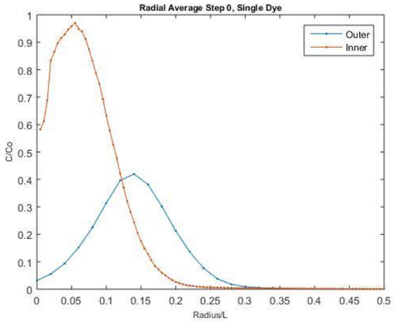
Radial Average Step 0, Single Dye
C/Co
Radius/L
Outer
Inner

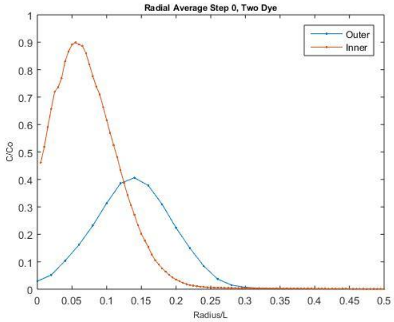
Radial Average Step 0, Two Dye
C/Co
Radius/L
Outer
Inner

8.3 Methods Overflow

RIM

Refractive index is typically measured using an Abbe refractometer, in which the sample is flanked by an illumination prism and a refracting prism. This treatment of the sample works well for liquids, but is not appropriate for measuring the refractive index of non-planar solids. Due to the geometry of the spherical porous media grains used in the EIE experiments, refractive index matching of the EIE media and fluid required a different approach. Rather than measuring refractive index of the media grains and fluid separately, an RIM test bench was designed to measure the degree of refractive index matching of the media and fluid as a system.

RIM candidate pairs were combined within a 40 mm x 40 mm x 40 mm, fused glass cuvette (Science Direct, part# C-G-F-40) at an equilibrated temperature, and then placed on the RIM test bench. A 514 nm beam from an argon-ion laser (Coherent Innova 90C-6) was expanded to a diameter of 1 cm through a beam expander (Melles Griot 25x-10x Beam Expander), turned into a sheet using a plano-convex cylindrical lens, then passed through the RIM sample. Downstream of the RIM sample, transmitted light was projected onto a sheet of white grid paper. A scientific camera (Imperx Bobcat, part# ICL-B1410M-SCO), fitted with a 25mm lens (Fujinon, part# HF25SA1) captured images of the projection onto the paper from the side opposite the sample. Refer to Figure A1 for a schematic of the RIM test bench.

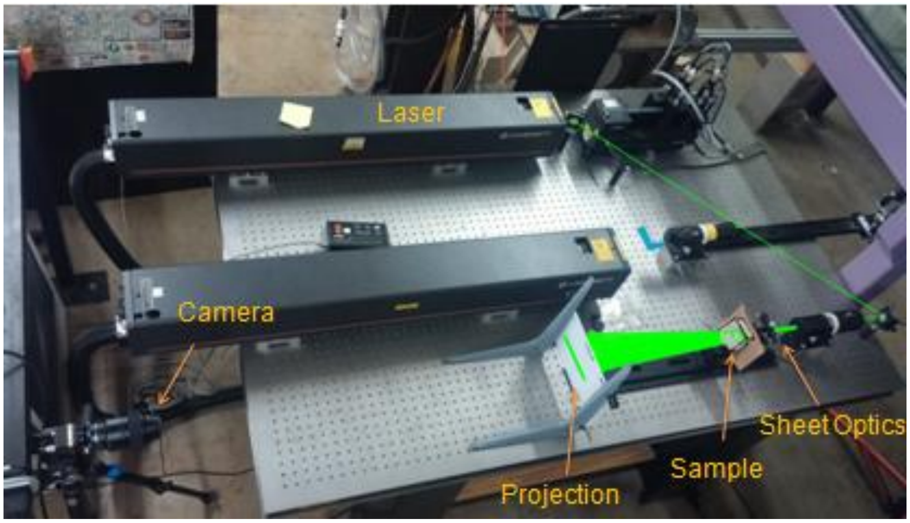

Figure A1: RIM test bench layout.

Due to lensing effects of the multiple porous media grains, an imperfect refractive index match of the media and fluid will cause light scattering as light is transmitted through the sample. This principal guides the interpretation of sample projections from the RIM test bench. A more precise index match will exhibit a tighter structure in the projection. More dramatic refractive index mismatches exhibit a more diffuse structure in the projection. This can be seen in Figure A2, where the respective refractive indices of Pyrex beads and DMSO solution were changed by the addition of water. It is apparent that the addition of 0.04 mL makes the refractive index match worse than that present at the optimal concentration.

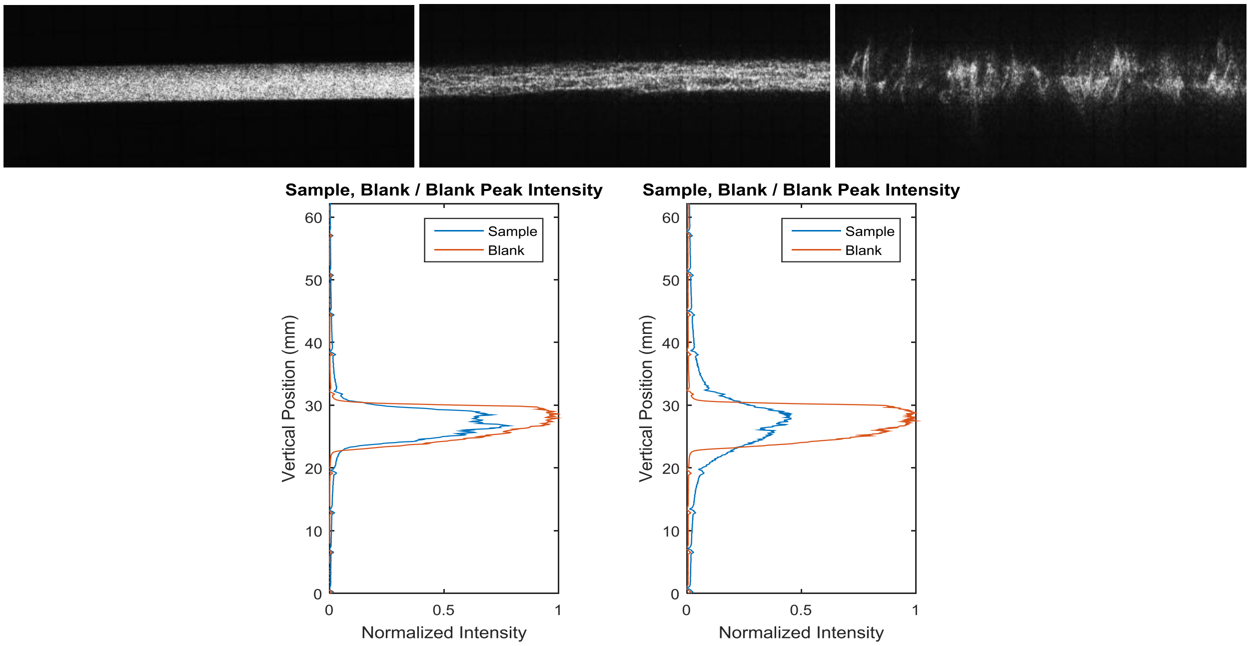

Figure A2: Unperturbed laser sheet projection (top left), sample projection with better refractive index matching (top middle), sample projection with worse refractive index matching (top right) after the addition of 0.04 mL of water. Intensity profile of better refractive index match compared with the unperturbed laser sheet, labeled as "Blank" (bottom left). Intensity profile of worse refractive index match compared with unperturbed laser sheet, labeled as "Blank" (bottom right). RIM samples were comprised of 3 mm Pyrex beads and different concentrations of DMSO and water.

As seen in Figure A3, where the respective refractive indices of Pyrex beads and glycerin were changed by changing the overall sample temperature. It is apparent that near 26 degrees C, the refractive indices of the RIM pair attain close agreement. The different scattering behavior on either side of the optimal refractive index match is due to whether the fluid has a higher refractive index than the media (above approximately 26 degrees C), or the media has a higher refractive index than the fluid (below approximately 26 degrees C).

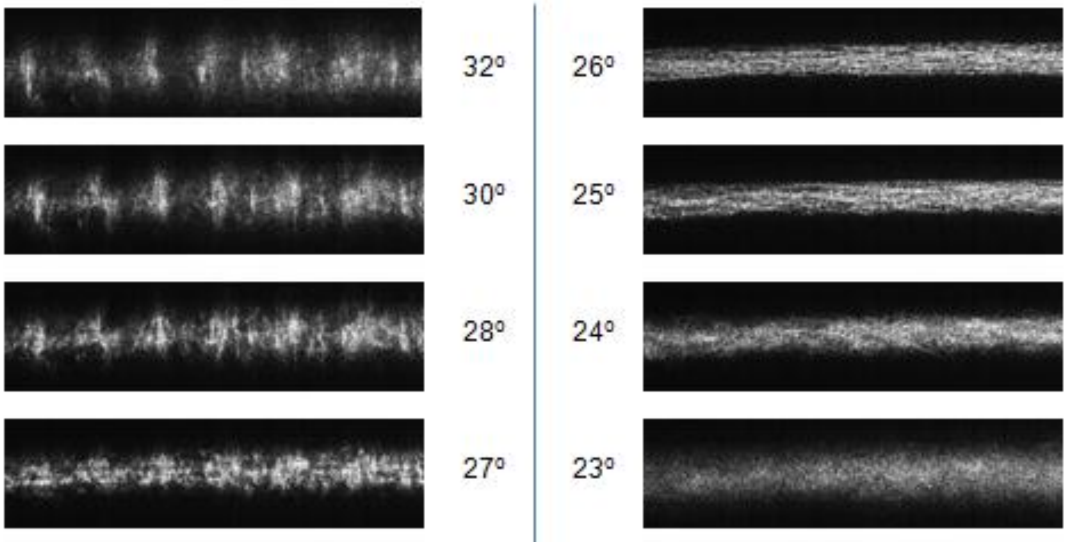

Figure A3: RIM test bench projections for temperature tuning of glycerin. Note that the least light scattering occurs at approximately 26°C.

Bead Loading Procedure

For One-Dimensional Plug Flow:

The first row of beads acts as a foundation for all subsequently added beads. Start by orienting the apparatus such that the floor is facing down, with the long apparatus floor dimension parallel to datum. The short dimension of the apparatus floor should be oriented at approximately 5 degrees from datum. The first row of beads is then added, completely filling the available length of that corner of the apparatus. The next row of beads is added, offset from the first row by one half of one bead diameter. In order to attain the correct alignment and fill all of the available space, the apparatus should be gently shaken side to side, while preserving the apparatus orientation to datum. Only add approximately ten beads at a time, then shake into place. Subsequent rows of beads should be added in the same fashion until the floor of the apparatus is completely filled with beads in the correct orientation. Visual inspection is necessary to confirm that every bead in the layer has the correct HCP orientation. Visual inspection is aided by looking at the layer from multiple angles and with unidirectional illumination from an acute angle. Depending on the apparatus geometry, there could be extra space above the top row, too narrow to fit another row of beads. This problem can be alleviated by the addition of a pliable wall on one side of the apparatus, or by designing the apparatus with a larger floor which will act to distribute the extra space through a larger number of beads.

Subsequent layers are added in similar fashion to the first layer. HCP packing must be confirmed for each completed layer before adding more beads. As more layers are added, the requirement of orienting the floor of the apparatus can somewhat be relaxed. It can be useful to gently shake the apparatus at different orientations to datum. However, great care must be taken not to hold the apparatus at extreme angles or shake to hard, as this may upset the packing of preceding layers. During the packing process, beads with irregular shape, dimension, or optical clarity must be removed, as well as any contaminants (note that these irregularities are rare for Pyrex beads). Forceps can be used to extract unwanted beads, or insert beads into random voids. Upon completion of the final layer, the apparatus lid can be affixed. In order to fill unwanted void space between the top bead layer and the lid, a pliable membrane can be applied to the lid.

For EIE:

Due to the large size of the EIE apparatus, loading the 1 mm bead sub-layer required the design and construction of specialized equipment. The bead loading rig was designed to place the 1 mm bead sub-layer and first layer of 3 mm beads into the EIE apparatus in one step, similar to the bead loading guide described in section 3.3.4. The rig consists of a completely flat platform, with a planar tolerance of 0.2mm. Beads aligned in the HCP pattern will reside on this platform prior to loading into the EIE apparatus. The platform dimensions match those of the EIE apparatus floor, to a tolerance of 0.5 mm. The tight tolerances of the platform are necessary in order to keep the 1 mm beads from changing position during operation. Five holes were drilled through the platform to match the orientation and size of the EIE wells. The platform is mounted to four rods, which are then mounted to a rigid foundation. The platform sits inside of a sliding guide, with walls that extend 3 mm above the top face of the platform when in its extended position. The guide freely slides up and down on the platform mounting rods. Alignment rods are affixed to the platform, matching the orientation and diameter of the EIE wells. The alignment rods slide through the platform when the guide is in the extended position. The platform, alignment rods, and guide walls work together to match the geometry of the EIE apparatus floor.

As shown in figure A4, the platform was temporarily held in its extended position as one layer of 3 mm beads were loaded in an HCP configuration. Next, the entire bead loading rig was held at an angle of approximately 20 degrees, at which point 1 mm beads were evenly sprinkled onto the 3 mm bead layer. 1 mm beads underwent further distribution by being gently blown into place. Care was taken to ensure that each interstitial void created by the

3mm beads contained one 1 mm bead. The EIE cell was then lowered into place, upside down, onto the top of the bead loading rig. The alignment rods of the rig guide slide into the EIE wells and the inside surface of the rig's guide walls are flush with the inside walls of the EIE apparatus. The rig platform was then slid up into the EIE cell, maintaining HCP bead alignment as it moved, until the beads came in contact with the EIE apparatus floor. The EIE apparatus and bead loading rig were then inverted, such that the 1mm beads were underneath the 3mm layer. The rig platform was then carefully extracted from the EIE cell, leaving the 1 mm and 3 mm layers in HCP configuration.

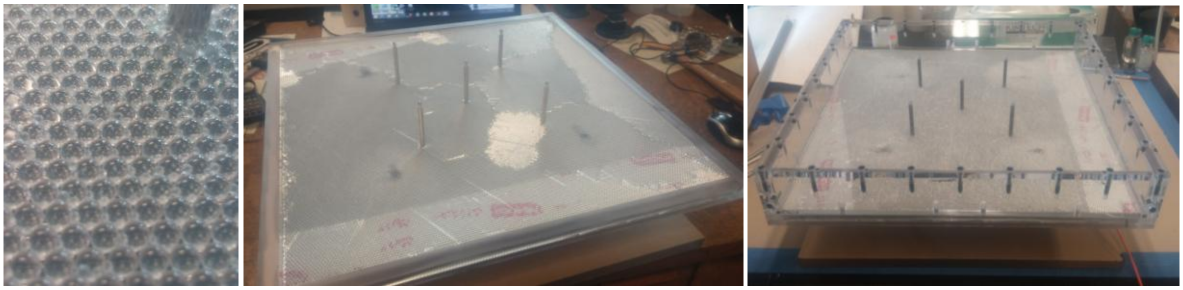

Figure A4: 3mm beads in HCP configuration topped with 1mm beads (left), bead loading rig in extended position and packed with beads (middle), EIE cell aligned with bead loading rig prior to bead placement within the EIE apparatus (right).

With the placement of the first layer of 3 mm beads complete, the subsequent layers of HCP beads could be packed by a similar method to that described in section 3.3.3. However, the loaded weight of the EIE apparatus prior to glycerin saturation was approximately 60 pounds. Due to the weight and size, it would be extremely difficult to shake beads into place without the aid of additional equipment. As seen in figure A5, the EIE cell was suspended by nylon mesh straps from scaffolding. The suspension setup permitted physical manipulation of the EIE cell, allowing beads to be gently shaken into an HCP configuration at user defined angles. A camera was mounted above the EIE cell during media packing. As every layer of porous media was completed, an image was taken of that layer's geometric configuration. The images could be used later to gain information about heterogeneity of the porous media field.

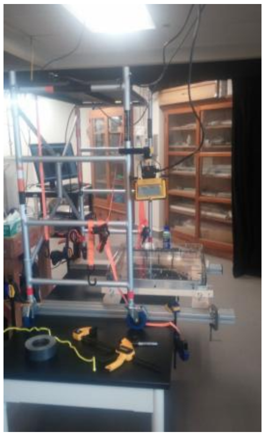

Figure A5: EIE suspension equipment for HCP bead loading.

8.4 Additional One-Dimensional Plug Flow Data

1-D flow with line of dye, various times:

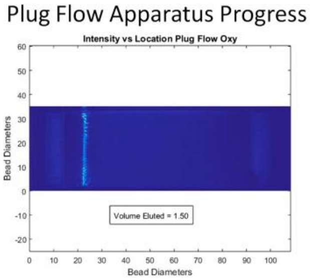
Plug Flow Apparatus Progress

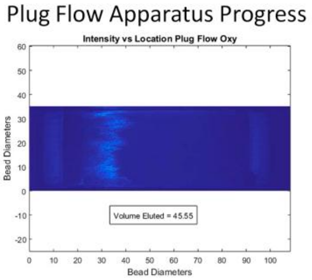
Plug Flow Apparatus Progress

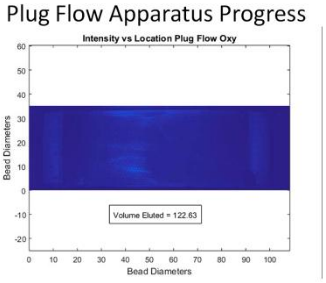
Plug Flow Apparatus Progress

Wall Effect Mitigation

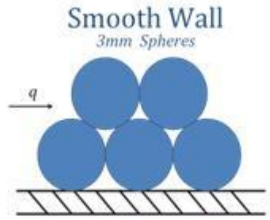

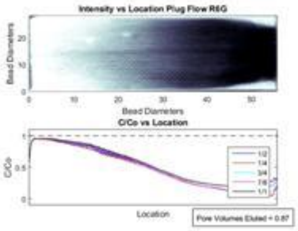

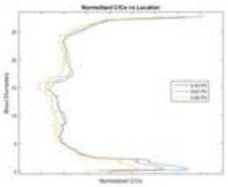

Smooth Wall, Field D=0.0023 cm²/s

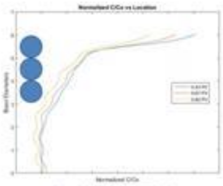

Smooth Far Wall, D=0.0023 cm/s

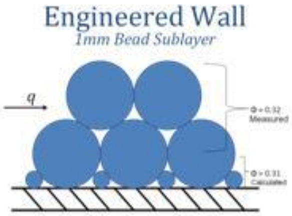

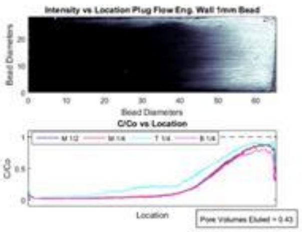

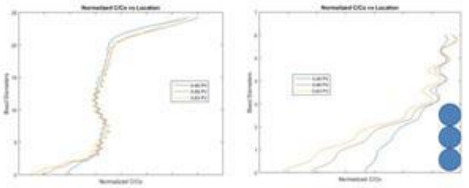

Dry Si Far Wall, 1mm Bead Near Wall, D=0.0023 cm/s

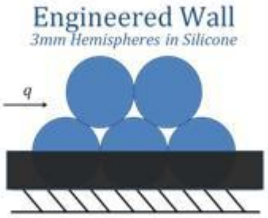

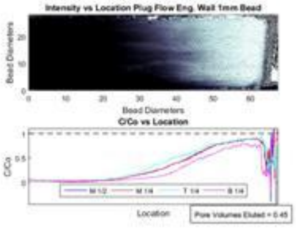

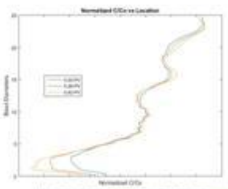

Wet Si Far Wall, 1mm Bead Near Wall, D=0.0016 cm/s

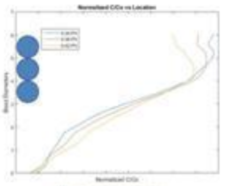

Wet Si Far Wall, D=0.0038 cm/s

8.5 Miscilaneous Data

Probe length determination

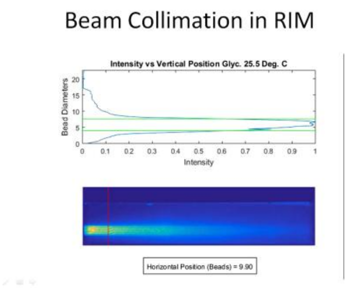
Beam Collimation in RIM

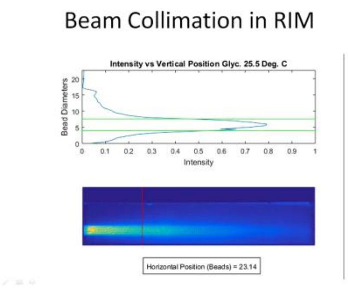
Beam Collimation in RIM

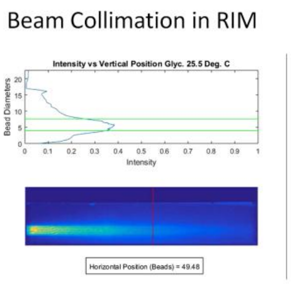
Beam Collimation in RIM

Temperature tuning, Pyrex and glycerin

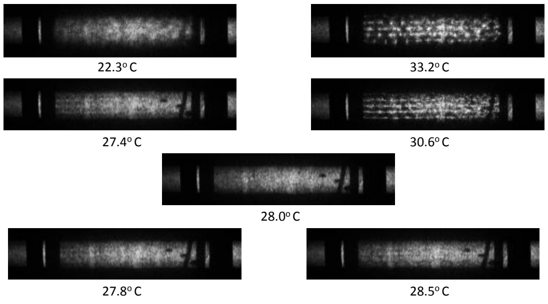
Temperature Tuning Glycerin

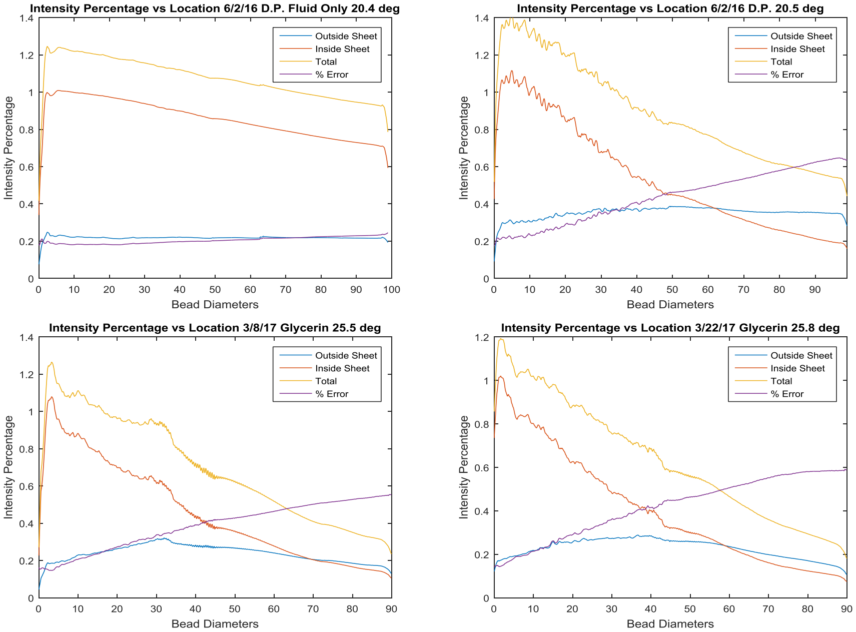

Normalized by average of intensities within beam region of highest intensity

Setup for temperature control

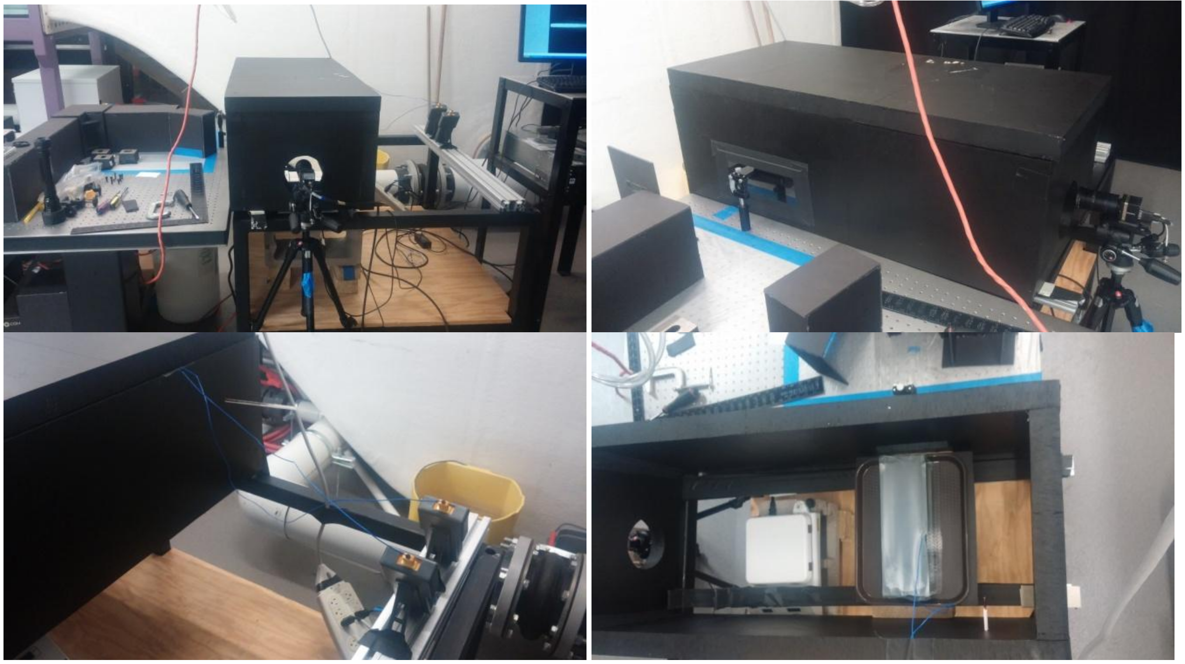

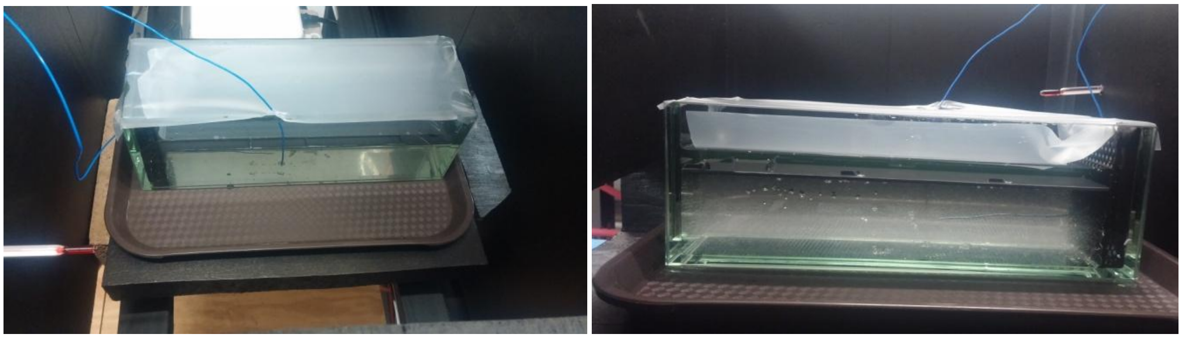

Initial dye distribution within EIE cell due to dye injection from one side